A Recycled Laser Interferometer for Gravitational Wave Detection

Shuichi Sato

DOCTOR OF SCIENCE

Department of Astronomical Science
School of Mathematical and Physical Science
The Graduate University for Advanced Studies

1998

Abstract

Several ground-based large-scale and medium-scale laser interferometers (LIGO, VIRGO, GEO600 and TAMA300) are now under construction for gravitational wave detection. A power-recycling technique is planned as a standard optical configuration to improve the shot-noise limited sensitivity. However, there was no demonstration of recycling on Fabry-Perot prototype interferometer with suspended masses and it was not clear that the recycling is really applicable to full scale detector.

Main purpose of this work is to apply the recycling technique to 20m interferometer which can simulate full scale antenna in its quality and to demonstrate the high power recycling gain of the order of 10, which is required for TAMA300 and also for other projects. In order to realize a high recycling gain, loss control of optics and interferometer is pretty important because the recycling gain is roughly proportional to the inverse of the total loss of the Fabry-Perot Michelson interferometer. Among several possible candidates of serious interferometer loss, poor reflectivity of arm cavities due to mirror loss and contrast defects of the Michelson interferometer caused by misalignment of mirrors were predominant in the case of 20m interferometer.

For the loss of optics, the quality of mirror coatings were extremely improved to have total loss of below 30ppm/optics. This was the first measurement of total loss for 10mm-size beam and best value for mirrors which are used in prototype interferometers. Further more, wave-front sensing technique was introduced as an alignment control system of the mirrors to stabilize the optical fluctuations of the interferometer. It was first demonstration of WFS on the suspended mirror interferometer.

As a result, 20m prototype interferometer locked with sufficiently high power recycling gain of over 12. This is highest gain ever reported in the world as a suspended mirror Fabry-Perot Michelson interferometer. Furthermore the remaining gain fluctuation due to mirror misalignment was sufficiently suppressed by engagement of wave-front sensing technique and stable operation was realized .

Acknowledgement

I would like to thank my two advisors: Professor Masa-Katsu Fujimoto for giving me a chance to work here, National Astronomical Observatory. Dr. Masatake Ohashi for entire support of the experiment on prototype described herein with tremendous patience and paramount inspirations. I am also grateful to the entire gravitational wave detection group for supporting this work.

Finally, I would like give my greatest thanks to Atsuko who makes everything possible.

Contents

1 Introduction 1

1.1 Gravitational Wave . . . 1

1.2 Laser Interferometric Gravitational Wave Detector . . . 2

1.3 Noise Behavior of Interferometer . . . 6

1.4 Purpose and Result of This Work . . . 8

2 Power Recycling Theories 11

2.1 Simple Theory of Power Recycling . . . 11

2.1.1 Basic Idea . . . 11

2.1.2 Recycling Gain . . . 14

2.2 Loss of Optics . . . 15

2.2.1 Mirror Loss . . . 16

2.2.2 Cavity Performance . . . 16

2.3 Loss of Interferometer . . . 18

2.3.1 Wave-Front Distortions . . . 18

2.3.2 Misalignment of Optics . . . 18

2.4 Control of The Interferometer . . . 19

2.4.1 Optical Heterodyne Technique . . . 19

2.4.2 Length Control . . . 20

2.4.3 Alignment Control . . . 23

2.5 Signal Extraction for Length Control . . . 27

2.5.1 Detection of Field . . . 27

2.5.2 Signal Extraction . . . 29

2.6 Signal Extraction for Alignment Control . . . 46

2.6.1 Detection of Field . . . 46

2.6.2 Signal Extraction 47

3 Power Recycling Experiments **57**

3.1 20m Prototype Interferometer 57

3.1.1 Optical Layout 57

3.1.2 Core1: Optics 61

3.1.3 Core2: Light Source 64

3.1.4 Core3: Suspension System 69

3.1.5 Detection System 74

3.1.6 Vacuum System 75

3.2 Loss Measurement of Optics 77

3.2.1 Theory of Loss Measurement 77

3.2.2 Experimental Setup 79

3.2.3 Experimental Results 87

3.3 Power Recycling 88

3.3.1 Optical Design 88

3.3.2 Control Design 91

3.3.3 Lock Acquisition 93

3.3.4 Recycling Gain 95

3.4 Wave Front Sensing 98

3.4.1 FP cavity Control 98

3.4.2 Interferometer Control 102

4 Conclusion **107**

List of Figures

1.1 Frequency response function of SMI. 3
1.2 Multi bounce system. 4
1.3 Response functions for Delay-Line and Fabry-Perot systems. 5
1.4 Designed noise budget for TAMA300. 7

2.1 Optical configuration of the FPMI. 12
2.2 Optical configuration of the Power Recycled FPMI. 13
2.3 Fabry-Perot cavity performance with optical losses. 17
2.4 Optical parameters of Fabry-Perot cavity. 20
2.5 Squared response function and its phase with round trip phase. 21
2.6 Independent Control (Phase-I) and Common-Differential Control (Phase-II). 22
2.7 Mode decomposition of the light from misaligned cavity. 25
2.8 TEM_{00} and TEM_{10} modes of carrier and side bands. 26
2.9 Fabry-Perot optical cavity and definition of its optical parameters. 29
2.10 Free Spectral Range and RF side band frequency for FP cavity. 30
2.11 Optical configurations of Coupled Cavity and definition of its optical parameters. 32
2.12 Magnitude of two signals for Φ and ϕ from reflected light of coupled cavity. 36
2.13 Magnitude of two signals for Φ and ϕ from picked off light of coupling cavity. 36
2.14 Schematic diagram of configuration and definition of circulating fields inside interferometer. 38
2.15 Alignment signals for IM and BM with Guoy phase evolution. 49
2.16 Alignment signals for coupled cavity with Guoy phase evolution. 51
2.17 Alignment signals for coupled cavity with Guoy phase evolution. 52
2.18 Displacement of the FP cavity due to the asymmetry of the interferometer. 53

3.1 20m prototype at Mitaka campus of NAOJ 58
3.2 Schematic over view of optical layout of 20m prototype. 59
3.3 Configuration of optics inside the center chamber. 60
3.4 Design of monolithic mirror substrates. 61
3.5 Number of layers and its designed reflectivity. 63
3.6 Design of Beam Splitter. 64
3.7 Design of mirrors. 65
3.8 The relation of FSR and side band frequency for side ban transmission. . . 67
3.9 Stabilized frequency noise of transmitted light of Mode Cleaner. 68
3.10 Stack systems for 20m prototype and for TAMA300. 70
3.11 Seismic noise spectrum on the ground and that on the bread board. 71
3.12 Transfer function of stack system of center chamber. 72
3.13 Design of double pendulum for 20m prototype. 73
3.14 Whole vacuum systems of 20m prototype. 76
3.15 Optical configuration of the tabletop experiment. 79
3.16 Optical configuration of the 20m base-line laser interferometer. 80
3.17 Amplitude gain and phase of the frequency-response function obtained by the tabletop experiment. 83
3.18 Amplitude gain and phase of the frequency-response function obtained by a loss measurement at the 20m interferometer. 84
3.19 Loss distribution within a coating surface. The several high peaks are due to point-like defects. 86
3.20 20m. 89
3.21 Degradation of cavity performance due to optical losses. 90
3.22 Control design for length sensing (Phase-I). 91
3.23 Control design for length sensing (Phase-II). 92
3.24 Schematic diagram of feed back system. 93
3.25 Open loop transfer function for arm cavity control loops. 94
3.26 Attained recycling gain with $R = 0.70$ mirror. 96
3.27 Attained recycling gain with $R = 0.91$ mirror. 97
3.28 Optical configuration for alignment control of FP cavity. 99
3.29 Beam propagation from the waist of the cavity mode to WFSs through GPT. 100
3.30 Alignment signals for IM and BM with Guoy phase evolution. 100

3.31 Open loop transfer function of alignment control loop. 101
3.32 Stabilization of FP cavity by alignment control. 102
3.33 Optical configuration of PRFPMI with WFSs. 103
3.34 Stabilized recycling gain by engagement of alignment control. 104

Chapter 1

Introduction

1.1 Gravitational Wave

Nature of the gravity is interpreted as a nature of spacetime itself according to general relativity. The physics of spacetime can be described by Einstein's equation, which is a relation between mass-energy density and spacetime curvature. This theory can explain the gravitation by attributing spacetime with tensor field, metric $g_{\mu\nu}$. In weak gravitational field limit, for example here on the earth, the metric can be approximated by using small perturbation $h_{\mu\nu}$ from Minkowski (flat) metric $\eta_{\mu\nu}$ as

$$g_{\mu\nu} \simeq \eta_{\mu\nu} + h_{\mu\nu}, \tag{1.1}$$

here $|h_{\mu\nu}| \ll 1$. Then the weak field Einstein equation in vacuum take the form with suitable choice of gauge,

$$\left(-\frac{1}{c}\frac{\partial^2}{\partial t^2} + \Delta^2\right) h_{\mu\nu} = 0. \tag{1.2}$$

This equation leads a wave form solution, which have a form of

$$h_{\mu\nu} = A_{\mu\nu} e^{ik_\mu x^\mu}, \tag{1.3}$$

were k_μ satisfies $k_\mu k^\mu = 0$. With further choice of gauge known as transverse traceless gauge, $A_{\mu\nu}$ can be simplified for a frame in which the wave is traveling in the z-direction

as

$$A_{\mu\nu} = \begin{pmatrix} 0 & 0 & 0 & 0 \\ 0 & h_+ & h_\times & 0 \\ 0 & h_\times & -h_+ & 0 \\ 0 & 0 & 0 & 0 \end{pmatrix} \tag{1.4}$$

Suppose that Michelson interferometer is placed in x-y plain with its arms along with x and y axis respectively. Using TT gauge, the geodesic equation means that the coordinate position of free masses does not change in the presence of a gravitational wave, but proper distance along the x-axis $ds^2 = g_{\mu\nu}dx^\mu dx^\nu$ is affected,

$$\Delta s = \int |g_{xx}|^{1/2} dx \simeq \left[1 + \frac{1}{2}h_0\right] x_0 \tag{1.5}$$

for plus polarized wave. The gravitational wave produces a strain of space, in the sense of change in the proper distance between two test particles. On the other hand, for the y direction of arm the opposite change is given in the travel time, so difference between two arm length as measured by the light is

$$\Delta L = hL \tag{1.6}$$

Thus the fringe of the Michelson interferometer is affected by this change due to gravitational wave, and this make it possible to measure gravitational waves directly.

Current interferometer design is expanded to multi bounce system, Fabry-Perot Michelson or Delay line, in order to optimize the arm length in a limited space.

1.2 Laser Interferometric Gravitational Wave Detector

The principle of interferometric detection of gravitational wave is measuring optical phase shift of the laser light caused by gravitational wave passing on the interferometer . So, the optical layout which can convert the strain of gravitational wave into optical phase change as effective as possible should be adopted as a design of interferometer. Before discussing full configured interferometer, it is worth while to consider the simple Michelson interferometer (SMI). The phase sensitivity in each arm is given by $d\phi/d\ell = 4\pi/\lambda$, so phase shift can be

approximated as

$$\Delta\phi_{GR} \simeq \frac{4\pi}{\lambda} h(t)\ell, \tag{1.7}$$

only for slowly varying $h(t)$, here λ is the wave length of laser light, $h(t)$ is time dependent strain and ℓ is the arm length of the interferometer. Using Fourier transformed $h(t)$,

$$h(t) = \int h(\omega) \mathrm{e}^{i\omega t} d\omega, \tag{1.8}$$

the frequency dependent phase shift will take the form of

$$\Delta\phi_{GR} = \int h(\omega) \mathrm{e}^{i\omega t} H_{SMI}(\omega) d\omega \tag{1.9}$$

$$H_{SMI}(\omega) = \frac{2\Omega}{\omega} \sin\left(\frac{\ell\omega}{c}\right) \mathrm{e}^{-i\omega\ell/c}, \tag{1.10}$$

where, $H_{SMI}(\omega)$ is a frequency response function of SMI to gravitational wave which is shown in Fig.1.1. From this expression, DC-gain of transfer function is maximized by

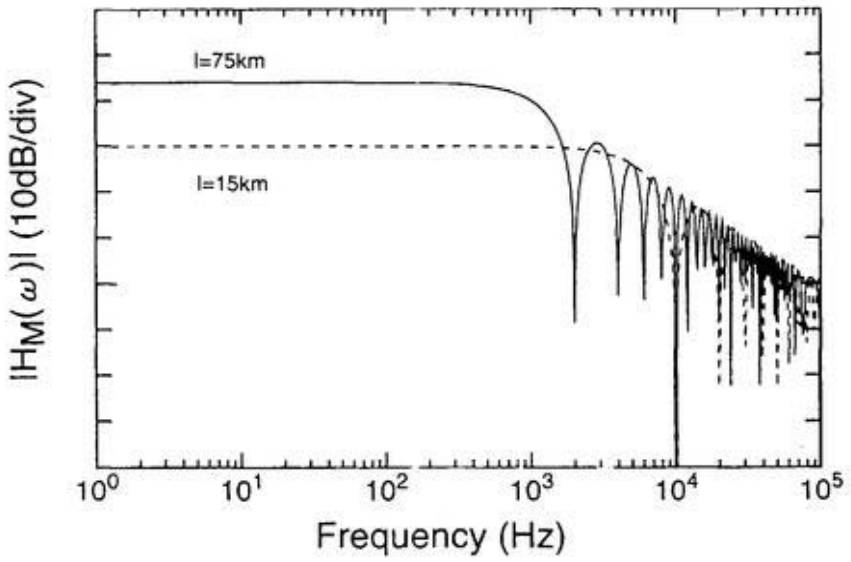

Figure 1.1: Frequency response function of SMI.

the condition of $\ell\omega_0 = \pi/2$ for specific frequency of gravitational wave ω_0. For example, optimum ℓ is 75km for 1kHz wave and this is not realistic for ground based interferometer with respect to build such huge facilities. In order to settle this difficulties, multi bounce

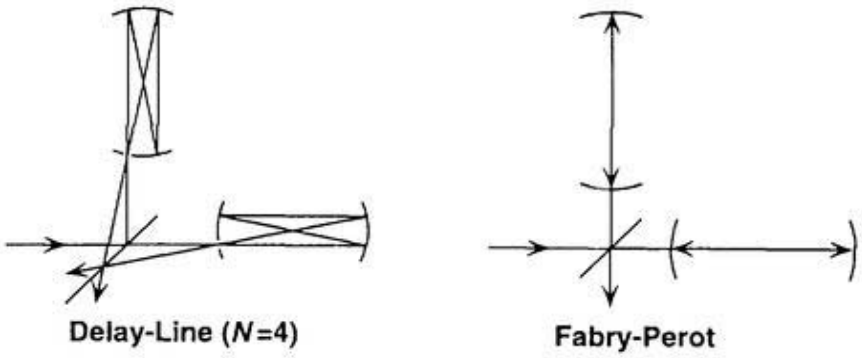

Figure 1.2: Multi bounce system. Delay-Line system holds beam line inside two arm mirrors by N-times. The beam will multiple interfere in cavities for Fabry-Perot cavity system.

methods have been suggested; Delay-Line and Fabry-Perot cavity systems inFig.1.2. The frequency response functions for both systems are given as

$$H_{DL}(\omega) = \frac{2\Omega}{\omega} \sin\left(\frac{N\ell\omega}{2c}\right) e^{-iN\ell\omega/2c}, \tag{1.11}$$

where, N is bounce number and

$$H_{FP}(\omega) = \frac{2\Omega}{\omega} \frac{t_{IM}^2 r_{BM}}{1 - r_{IM} r_{BM}} \sin\left(\frac{\ell\omega}{c}\right) e^{-i\ell\omega/c} \frac{1}{1 - r_{IM} r_{BM} e^{-2i\ell\omega/c}}, \tag{1.12}$$

where r, t are amplitude reflectivity and transmission of mirrors. Subscriptions IM,BM denote Input Mirror and Back Mirror of the optical cavity respectively.[1] Amplitude gain for both functions are compared in Fig.1.3, using typical parameters for full scale detectors. In past decade, both configurations were tested by using prototype interferometers over the world and current projects are employing FP system or SMI as a optical design.

Several ground-based large-scale,medium-scale laser interferometers (LIGO, VIRGO, GEO600 and TAMA300) are now under construction for gravitational wave detection, as summarized in table 1.1. A Michelson-type interferometer using Fabry-Perot cavities in its arms is employed for TAMA300 and the optical parameters of the input and end mirrors for each arm cavities were designed to be R=0.9880 and 0.9999 in power reflectance, respectively. The expected qualities of the cavity are a finesse of 516 and a cavity reflectance of 0.96, assuming loss-free mirrors.

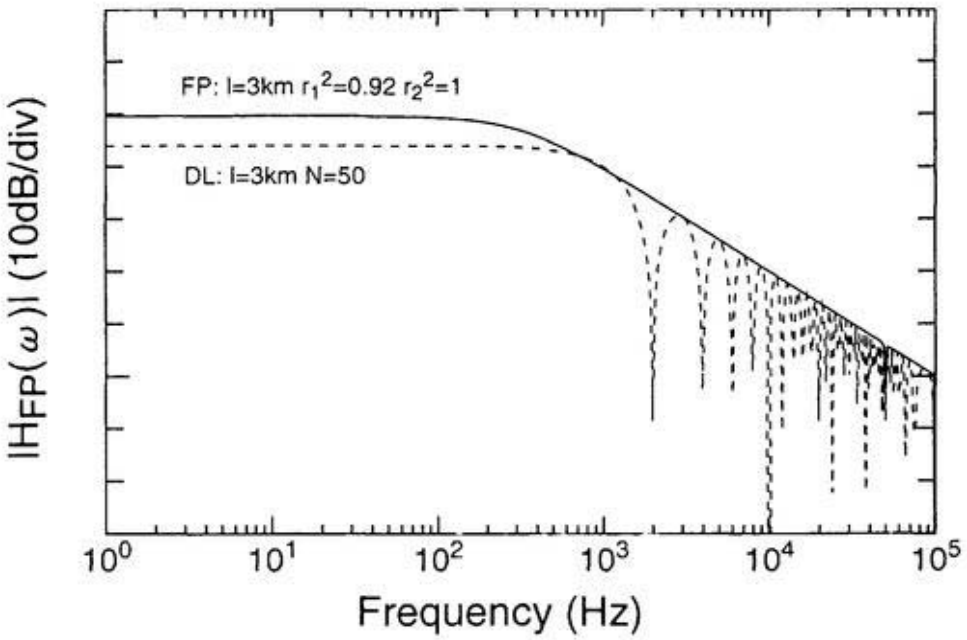

Figure 1.3: Response functions for Delay-Line and Fabry-Perot systems.

Project	Host	Institutions	Arm Length	Storage Time τ_s
LIGO[2]	U.S.	Caltech, MIT	FP 4 [km]×2	0.88 [msec]
VIRGO[3]	FRA, ITA	IFNF, PisaUniv., CNRS	FP 3 [km]	0.31 [msec]
GEO600[4]	GER, GB	MPQ, GlasgowUniv.	DR 600 [m]	
TAMA300[5]	JPN	NAOJ, UT, UEC, KEK, ...	FP 300 [m]	0.33 [msec]

Table 1.1: Projects for interferometric gravitational wave detection.

A power-recycling techniqueis also planed as a standard optical configuration for all projects employing the optically recombined interferometer design; also, its recycling gain (power-enhancement factor of the light inside the interferometer by the recycling technique) is roughly proportional to the inverse of the total loss of the Fabry-Perot Michelson interferometer (at a beam splitter) as an one complex mirror for the recycling cavity.

1.3 Noise Behavior of Interferometer

As is described in previous section, the signal of gravitational wave are detected as a output signal of Michelson interferometer in principle. Though the expected signals from astrophysical sources are extremely small, there will be no difficulties to detect them without any other noise. However, there are a lot of possible hosts of noise that can appear at the output not only to disgrace but overwhelm gravitational wave signals.

Typical noise sources, which are thought to be serious limiting source for detector sensitivity for TAMA300, are summarized in Fig.1.4. [6]

The shot noise, the statistical error in the photon counting process is intrinsic noise for detectors which use light as a measurement prove. This is expected to be limiting factor in most interesting frequency range and above this frequency if other artificial noises are negligible small. Corresponding expression in detail for shot noise limited sensitivity will be introduced in later section. In principle, it will decrease in proportion with the inverse of square root of input light power incident to the interferometer. In other words, if the sensitivity of the interferometer is shot noise limited, the only way to improve the limitation is increasing the input power inside the interferometer.

The second one is seismic noise. For ground based interferometers, it is impossible to prevent the effect of seismic motion of the ground completely. The typical ground motion is reported to have the spectrum of [7]

$$x_{seis} \simeq 10^{-7} \left(\frac{1\mathrm{Hz}}{f} \right)^2 [\mathrm{m}/\sqrt{\mathrm{Hz}}]. \tag{1.13}$$

In order to isolate this ground motion sufficiently at observation band, many kind of low-pass filters have been developed, for example, pendulum, stack mechanical filters and active dumpers.

The third ones are thermal noises. The test mass itself is still vibrating due to its thermal energy without external excitations. According to principle of equipartition, a

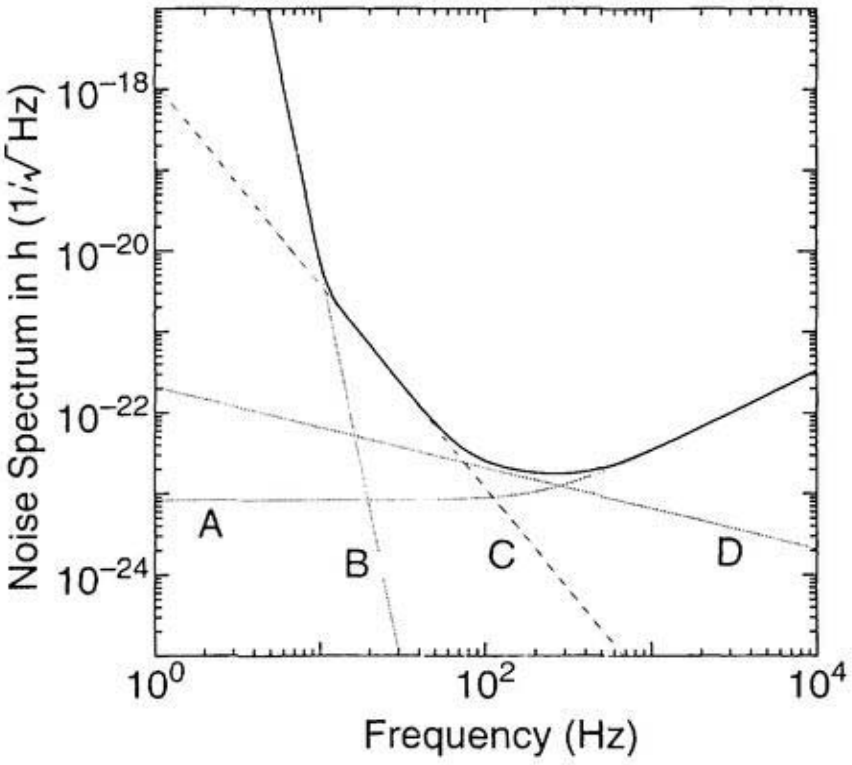

Figure 1.4: Designed noise budget for TAMA300. A: Shot noise. B: Seismic noise. C:Thermal noise of pendulum. D: Thermal noise of mirror internal modes.

kinetic energy of $\frac{1}{2}k_BT$ are divided to each vibration modes. These energies will diffuse to frequency ranges around resonance due to fluctuation- dissipation theorem. The modes relevant to test masses are the internal modes of them, pendulum modes and violin modes of suspending wire. These can be reduced by making the quality factor (Q-value) high and/or cooling down the temperature.

1.4 Purpose and Result of This Work

There are a lot of optical and electronical techniques planned to be applied to full scale detector, including advanced configurations of interferometer. A number of table top experiments with small scale and with rigidly supported mirrors were already performed to demonstrate these techniques. The next step is to demonstrate them on a prototype class interferometer with free masses and to scale up these techniques to long base line interferometers. Usually, in order to simulate the full scale detector, these "prototypes" have many equipment of the same quality as a full scale detector; for example, Nd:YAG laser, mode cleaner, vacuum system, suspended free masses and high quality optics. In contrast with table top or small size interferometers, long base line interferometers are hard to operate and to maintain the performance in general. These difficulties mainly come from large size of laser beam and length of arms. For example, imperfections of optics with a scale of millimeter can cause a serious defect to the larger aperture beams but do not to the smaller beams, larger interferometer are more sensitive to misalignment of optics than shorter ones. In this regards, it is important to demonstrate that the recycling technique is applicable to these prototypes.

This work focused on the most exciting issue of power recycling, recycling gain. The recycling gain is defined as a power enhancement factor of light incident on the interferometer. Main purpose of this work is to apply the recycling technique to 20m interferometer which simulates a full scale antenna in its quality and to demonstrate the high power recycling gain of the order of 10, which is required for TAMA300 and also for other projects. In addition to high recycling gain, study of lock acquisition sequence of high recycling gain interferometer was also an important subject of this thesis.

In order to realize a high recycling gain, loss control of optics and interferometer is pretty important since a recycling gain is roughly proportional to the inverse of the total loss of the interferometer. Resulting recycling gain of 450 was reported for simple Michelson inter-

Nickname	Institution	Arm Length	Start	First Lock	Designed Gain
Mark II	Caltech (U.S.)	40m	1996	Dec 1997	8
Tamago	NAOJ (JPN)	20m	1997	Jun 1998	-
-	UT (JPN)	3m	1996	Nov 1997	-
-	Garching (GER)	30m	-	-	-

Table 1.2: Projects for interferometric gravitational wave detection.

ferometer with suspended mirrors .[8] On the other hand, FP Michelson interferometer with fixed mirror table top experiments demonstrated the recycling gain of 18 at the time when this experiment started.[10] The discrepancy between two cases is mainly comes from the difference in reflectivity between simple mirrors and combined FP cavities. Further more, in case of FPMI with suspended mirrors, misalignments of mirrors degrade the contrast of Michelson interferometer as well as reflectivity of FP cavity. Therefore, it is not obvious to attain the high recycling gain with FPMI prototypes. On going recycling experiments for FPMI with suspended mirrors are shown in table 1.2 Among several possible candidates of serious interferometer loss, poor reflectivity of arm cavities due to mirror loss and contrast defects of the Michelson interferometer caused by misalignment of mirrors were predominant in the case of 20m interferometer.

For the loss of optics, the quality of mirror coatings were extremely improved to have total loss of below 30ppm/optics. This was the first measurement of total loss for 10mm-size beam and best value for mirrors which are used in prototype interferometers. Further more, wave-front sensing technique was introduced as an alignment control system of the mirrors to stabilize the optical fluctuations of the interferometer. It was first demonstration of WFS on the suspended mirror interferometer.

As a result, 20m prototype interferometer locked with sufficiently high power recycling gain of over 12. This is highest gain ever reported in the world as a suspended mirror Fabry-Perot Michelson interferometer. The whole interferometer was acquired lock by both sequential and automatic locking method within a minute typically. Furthermore the remaining gain fluctuation due to mirror misalignment was sufficiently suppressed by engagement of wave-front sensing technique and stable operation was realized . Success of this work on high gain recycling and implementation of automatic alignment control

system using wave-front sensing on 20m interferometer marks significant progress towards achieving full-configured interferometer.

Chapter 2

Power Recycling Theories

2.1 Simple Theory of Power Recycling

In this section, the original idea of power recycling technique is described. The signal extraction and other control issues will be described in later section.

2.1.1 Basic Idea

The original idea of power recycling was suggested by Drever and Schilling[12] in order to improve the shot noise limited sensitivity of the laser interferometer for a gravitational wave antenna. The shot noise limited sensitivity of Fabry-Perot Michelson interferometer is approximately given by

$$h_{min} \simeq \sqrt{\frac{\hbar\lambda[1+(\tau_S\omega)^2]}{4\pi c\eta_{PD}P_0\tau_S^2}\Delta f} \tag{2.1}$$

$$\tau_S = \frac{\ell\sqrt{F}}{c} = \frac{2\ell}{c}\frac{\sqrt{r_{IM}r_{BM}}}{1-r_{IM}r_{BM}} \tag{2.2}$$

where, τ_S is the storage time of the photon inside the arm Fabry Perot cavities, ℓ is arm length, r_i are amplitude reflectivities with i denoting specific mirrors, η_{PD} is efficiency of photo diode including quantum efficiency, Δf is observation band width and P_0 is the light power incident to the interferometer.[1] From this expression, the only parameter which can improve the limit is incident power to the interferometer P_0, once optical configuration is determined. For example, the required light power in order to achieve the strain sensitivity of $h = 10^{-21}$ with Nd:YAG light (λ = 1064nm) with bandwidth of 1kHz around 1kHz

will exceed 1kW. Such ultra-high power cw laser source is not available with current laser technologies. For example, output power of the laser which is prepared for TAMA300 (developed by SONY Co;Ltd.) is 10W and that for initial LIGO (manufactured by Lightwave Electronics Co; (MOPA)) is also 10W. Then recycling technique can settle this difficulties as described below.

The optical configuration of Fabry-Perot Michelson Interferometer (FPMI) and Power Recycled Fabry-Perot Michelson Interferometer (PRFPMI) are shown in Fig.2.1,2.2. As

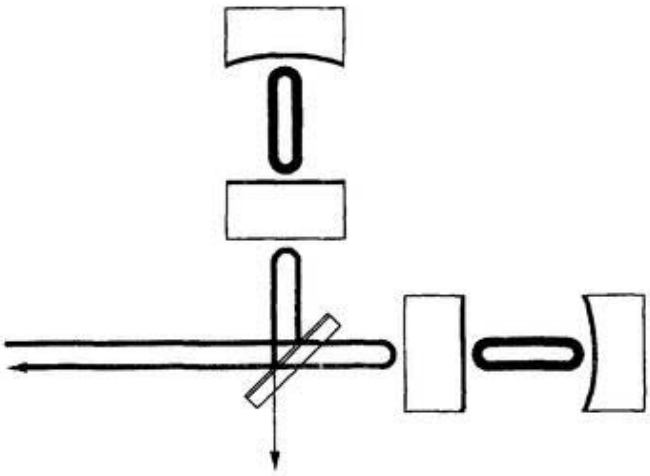

Figure 2.1: Optical configuration of the FPMI.

is same for simple Michelson interferometer, the output fringe of the antisymmetric output (read out) of the FPMI is given by

$$P_{DIFF} = \frac{1}{2} P_0 (1 - C\cos(\phi)), \tag{2.3}$$

where, ϕ is relative phase difference between two arms and C is contrast. Generally, this antisymmetric output will be kept $\phi=\pi$, i,e, the dark fringe for the carrier light at operational point. In a well-balanced interferometer, dark fringe operation at the antisymmetric output means that the symmetric output become bright and a lot of power of light comes

FPMI as a complex

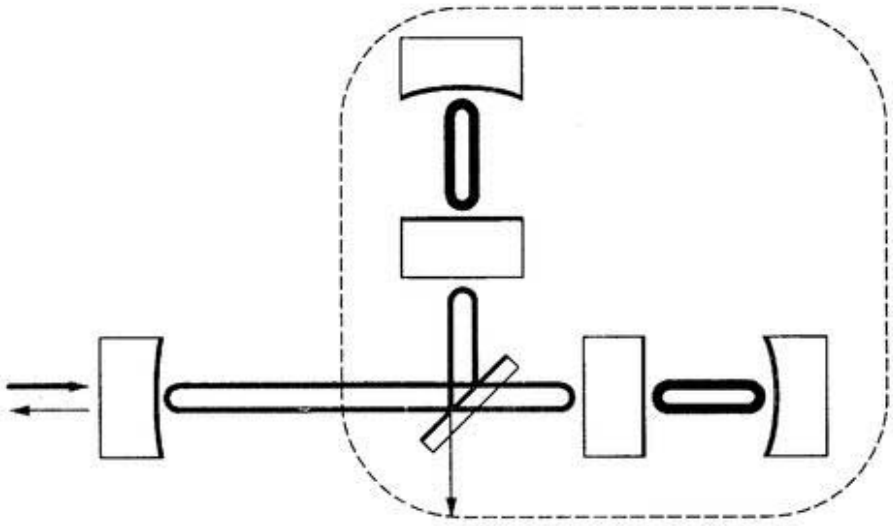

Power Recycled Fabry-Perot Michelson Interferometer

Figure 2.2: Optical configuration of the Power Recycled FPMI.

back toward the light source. With this point of view, the FPMI in operation is regarded as a kind of very complicated mirror, which can include optical loss, asymmetry of configurations, imperfections of control and so on.

It is worth while to consider the Fabry-Perot cavity before discussing recycled configuration of the interferometer. The circulating power inside the cavity can be increased by keeping the cavity on resonance by factor of

$$G_{CAV} = \frac{P_{inside}}{P_{incident}} \tag{2.4}$$

$$= \left(\frac{t_{IM}}{1 - r_{IM}r_{BM}}\right)^2. \tag{2.5}$$

Of course, the power enhancement factor completely depends on the design and quality of the mirrors which consists of the resonator, that is, r_i, t_i determine G_{CAV}. This idea is applicable to the case of FPMI, i,e, complex of cavities as a single mirror. In these expressions, the input mirror corresponds to the recycling mirror and end mirror to the FPMI compound mirror. The circulating power inside the interferometer can be increased by composing the "recycling cavity" with recycling mirror in front of the interferometer.

The power enhancement factor by using recycling is also expressed with same way as for the plain cavity,

$$G_{REC} = \left(\frac{t_{REC}}{1 - r_{REC}r_{FPMI}}\right)^2 \tag{2.6}$$

$$= \left(\frac{t_{REC}}{1 - \sqrt{1 - A_{REC} - t_{REC}^2}\sqrt{1 - A_{FPMI} - t_{FPMI}^2}}\right)^2. \tag{2.7}$$

This factor is called recycling gain G_{REC} in original meaning, but precise definition will be given in later section because $P_{incident}$ contains carrier and sidebands components due to phase modulation. The carrier and sidebands will have different power enhancement factors in general.

2.1.2 Recycling Gain

The optimized transmission of recycling mirror can be obtained by differentiating G_{REC} with respect to r_{REC}.

$$\frac{\partial}{\partial r_{REC}} G_{REC} = 0 \tag{2.8}$$

$$T_{REC} = (1 - A_{REC})(1 - R_{FPMI}(1 - A_{REC})) \tag{2.9}$$

So, the recycling gain G_{REC} can be maximized by making equal the R_{REC} to the reflectivity of the interferometer for the given R_{FPMI} if there is no loss ($A_{REC} = 0$) for optics. Thus, once the reflectivity of the FPMI is determined, the maximum of the recycling gain is limited to finite value according to the R_{FPMI}. Using this T_{REC}, maximized recycling gain G_{REC}^{max} is approximated as

$$G_{REC}^{max} = \frac{P_{inside}^{max}}{P_{incident}} \tag{2.10}$$

$$\simeq \frac{1}{A_{REC} + A_{FPMI}}. \tag{2.11}$$

From this expression, the maximized recycling gain is roughly proportional to the inverse of the total loss of the recycling cavity.[10] So, in order to realize the possibly high recycling gain the loss of the interferometer (A_{FPMI}) should be minimized.

The primary candidates which can dominate the degradation of FPMI reflectivity up to a few percent are poor quality of optics and imperfections of interferometer control. If these interferometer loss can be suppressed within, for example, one percent, the attainable recycling gain will reach to $G_{REC} = 1/0.01 = 100$, which is sufficient to full scale detector design.

2.2 Loss of Optics

Though power recycled laser interferometer has sufficiently complex configuration as is seen in Fig.2.2, its recycling cavity can be thought as a plain FP cavity with "reflectivity variable mirror" as a back mirror, once FPMI part after beam splitter is regarded as one compound mirror. In this meaning, high recycling gain is interpreted to small loss optics, recycling mirror and compound mirror as optics. Moreover, high quality compound mirror for high recycling gain means high reflection efficiency of both arm cavities and high interference efficiency at the beam splitter. Therefore, two factors are very important for building "rich" recycling cavity, as possible hosts which can be anomalous losses over one percent; to maintain the reflection efficiency of arm cavities high, which can be interpreted as to reduce the total loss of both input and back mirror, and to maintain interference efficiency high.

2.2.1 Mirror Loss

High-quality mirrors with high reflectance and super-low losses (including absorption and scattering) have many applications in optical and laser science. Recently, there has been considerable interest in ultra-low-defect (as a scattering source) multi-layer coating and ultra-smooth polishing techniques, which are indispensable for high-quality mirrors along with the advances of semiconductor industries, such as EUV lithography and with the needs of scientific research, such as gravitational wave detection.

In recent years, the losses of dielectric multi-layer coating mirrors have been greatly reduced. A high-quality cavity using ultra-low-loss mirrors has been demonstrated to have 1.5ppm losses/optics at a wavelength of 1064nm with a small beam spot size ($2w_0$=0.38mm) by a tabletop experiment.[11] This is the lowest loss factor to be measured using a small Nd:YAG beam ever known.

In particular, in the case of a laser interferometric gravitational wave detector, ultra high-quality mirrors (low scattering and absorption losses) are required to obtain a good performance of the Fabry-Perot cavity, a high recycling gain and to avoid any thermal-lensing effect. Furthermore, another important feature concerning the requirements for the mirrors is the uniformity of the mirror coatings and losses in addition to a good surface figure and small microroughness of the mirror substrate, since any inhomogeneity which can cause wave front distortions degrades the efficiency of the interference. The total loss of a rather wide area (typically several centimeters of radius for full scale interferometers) of the mirrors, including scattering from the mirror substrate, should be kept sufficiently small, because the longer the arms of the interferometer become the bigger the beam spot on the mirror surface grows.

2.2.2 Cavity Performance

Optical parameters of the resonant Fabry-Perot cavity are characterized by its optical design and imperfections of mirrors, if the control system is appropriate. Though three observable quantities, that is, reflection efficiency (η_R), transmission efficiency (η_T) and finesse ($\mathcal{F}$) can be calculated strictly using designed reflectivities of the mirrors for loss free resonator, practical performance of the cavity can be degraded with finite imperfection of the mirrors. Loss dependencies of these quantities can be investigated using following

expressions.

$$\eta_R = \left(r_{IM} - \frac{t_{IM}^2 r_{BM}}{1 - r_{IM} r_{BM}} \right)^2 \tag{2.12}$$

$$\eta_T = \left(\frac{t_{IM} t_{BM}}{1 - r_{IM} r_{BM}} \right)^2 \tag{2.13}$$

$$\mathcal{F} = \frac{\pi \sqrt{r_{IM} r_{BM}}}{1 - r_{IM} r_{BM}} \tag{2.14}$$

Total loss of the cavity is caused by many different mechanisms, absorption, scattering of mirror substrate and coating and so on. Furthermore, it is possible that these parameters have different values dependent on beam size due to imhogeniety of substrate and high-reflecting coating. So, it is difficult to determine the proportion between reflection and transmission reduction caused by increased loss. Suppose dominant loss is only scattering and this degrade only reflectance of mirrors. This loss can debase the quality of cavity as is shown in Fig. 2.3. In these calculations, designed mirror reflectivities are $r_{IM}^2 =$

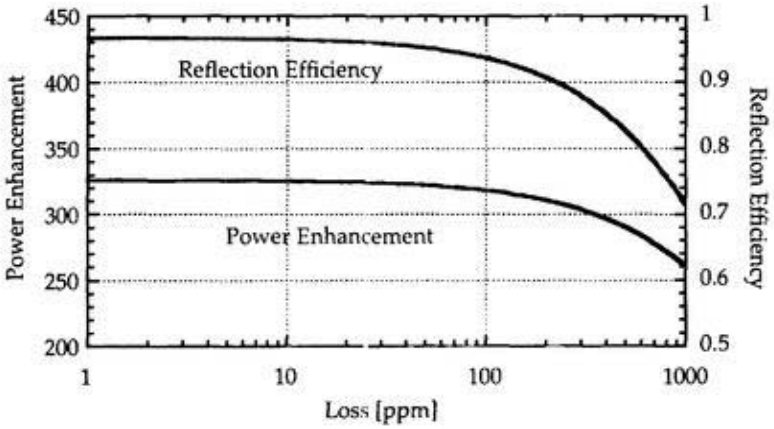

Figure 2.3: Fabry-Perot cavity performance with optical losses.

0.9880and $r_{BM}^2 = 0.9999$ which are used for 20m prototype and TAMA arm cavities. For demonstration of the high gain recycling, the reflection efficiency of the both arm cavities are key quantities from the point of view of power recycling. As is described in previous section, at least 90% of reflection efficiency of the arm cavities are needed for recycling gain of 10 without any other optical losses inside the interferometer. This means that total loss of the mirrors should be suppressed below 100ppm/optics and below 50ppm if possible.

2.3 Loss of Interferometer

Several effects can be classified to two categories as optical losses which are induced by the interferometer; power degradation of FP cavity and contrast defects at the beam splitter. Further more, both power loss can be caused by wave-front distortions due to optics, misalignment of optics and imperfect control of interferometer.

2.3.1 Wave-Front Distortions

It is common idea that imperfect reflecting surface of optics can cause wave-front distortions for mainly reflected beam. This effect completely depends on the quality of optics, especially on polishing of mirror substrates and also on the uniformity of HR coating with the scale of beam size. However, it is clear that this will take more effect for large-beam using interferometer. This issue should be treated as a surface flatness which contains so called micro roughness and figure error, in connection with its power spectrum of the surface figure with special wave length.

Precise experimental study have not been performed yet for this kind of issues, but computer-aided simulation study is now under going by using "FFT" program which was developed by LIGO group. This program can simulate the propagation of field directly in the time domain with fixed mashed optics, and this work will be able to clarify this problem quantitatively in near future.

2.3.2 Misalignment of Optics

Optical characteristics of whole interferometer can be predicted by calculating the fields using plain wave approximation with no misalignment for all optics, But some optical performance will differ with presence of finite misalignment of any optics. For example, misalignment of input and back mirrors of FP cavity can prevent proper power build-up inside the cavity and this misaligned cavity will scatter fundamental mode of the incident beam to higher order modes in part. If these misalignments exist in both arm cavities of the interferometer, reflected light from each arms contains incoherent higher order modes, basically. As a result, these higher modes does not interfere constructively at the beam splitter and can not circulate in the recycling cavity. There are two origins for these misalignments. One is initial misalignments of optics and that caused by drifts of any

suspension system of optics, which corresponds to near DC component. The other one is pith and/or yaw motion of suspended optics excited mainly by the seismic motion.

For large scale interferometers, the alignment control system of all optics is thought to be a basic item and misalignment below μrad is required.

2.4 Control of The Interferometer

If the ground is sufficiently quiet so as not to shake suspended mirrors, all optics can be left free at the appropriate positions along with optical axis, at which whole interferometer locks and resonates. But seismic motion can move each mirrors by the scale of several wave length in the case of 20m prototype. So, the cavities and the Michelson part have to be length controlled in order to maintain resonances and lock. For the FP optical cavity, Pound-Drever-Hall technique using phase modulation on incident light is adopted as a standard locking method.[12] This method is often called as "reflection locking scheme" or "optical heterodyne technique". Also for interferometer, applied PDH method with pre-modulation (Shnupp method) is employed for control of all degrees of freedom.

In addition to length degrees of freedom, that of mirror orientations are also fluctuating. These are called as angular misalignment of the mirror, which can be caused by drift or resonance motion of the suspension system. Since these misalignments of the interferometer mirrors can both decrease power build up in the cavities and degradation of contrast at beam splitter, this should be suppressed sufficiently small. For example, 10^{-7} [rad] is requirement of TAMA. As a method of alignment sensing, optical heterodyne technique is also used to extract the signals.

2.4.1 Optical Heterodyne Technique

It is worth while to mention about optical heterodyne technique briefly because this is core of signal extraction for length and alignment control. When the laser light is incident to optical cavity, its reflection and transmission efficiency change according to the cavity length ℓ. Suppose amplitude reflectance and transmittance of both mirrors are defined as Fig.2.4. Using these parameters, response function for reflected light from the cavity is expressed as a function of round trip phase $\varphi=2\omega\ell/c$ as

$$\eta_R(\varphi) = r_1 + \frac{t_1^2 r_2 e^{-i\varphi}}{1 + r_1 r_2 e^{-i\varphi}}, \tag{2.15}$$

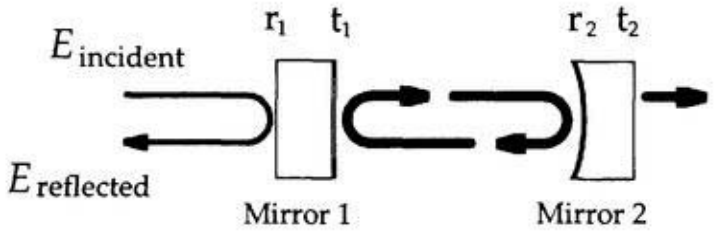

Figure 2.4: Optical parameters of Fabry-Perot cavity.

where, ω is angular frequency of light and c is speed of light. The cavity resonate when the condition $\exp(2\omega\ell/c) = -1$ is satisfied. The reflection efficiency and its phase around resonance is sown in Fig.2.5. From φ dependence on reflected light, it is clear that the amplitude shows symmetric change around resonance, while phase changes anti-symmetric. So, in order to keep cavity lock, phase change of reflected light can be used as an error signal. However, it is difficult to detect the optical phase of light directly. Then the phase modulation side bands are imposed as a phase reference. Here, length deviation from the resonance is interpreted as a phase deviation of the light and then converted to detectable amplitude change of side band frequency by using side band as a phase reference. Precise descriptions are in later section.

2.4.2 Length Control

There are four degrees of freedom to be controlled for power recycled FP Michelson interferometer; two lengths of both arm cavities and differential and common length of recycling cavity. In this thesis, L denotes arm cavity length and recycling cavity length is indicated by l. Two arm cavities are distinguished by names of inline and offline (or perpendicular) and C,D are capital letters of Common and Differential. So, l_D means differential degrees of freedom of recycling cavity, that is, Michelson fringe. There are five ports to pick up the light consisting error signals for the prototype. This prototype interferometer have two control scheme, independent control (phase-I) and common-differential control (phase-II). Both systems are summarized briefly in next section.

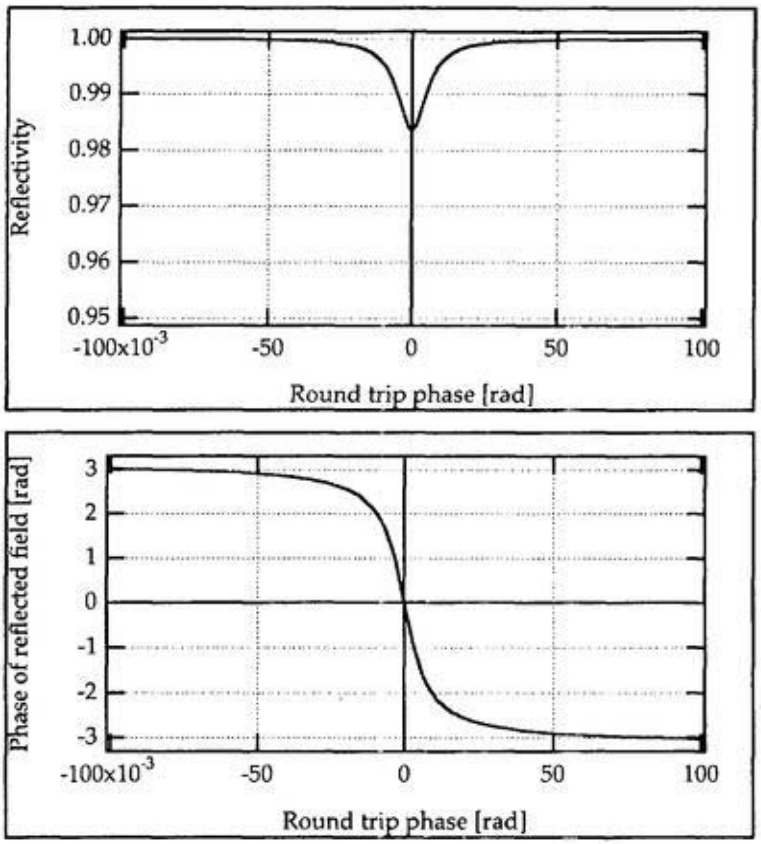

Figure 2.5: Squared response function and its phase with round trip phase.

Independent Control (Phase-I)

Prior to PRFPMI, 20m prototype was operated as FPMI, which requires control of three degrees of freedom; two arm cavity lengths and Michelson fringe. The error signals for both arm cavities are extracted from reflected lights of the cavities through the reflection from anti-reflection (AR) coatings of beam splitter. As an extension of this scheme, independent control scheme was adopted for phase-I locking method as is shown in Fig.2.6.

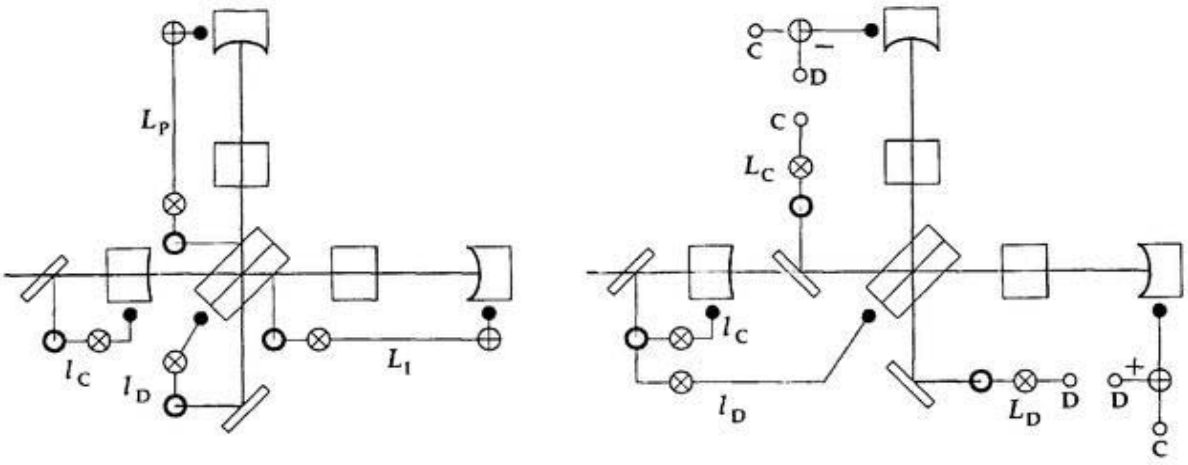

Figure 2.6: Independent Control (Phase-I) and Common-Differential Control (Phase-II).

Common Differential Control (Phase-II)

In contrast with independent control scheme, common- differential control scheme was developed by LIGO group as a final design of control scheme for full configured interferometer.[13] Here, two arm lengths are converted to common and differential degrees of freedom as

$$L_C = \frac{1}{2}(L_I + L_O) \tag{2.16}$$

$$L_D = \frac{1}{2}(L_I - L_O). \tag{2.17}$$

With these conversion, only independent basis of freedoms to be controlled were changed, so number of independent degrees of freedom are preserved. Three lights from reflected,

picked off and differential port are used for signal extraction with appropriate demodulation phase, in-phase and quadrature-phase.

2.4.3 Alignment Control

Generally, angular misalignment of the mirrors which consists of cavities can degrade the optical performance of the cavities. They will not only decrease the power buildup in the cavity but also increase the shot noise at the read out port of gravitational wave signals. Moreover, the decrease of the reflection and transmission efficiency of the arm cavities due to misalignment can be one of most serious problems with respect to the power enhancement inside the recycling cavity, in other words, recycling gain. With presence of misalignment of arm mirrors, the optical axis of cavity-reflected beam can be slightly different between off-resonance and on-resonance state, which will leads to serious contrast defect at the Michelson interferometer, for example, over a few percent.

As methods of alignment control, several schemes are proposed and tested by several interferometer experiment. The local control system such as optical lever, is relative easy to implement in contrast with global control system, such as Wave Front Sensing or Anderson method.[15, 16] Intrinsically, the reference of alignment control should be a input beam for the interferometer because any global reference frame can not be defined for interferometer itself. In this sense, some interferometric detection system, which can sense the higher modes of the Gaussian beam, is most promising candidate for alignment control system as a final detector configuration. In this sense, the wave front sensing technique are adopted for this experiment as an alignment control system.

Wave Front Sensing

As a solution of scalar wave equation for freely propagating laser beam to z-direction with paraxial approximation, the field distribution in two dimensional space can be expressed as

$$U_{m,n}(x,y,z) = U_m(x,z)U_n(y,z)e^{i(-kz+(m+n+1)\eta(z))}, \tag{2.18}$$

with

$$U_m(x,z) = \left(\frac{2}{\pi}\right)^{\frac{1}{4}} \left(\frac{1}{m!2^m w(z)}\right)^{\frac{1}{2}} H_m\left(\frac{\sqrt{2}x}{w(z)}\right) \exp\left[-\left\{\frac{1}{w(z)^2} + i\frac{k}{2R(z)}\right\}x^2\right], \tag{2.19}$$

where $\eta(z)$ is Guoy phase, $w(z)$ is beam size at the position z, $R(z)$ is the radius of curvature of wave front and H_l is Hermit polynomials of the order l. Rayleigh range $w(z)$ and Guoy phase $\eta(z)$ are given by

$$z_0 = \frac{\pi w_0^2}{\lambda}, \tag{2.20}$$

$$\eta(z) = \arctan\frac{z}{z_0}, \tag{2.21}$$

with w_0 is waist size and λ is wave length of the light.

For example, at z =0 the spatial distribution of the fundamental and first two higher order modes are

$$U_0(x) = \left(\frac{2}{\pi}\right)^{\frac{1}{4}}\left(\frac{1}{w_0}\right)^{\frac{1}{2}}\exp\left\{\frac{-x^2}{w_0^2}\right\} \tag{2.22}$$

$$U_1(x) = \left(\frac{2}{\pi}\right)^{\frac{1}{4}}\left(\frac{1}{w_0}\right)^{\frac{1}{2}}\left(\frac{2x}{w_0}\right)\exp\left\{\frac{-x^2}{w_0^2}\right\} \tag{2.23}$$

$$U_2(x) = \left(\frac{2}{\pi}\right)^{\frac{1}{4}}\left(\frac{1}{w_0}\right)^{\frac{1}{2}}\left(\sqrt{8}\left(\frac{x}{w_0}\right)^2 - 1\right)\exp\left\{\frac{-x^2}{w_0^2}\right\} \tag{2.24}$$

For the laterally displaced two fields by x_0,

$$E_1 = A_1\exp\left(-\frac{x^2}{w_0^2}\right)\mathrm{e}^{-ikz}, \tag{2.25}$$

$$E_2 = A_2\exp\left(-\frac{(x-x_0)^2}{w_0^2}\right)\mathrm{e}^{-ikz}. \tag{2.26}$$

E_2 can be expanded with optical frame of E_1 as follows.

$$E_2 \simeq A_2\exp\left(-\frac{x^2}{w_0^2}\right)\left\{1 - \left(\frac{x_0}{w_0}\right)\left(\frac{x}{w_0}\right) + \left(\frac{x_0}{w_0}\right)^2\left(\frac{1}{2}\left(\frac{x}{w_0}\right)^2 - 1\right)\right\}\mathrm{e}^{-ikz} \tag{2.27}$$

$$\simeq A_2\left\{\left(1 - \left(\frac{x_0}{w_0}\right)^2\left(1 - \frac{\sqrt{2}}{16}\right)\right)U_0 - \frac{1}{2}\left(\frac{x_0}{w_0}\right)U_1 - \frac{\sqrt{2}}{16}\left(\frac{x_0}{w_0}\right)^2 U_2\right\} \tag{2.28}$$

Similarly for the axially tilted fields,

$$E_2 = A_2\exp\left(-\frac{x^2}{w_0^2}\right)\mathrm{e}^{-2ik\theta_x}\mathrm{e}^{-ikz} \tag{2.29}$$

this can be expressed by superposition of series of higher order modes.

$$E_2 \simeq A_2\exp\left(-\frac{x^2}{w_0^2}\right)\left\{1 - i\left(\frac{\theta}{\theta_D}\right)\left(\frac{x}{w_0}\right) + \frac{1}{2}\left(\frac{\theta}{\theta_D}\right)^2\left(\frac{x}{w_0}\right)^2\right\}\mathrm{e}^{-ikz} \tag{2.30}$$

$$\simeq A_2\left\{\left(1 - \left(\frac{\theta}{\theta_D}\right)^2\left(1 - \frac{\sqrt{2}}{16}\right)\right)U_0 - \frac{i}{2}\left(\frac{\theta}{\theta_D}\right)U_1 - \frac{\sqrt{2}}{16}\left(\frac{\theta}{\theta_D}\right)^2 U_2\right\} \tag{2.31}$$

where θ_D is divergence angle defined as $\theta_D = \lambda/\pi w_0$. For the resonant optical cavity with slightly misaligned mirror(s), any misalignment of the optics cause lateral displacement and/or tilt of the optical axis of the cavity with respect to the incoming beam to the cavity. This means that expanded spatial distribution of the misaligned cavity with incoming beam axis contains higher order component in addition to the fundamental mode. In other words, the reflected light from any misaligned cavity can be expanded by superposition of the series of the Hermit- Gaussian modes if misalignment is sufficiently small as can be seen in Fig.2.7. These mode dispersions to higher order modes due to misalignment occur to phase

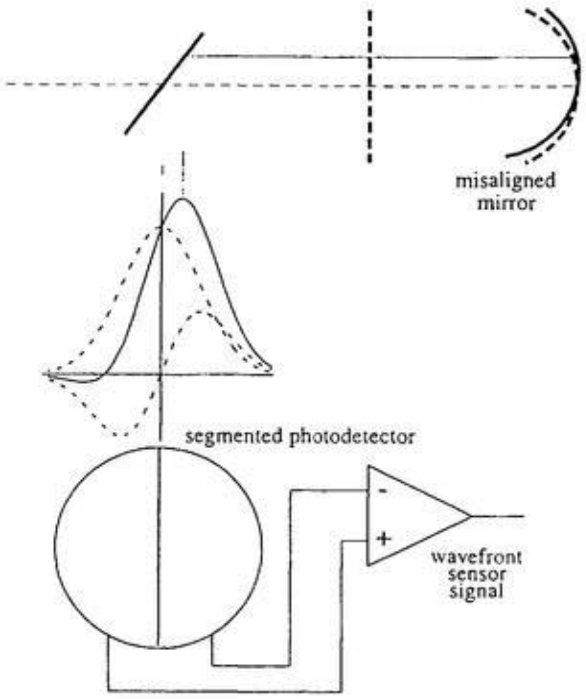

Figure 2.7: Mode decomposition of the light from misaligned cavity.[17]

modulation sidebands similarly, so the mode structure of the cavity can be simplified as Fig.2.8. This higher order spatial component, TEM_{10} mode, can be sensed with segmented photo detector by subtracting two halves plain signals each other. Further more, by using optical heterodyne technique, only the phase modulation frequency component of the field will be down converted to the DC signals to control the optics through demodulator. As a result, demodulated wave front sensor signal is superposition of beat between the TEM_{00} component of the carrier and TEM_{10} mode of the sidebands and the beat between TEM_{00}

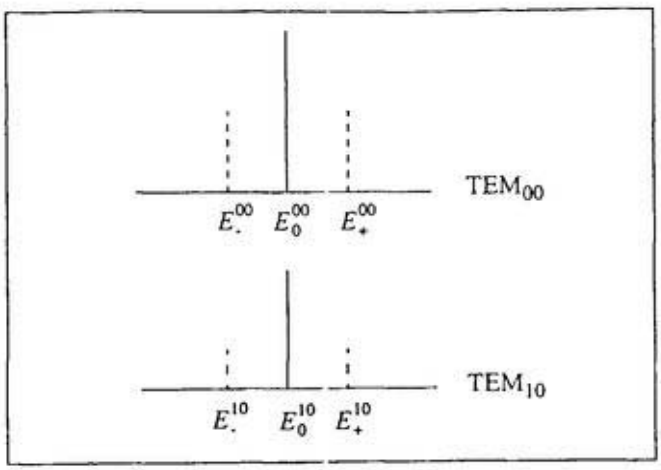

Figure 2.8: TEM_{00} and TEM_{10} modes of carrier and side bands.[17]

component of the sidebands and TEM_{10} mode of the carrier.

2.5 Signal Extraction for Length Control

2.5.1 Detection of Field

The light from the laser source E_0 is phase modulated at the frequency of Ω and then incident to the interferometer, which has the field form as

$$E_{inc} = E_0 e^{i\Gamma\cos(\Omega t)} \tag{2.32}$$

$$\simeq E_0\left[J_0(\Gamma) + iJ_1(\Gamma)e^{i\Omega t} + iJ_1(\Gamma)e^{-i\Omega t}\right], \tag{2.33}$$

for $\Gamma \ll 1$. The first term is called carrier (CR), while second and third term are phase modulated sidebands, upper side band (USB) and lower side band (LSB), respectively. The $J_i(\Gamma)$ are Bessel functions, which have values $J_0(\Gamma) \simeq 1$ and $J_1(\Gamma) = \Gamma/2$ for small modulation depth, $\Gamma \ll 1$. These three components of fields will experience different response through some optical system and will have the form of

$$E = \left[E_{CR} + E_{USB}e^{i\Omega t} + E_{LSB}e^{-i\Omega t}\right]e^{i\omega t} \tag{2.34}$$

at the any detection point of the system, where E_{CR}, E_{USB} and E_{LSB} are complex quantities in general. These fields can be detected with photo diode which have unity efficiency and converted to photo current as

$$i_{PD} = E \cdot E^* \tag{2.35}$$

$$= \left[|E_{CR}|^2 + |E_{USB}|^2 + |E_{LSB}|^2\right] \tag{2.36}$$

$$+ \left[(E_{CR}^* E_{USB} + E_{CR}E_{LSB}^*)e^{i\Omega t} + C.C.\right] \tag{2.37}$$

$$+ \left[(E_{USB}E_{LSB}^*)e^{2i\Omega t} + C.C.\right] \tag{2.38}$$

First term corresponds to DC-current and second term to oscillating component at frequency of Ω and third term to second harmonic component. By multiplying sinusoidal local reference at frequency Ω, only the second term will be down converted to DC signal and can be detected as signal. So, the output signal at the any detection points are

$$v_I(t) = \frac{1}{T}\int_{t-T}^{t}\left[(E_{CR}^* E_{USB} + E_{CR}E_{LSB}^*)e^{i\Omega t} + C.C.\right]e^{-i\vartheta_1}\cos(\Omega t + \vartheta_2)dt \tag{2.39}$$

$$= \Re\{(E_{CR}^* E_{USB} + E_{CR}E_{LSB}^*)e^{i\gamma}\} \tag{2.40}$$

where, ϑ_1 denote the phase shift from the point of the field calculation to practical photo diode and ϑ_2 denote the demodulation phase shift between phase modulating local oscillator and demodulating local oscillator. It is worth while to note that ϑ_1 and ϑ_2 have same effects on the demodulated signal, in other words, any optical phase shifts due to output optics can be compensated by demodulation phase. The combined demodulation phase γ in last line in eq.(2.40) play a important role for a signal separation of length sensing and wave front sensing of PRFPMI.

Then in-phase signal which is demodulated with local reference used for phase modulation is defined as

$$\begin{aligned} v_I &= \Re\{E^*_{CR}E_{USB}e^{i\gamma} + E_{CR}E^*_{LSB}e^{i\gamma}\} \\ &= \Re\{E_{CR}(E_{USB}e^{-i\gamma} + E_{LSB}e^{i\gamma})^*\} \\ &= \Im\{(H_{CR}(H_{USB}e^{-i\gamma} + H_{LSB}e^{i\gamma})^*)\}E_{CR}|E_{USB}| \end{aligned} \tag{2.41}$$

and quadrature signals become

$$\begin{aligned} v_Q &= \Im\{E^*_{CR}E_{USB}e^{i\gamma} + E_{CR}E^*_{LSB}e^{i\gamma}\} \\ &= \Im\{E_{CR}(E_{USB}e^{-i\gamma} - E_{LSB}e^{i\gamma})^*\} \\ &= -\Re\{(H_{CR}(H_{USB}e^{-i\gamma} - H_{LSB}e^{i\gamma})^*)\}E_{CR}|E_{USB}| \end{aligned} \tag{2.42}$$

where, $H_x$is a response function of corresponding field which is defined as

$$H_x = \frac{E_x}{E_x^{inc}} \tag{2.43}$$

So, it is convenient to omit these common factors, $E_{CR}|E_{USB}|$, for tractability and to redefine the normalized signals whose size does not depend on the intensity of the light source or modulation depth as follows.

$$v_I|_{\aleph} = \Im\{(H_{CR}(H_{USB}e^{-i\gamma} + H_{LSB}e^{i\gamma})^*)\} \tag{2.44}$$

$$v_Q|_{\aleph} = -\Re\{(H_{CR}(H_{USB}e^{-i\gamma} - H_{LSB}e^{i\gamma})^*)\} \tag{2.45}$$

If these fields are function of some free parameter, it is useful to define the derivative quantity with respect to the particular degree of freedom in order to quantify the size of signals. Suppose demodulated signals are functions of θ, the derivative of signal are

$$\frac{\partial v_I}{\partial\theta} = \Re\left\{\frac{\partial E_{CR}}{\partial\theta}(E_{USB} + E_{LSB})^* + E_{CR}\frac{\partial}{\partial\theta}(E_{USB} + E_{LSB})^*\right\} \tag{2.46}$$

$$= E^{INC}_{CR}|E^{INC}_{USB}|\Im\left\{\frac{\partial H_{CR}}{\partial\theta}(H_{USB} + H_{LSB})^* + H_{CR}\frac{\partial}{\partial\theta}(H_{USB} + H_{LSB})^*\right\} \tag{2.47}$$

$$\frac{\partial v_Q}{\partial \theta} = \Im\left\{\frac{\partial E_{CR}}{\partial \theta}(E_{USB} - E_{LSB})^* + E_{CR}\frac{\partial}{\partial \theta}(E_{USB} - E_{LSB})^*\right\} \tag{2.48}$$

$$= -E_{CR}^{INC}|E_{USB}^{INC}|\Re\left\{\frac{\partial H_{CR}}{\partial \theta}(H_{USB} - H_{LSB})^* + H_{CR}\frac{\partial}{\partial \theta}(H_{USB} - H_{LSB})^*\right\} \tag{2.49}$$

Then normalized signals have a form of

$$\left.\frac{\partial v_I}{\partial \theta}\right|_{\aleph} = \Im\left\{\frac{\partial H_{CR}}{\partial \theta}(H_{USB} + H_{LSB})^* + H_{CR}\frac{\partial}{\partial \theta}(H_{USB} + H_{LSB})^*\right\} \tag{2.50}$$

$$\left.\frac{\partial v_Q}{\partial \theta}\right|_{\aleph} = -\Re\left\{\frac{\partial H_{CR}}{\partial \theta}(H_{USB} - H_{LSB})^* + H_{CR}\frac{\partial}{\partial \theta}(H_{USB} - H_{LSB})^*\right\} \tag{2.51}$$

2.5.2 Signal Extraction

FP Cavity

For the simple Fabry-Perot optical cavity, all of the fields at anywhere can be written down analytically using mirror parameters and cavity parameter. The reflectivities and its sign, mirror separations are defined as is shown in Fig.2.9 The reflection efficiency,

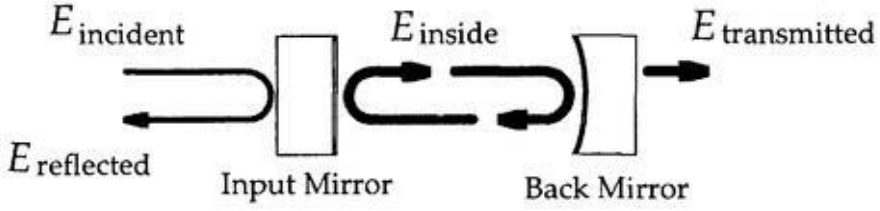

Figure 2.9: Fabry-Perot optical cavity and definition of its optical parameters.

transmission efficiency and internal fields of the cavity become as function of round trip phase $\Phi = 4\pi l/\lambda$,

$$\frac{E^{ref}}{E^{inc}} = H^{REF} = r_{IM} + \frac{t_{IM}^2 r_{BM} e^{-i\Phi}}{1 + r_{IM} r_{BM} e^{-i\Phi}} \equiv \sqrt{\eta_R} \tag{2.52}$$

$$\frac{E^{trans}}{E^{inc}} = H^{TRS} = \frac{t_{IM} t_{BM} e^{-i\Phi}}{1 + r_{IM} r_{BM} e^{-i\Phi}} \equiv \sqrt{\eta_T} \tag{2.53}$$

$$\frac{E^{ins}}{E^{inc}} = H^{INS} = \frac{t_{IM}}{1 + r_{IM} r_{BM} e^{-i\Phi}} \equiv g_{CAV} \tag{2.54}$$

For the carrier light, round trip phase is chosen so as the field to resonant, $\Phi_{CR}=\pi$, while for the sidebands, the phase are often chosen to be near anti-resonant , $\Phi_{USB}=0+\Psi$, $\Phi_{LSB}=0$ Ψ, for reflection locking technique. These condition is satisfied by designing free spectral range (FSR) of the cavity and modulation RF frequency properly. So, the transfer function of reflected light for the carrier and both side bands should be defined in general as

$$H_{CR}^{CAV} = r_{IM} - \frac{t_{IM}^2 r_{BM}}{1 - r_{IM} r_{BM}} \tag{2.55}$$

$$H_{USB}^{CAV} = r_{IM} + \frac{t_{IM}^2 r_{BM} e^{-i\Psi}}{1 + r_{IM} r_{BM} e^{-i\Psi}} \tag{2.56}$$

$$H_{LSB}^{CAV} = r_{IM} + \frac{t_{IM}^2 r_{BM} e^{i\Psi}}{1 + r_{IM} r_{BM} e^{i\Psi}} \tag{2.57}$$

From these expression, H_{CAV} of both side bands will have complex reflectivity for non-zero Ψ and will be reduced to pure real quantities only for $\Psi = 0$. In many cases, side band frequency is chosen to be center of n-th and (n+1)th FSR, just anti-resonant as is shown in fig.2.10. With these conditions, reflection efficiency for carrier and side bands become

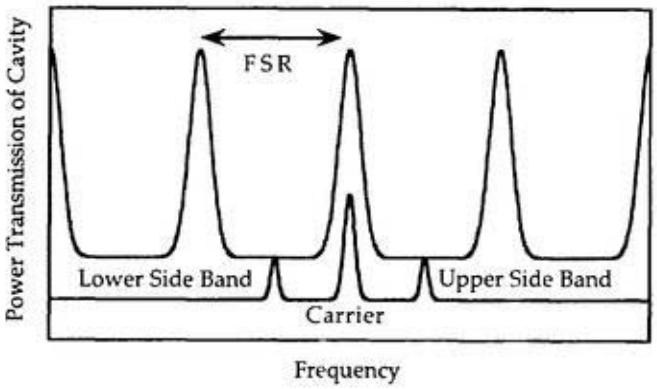

Figure 2.10: Free Spectral Range and RF side band frequency for FP cavity.

as follows,

$$H_{CR}^{REF} = r_{IM} - \frac{t_{IM}^2 r_{BM}}{1 - r_{IM} r_{BM}} \equiv -r_{reso} \tag{2.58}$$

$$H_{SB}^{REF} = r_{IM} + \frac{t_{IM}^2 r_{BM}}{1 + r_{IM} r_{BM}} \equiv -r_{anti} \tag{2.59}$$

In the same way, derivative of these fields of response functions with respect to the round trip phase can be defined. For example, reflection efficiency becomes

$$\frac{\partial}{\partial \Phi} \frac{E^{ref}}{E^{inc}} = \frac{-i t_{IM}^2 r_{BM} e^{-i\Phi}}{1 + r_{IM} r_{BM} e^{-i\Phi}}, \tag{2.60}$$

and by using round trip conditions,

$$\frac{\partial}{\partial \Phi} \frac{E_{CR}^{ref}}{E_{CR}^{inc}} = \frac{i t_{IM}^2 r_{BM}}{1 - r_{IM} r_{BM}} \equiv -r'_{reso} \tag{2.61}$$

$$\frac{\partial}{\partial \Phi} \frac{E_{USB}^{ref}}{E_{USB}^{inc}} = \frac{-i t_{IM}^2 r_{BM} e^{-i\Psi}}{1 + r_{IM} r_{BM} e^{-i\Psi}} \tag{2.62}$$

$$= \frac{-i t_{IM}^2 r_{BM}}{1 + r_{IM} r_{BM}} \equiv -r'_{anti} \tag{2.63}$$

$$\frac{\partial}{\partial \Phi} \frac{E_{LSB}^{ref}}{E_{LSB}^{inc}} = \frac{-i t_{IM}^2 r_{BM} e^{i\Psi}}{1 + r_{IM} r_{BM} e^{i\Psi}} \tag{2.64}$$

$$= \frac{-i t_{IM}^2 r_{BM}}{1 + r_{IM} r_{BM}} \equiv -r'_{anti}. \tag{2.65}$$

Using these expressions, the demodulated signals with in-phase from reflected light can be extracted as follows,

$$\left.\frac{\partial v_I}{\partial \Phi}\right|_{\aleph} = \Im \left\{ \frac{\partial H_{CR}^{ref}}{\partial \Phi} (H_{USB}^{ref} + H_{LSB}^{ref})^* + H_{CR}^{ref} \frac{\partial}{\partial \Phi} (H_{USB}^{ref} + H_{LSB}^{ref})^* \right\} \tag{2.66}$$

$$= 2\Im \left\{ r_{anti} r'_{reso} e^{i\gamma} - r_{reso} r'_{anti} e^{i\gamma} \right\} \tag{2.67}$$

$$= 2 \left\{ r_{anti} |r'_{reso}| e^{i\gamma} - r_{reso} |r'_{anti}| e^{i\gamma} \right\} \tag{2.68}$$

$$\rightarrow 2 \left\{ r_{anti} |r'_{reso}| - r_{reso} |r'_{anti}| \right\}. \tag{2.69}$$

Here, as the degree of freedom to be controlled is only Φ for length control, side bands phase shift from $\Phi = 0$ dose not have so much importance. Though this will cause the phase shift in signal, the demodulation phase γ should be adjusted to maximize the corresponding error signal.

Coupled Cavity

Before discussing the full configured interferometer, Power Recycled (PRFPMI), it is interesting to consider the coupled cavity. Additional mirror (Coupling Mirror:CM) in

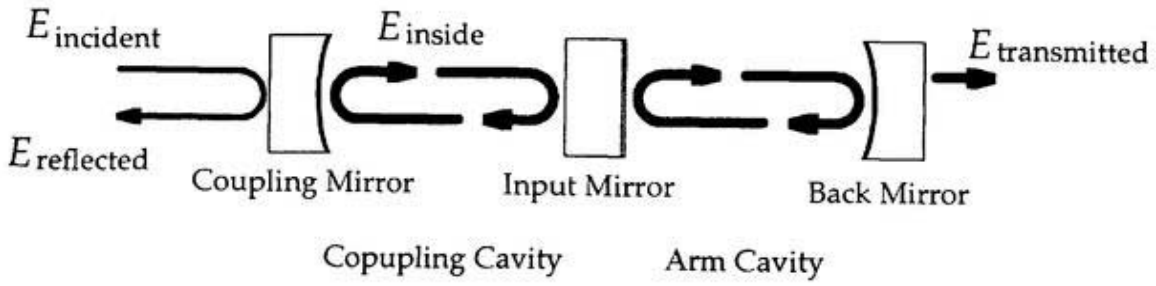

Figure 2.11: Optical configurations of Coupled Cavity and definition of its optical parameters.

front of the input mirror of FP cavity and input mirror compose a coupled cavity as is shown in Fig.2.11. What is interesting about coupled cavity is its complex response as an optical cavity because of its two combined FP cavities. In general, FP cavity composed of IM and BM can be regarded as a complicated reflection mirror in the meaning that it reflect the part of incident light according to its optical phase Φ. The reflection efficiency of the cavity as a function of optical phase is not linear to the phase, as is shown previous section. In this sense, the coupling cavity is also a FP cavity with compound back mirror as a FP cavity.

The way of calculating demodulated signal is same as for the FP cavity, except for the back mirror reflectivity; the reflectivity of back mirror should be substituted by round trip phase dependent FP reflection efficiency for constant reflectivity of single mirror. So, the response function of reflection light and field inside the coupling cavity are modified as follows;

$$H^{REF} = r_{CM} + \frac{t_{CM}^2 H^{RT}}{1 + r_{CM} H^{RT}} \tag{2.70}$$

$$= r_{CM} + \frac{t_{CM}^2 H^{CAV} \mathrm{e}^{-i\phi}}{1 + r_{CM} H^{CAV} \mathrm{e}^{-i\phi}} \tag{2.71}$$

$$H^{INS} = \frac{t_{CM}}{1 + r_{CM} H^{RT}} \tag{2.72}$$

$$= \frac{t_{CM}}{1 + r_{CM} H^{CAV} \mathrm{e}^{-i\phi}} \tag{2.73}$$

with

$$H^{RT} \equiv H^{CAV} \mathrm{e}^{-i\phi} \tag{2.74}$$

$$H^{CAV} = r_{IM} + \frac{t_{IM}^2 r_{BM} \mathrm{e}^{-i\Phi}}{1 + r_{IM} r_{BM} \mathrm{e}^{-i\Phi}} \tag{2.75}$$

where, H^{RT} denotes round trip response function inside the coupling cavity which contains round trip phase and reflection efficiency of the FP cavity.

As is same for arm cavity, it is interesting to introduce the phase offset for both side bands, due to length deviation of coupling cavity. For the coupling cavity, resonant condition for carrier becomes $\phi_{CR} = 0$ because the reflection efficiency of FP cavity H_{CR}^{CAV} is negative. And for both side bands, round trip phases are adopted as $\phi_{USB} = \pi + \psi$ and $\phi_{LSB} = \pi - \psi$ so, corresponding expressions are

$$H_{CR}^{CC} = r_{CM} + \frac{t_{CM}^2 H_{CR}^{CAV}}{1 + r_{CM} H_{CR}^{CAV}} \tag{2.76}$$

$$H_{USB}^{CC} = r_{CM} - \frac{t_{CM}^2 H_{USB}^{CAV} \mathrm{e}^{-i\psi}}{1 - r_{CM} H_{USB}^{CAV} \mathrm{e}^{-i\psi}} \tag{2.77}$$

$$H_{LSB}^{CC} = r_{CM} - \frac{t_{CM}^2 H_{LSB}^{CAV} \mathrm{e}^{i\psi}}{1 - r_{CM} H_{LSB}^{CAV} \mathrm{e}^{i\psi}}. \tag{2.78}$$

Note that H^{CAV} for side bands also contains Ψ as a degree of freedom, so, H^{CC} is a function of two parameters Ψ and ψ. With these preparations, normalized signals can be obtained as follows:

$$\left.\frac{\partial v_I^{ref}}{\partial \Phi}\right|_{\mathrm{R}} = \Im \left\{ \frac{\partial H_{CR}^{ref}}{\partial \Phi} (H_{USB}^{ref} \mathrm{e}^{-i\gamma} + H_{LSB}^{ref} \mathrm{e}^{i\gamma})^* \right. \tag{2.79}$$

$$\left. + H_{CR}^{ref} \frac{\partial}{\partial \Phi} (H_{USB}^{ref} \mathrm{e}^{-i\gamma} + H_{LSB}^{ref} \mathrm{e}^{i\gamma})^* \right\}. \tag{2.80}$$

In order to calculate this signal, some derivatives can be extracted as preparations.

$$\frac{\partial H_{CR}^{ref}}{\partial \Phi} = \frac{\partial H_{CR}^{RT}}{\partial \Phi} \frac{\partial H_{CR}^{ref}}{\partial H_{CR}^{RT}} \tag{2.81}$$

$$= \frac{\partial}{\partial H_{CR}^{RT}} \left(r_{CM} + \frac{t_{CM}^2 H_{CR}^{RT}}{1 + r_{CM} H_{CR}^{RT}} \right) \frac{\partial}{\partial \Phi} H_{CR}^{CAV} \mathrm{e}^{-i\phi} \tag{2.82}$$

$$= -g_{CR}^2 r_{CR}^{\prime CAV} \tag{2.83}$$

$$\frac{\partial H_{USB}^{ref}}{\partial \Phi} = -g_{USB}^2 r_{USB}^{\prime CAV} \mathrm{e}^{-i\psi} \tag{2.84}$$

$$\frac{\partial H_{LSB}^{ref}}{\partial \Phi} = -g_{LSB}^2 r_{LSB}^{\prime CAV} \mathrm{e}^{i\psi} \tag{2.85}$$

where,

$$g_{CR} = \frac{t_{CM}}{1 + r_{CM} H_{CR}^{RT}} = \frac{t_{CM}}{1 - r_{CM} r_{CR}^{CAV}} \tag{2.86}$$

$$g_{USB} = \frac{t_{CM}}{1 + r_{CM} H_{USB}^{RT}} = \frac{t_{CM}}{1 + r_{CM} r_{USB}^{CAV}} \tag{2.87}$$

$$g_{LSB} = \frac{t_{CM}}{1 + r_{CM} H_{LSB}^{RT}} = \frac{t_{CM}}{1 + r_{CM} r_{LSB}^{CAV}}. \tag{2.88}$$

For coupled cavity, two control signals for Φ and ϕ are expected from two different picked off light, reflected and picked off light from coupling cavity. The four signals extracted from reflected and picked off light with respect to Φ and ϕ can be calculated in the same manner as for the FP cavity and resulting expressions are

$$\left.\frac{\partial v_I^{REF}}{\partial \Phi}\right|_{\aleph} = \Im\left\{ g_{CR}^2 r_{CR}^{\prime CAV} \left(r_{USB}^{CC} e^{i\gamma} + r_{LSB}^{CC} e^{-i\gamma} \right)^* \right. \tag{2.89}$$

$$\left. + r_{CR}^{CC} \left(g_{USB}^2 r_{USB}^{\prime CAV} e^{-i\psi} e^{i\gamma} + g_{LSB}^2 r_{LSB}^{\prime CAV} e^{i\psi} e^{-i\gamma} \right)^* \right\}$$

$$\rightarrow -2 \left(g_{CR}^2 |r_{CR}^{\prime CAV}| r_{SB}^{CC} + g_{SB}^2 r_{CR}^{CC} |r_{SB}^{\prime CAV}| \right) \tag{2.90}$$

$$\left.\frac{\partial v_I^{REF}}{\partial \phi}\right|_{\aleph} = \Im\left\{ -i g_{CR}^2 r_{CR}^{CAV} \left(r_{USB}^{CC} e^{i\gamma} + r_{LSB}^{CC} e^{-i\gamma} \right)^* \right. \tag{2.91}$$

$$\left. - r_{CR}^{CC} \left(i g_{USB}^2 r_{USB}^{CAV} e^{-i\psi} e^{i\gamma} + i g_{LSB}^2 r_{LSB}^{CAV} e^{i\psi} e^{-i\gamma} \right)^* \right\}$$

$$\rightarrow -2 \left(g_{CR}^2 r_{CR}^{CAV} r_{SB}^{CC} + g_{SB}^2 r_{CR}^{CC} r_{SB}^{CAV} \right) \tag{2.92}$$

$$\left.\frac{\partial v_I^{PCK}}{\partial \Phi}\right|_{\aleph} = \Im\left\{ \frac{1}{t_{CM}} g_{CR}^2 r_{CR}^{\prime CAV} \left(g_{USB} r_{USB}^{CAV} e^{-i\psi} e^{i\gamma} + g_{LSB} r_{LSB}^{CAV} e^{i\psi} e^{-i\gamma} \right)^* \right. \tag{2.93}$$

$$\left. + g_{CR} r_{CR}^{CAV} \left(\frac{1}{t_{CM}} g_{USB}^2 r_{USB}^{CAV} e^{-i\psi} e^{i\gamma} + \frac{1}{t_{CM}} g_{LSB}^2 r_{LSB}^{CAV} e^{i\psi} e^{-i\gamma} \right)^* \right\}$$

$$\rightarrow \frac{2}{t_{CM}} \left(g_{CR}^2 g_{SB} |r_{CR}^{\prime CAV}| r_{SB}^{CAV} - g_{CR} g_{SB}^2 r_{CR}^{CAV} |r_{SB}^{\prime CAV}| \right) \tag{2.94}$$

$$\left.\frac{\partial v_I^{PCK}}{\partial \phi}\right|_{\aleph} = \Im\left\{ \frac{i}{t_{CM}} g_{CR}^2 r_{CR}^{\prime CAV} \left(g_{USB} r_{USB}^{CAV} e^{-i\psi} e^{i\gamma} + g_{LSB} r_{LSB}^{CAV} e^{i\psi} e^{-i\gamma} \right)^* \right. \tag{2.95}$$

$$\left. + g_{CR} r_{CR}^{CAV} \left(\frac{i}{t_{CM}} g_{USB}^2 r_{USB}^{CAV} e^{-i\psi} e^{i\gamma} + \frac{i}{t_{CM}} g_{LSB}^2 r_{LSB}^{CAV} e^{i\psi} e^{-i\gamma} \right)^* \right\}$$

$$\rightarrow \frac{2}{t_{CM}} g_{CR} g_{SB} \left(g_{CR} - g_{SB} \right) r_{CR}^{CAV} r_{SB}^{CAV} \tag{2.96}$$

The reduced signals for Ψ=ψ=0 are also shown after right arrows in the last line of each expressions. In the case that optical system is perfectly symmetric, that is, ψ=0 and Ψ=0, each signals will be maximized with demodulation phase offset from in-phase γ=0 and

signal separation matrix will become

$$\begin{pmatrix} \left.\frac{\partial v_I^{REF}}{\partial \Phi}\right|_{\aleph} & \left.\frac{\partial v_I^{REF}}{\partial \phi}\right|_{\aleph} \\ \left.\frac{\partial v_I^{PCK}}{\partial \Phi}\right|_{\aleph} & \left.\frac{\partial v_I^{PCK}}{\partial \phi}\right|_{\aleph} \end{pmatrix} \tag{2.97}$$

$$= \begin{pmatrix} -2\left(g_{CR}^2 |r_{CR}^{\prime CAV}| r_{SB}^{CC} + g_{SB}^2 r_{CR}^{CC} |r_{SB}^{\prime CAV}|\right) \\ \frac{2}{t_{CM}}\left(g_{CR}^2 g_{SB} |r_{CR}^{\prime CAV}| r_{SB}^{CAV} - g_{CR} g_{SB}^2 r_{CR}^{CAV} |r_{SB}^{\prime CAV}|\right) \end{pmatrix} \tag{2.98}$$

$$\begin{pmatrix} -2\left(g_{CR}^2 r_{CR}^{CAV} r_{SB}^{CC} + g_{SB}^2 r_{CR}^{CC} r_{SB}^{CAV}\right) \\ \frac{2}{t_{CM}} g_{CR} g_{SB}\left(g_{CR} - g_{SB}\right) r_{CR}^{CAV} r_{SB}^{CAV} \end{pmatrix} \tag{2.99}$$

$$\tag{2.100}$$

This matrix is numerically,

$$\begin{array}{c} \\ \partial v_I^{REF}(\eta = 0) \\ \partial v_I^{PCK}(\eta = 0) \end{array} \begin{array}{c} \begin{array}{cc} \partial\Phi & \partial\phi \end{array} \\ \begin{pmatrix} 1.98 \times 10^4 & 3.9 \times 10^1 \\ 9.80 \times 10^5 & 2.35 \times 10^3 \end{pmatrix} \end{array} = \begin{pmatrix} 1 & -2.2 \times 10^{-3} \\ 1 & 2.42 \times 10^{-3} \end{pmatrix}. \tag{2.101}$$

This matrix means that signals for two degrees of freedom, Φ and ϕ are mixing in both reflected and picked off light and for both demodulated signals, the error signal of Φ is dominant over that of ϕ. In other words, two error signals does not separate. In principal, two independent error signals can control two degrees of freedom even if they are completely mixing as far as control system is concerned. But as a practical problem, if one of signals are extremely small compared with others, control servo system have to compensate this gain gap with electronical gain. In order to realize stable control system and operation, error signals should be separated as much as possible.

On the other hand, if the optical system is not symmetric especially for the sidebands, the round trip phase Ψ does not match 0 which leads reflection efficiency of FP cavity complex for both sidebands. This take effects on the phase of sidebands inside the coupling cavity and change the right angle relation between carrier and sidebands fields in a complex plain. So, the complex vector in the bracket of signals in Eqn.2.57-2.57 will be rotated due to Ψ and complex vectors in the bracket of differentiated signals Eqn.2.90-2.96 can have different complex arguments. The resulting magnitude of signals are drown in Fig.2.12,2.13 with demodulation phase in horizontal axis. Notice that optimum phases which maximize the corresponding signal are different for two degree of freedom in one of detected light. Making use of this phase offset, any signal can be separated by choosing the demodulation phase at which another signal will vanish.

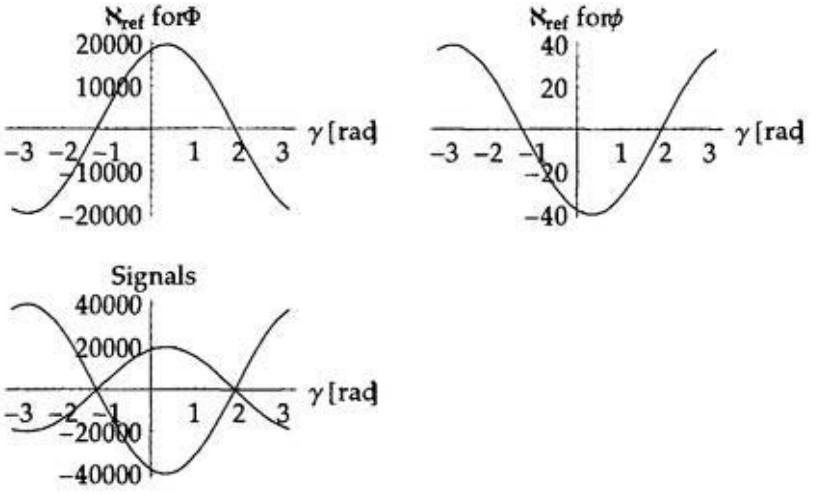

Figure 2.12: Magnitude of two signals for Φ and ϕ from reflected light of coupled cavity.

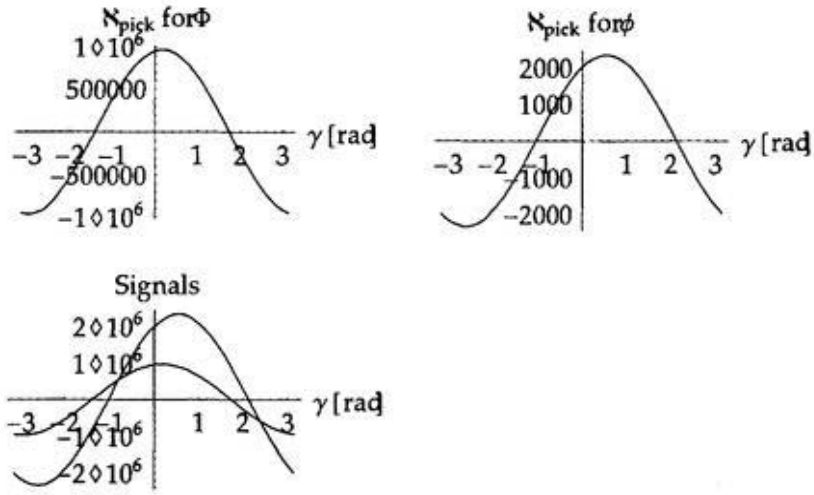

Figure 2.13: Magnitude of two signals for Φ and ϕ from picked off light of coupling cavity.

These effect can be caused also by changing the length of the coupling cavity. As the length is chosen to be the quarter of the wavelength of modulation frequency, sideband components are also resonant in the coupling cavity as well as carrier. So, the length change of the cavity from the side band resonance condition means side bands resonance at the shoulder of the resonance line shape. This "shoulder locking" is thought not to be preferable because side bands fields become very sensitive to the its position in a resonance line shape with respect to the FM-AM conversion. Though these expressions contain a free parameter ψ as a coupling cavity length deviation from the specific length, this should not be used for signal separation calculation but for the imperfection study.

As a result, the signal separation matrix become

$$\begin{array}{cc} & \begin{array}{cc} \partial\Phi & \partial\phi \end{array} \\ \begin{array}{c} \partial v_I^{REF}(\eta = 0.34) \\ \partial v_I^{PCK}(\eta = 1.74) \end{array} & \begin{pmatrix} 1.98 \times 10^4 & -3.99 \times 10^1 \\ 1.74 \times 10^0 & 8.60 \times 10^2 \end{pmatrix} = \begin{pmatrix} 1 & -2.02 \times 10^{-3} \\ 1.98 \times 10^{-3} & 1 \end{pmatrix} \end{array}$$

for $\Psi=\pi/3$ and $\psi=0$ condition, which is the case of the arm cavity of 20m prototype interferometer and its modulation frequency. As can be seen, two error signals for Φ and ϕ are almost completely separated. The same effect was suggested by S. Miyoki by tuning the coupling cavity length.

PRFPMI

Optical configuration of full configured interferometer, Power Recycled Fabry-Pérot Michelson Interferometer is shown in Fig. 2.14. Basically, the interferometer can be regarded as coupled cavity which consists of arm cavities and recycling cavity except for the two-way splitting by beam splitter within a recycling cavity. So the way of calculation for signal separation is analogues to that of coupled cavity. Major difference between them is that round trip response function of internal field of the recycling cavity will be superposition of that for the inline arm cavity and offline arm cavity. As this optical system, PRFPMI, contains Michelson part at which the fields reflected from both arm cavities will be optically recombined and interfere, some field will go back toward the light source while other will leak out to the differential output port. Following these modification of the system, two additional response functions for Michelson part can be defined: common and differential round trip response function.

$$H^{COM} \equiv \frac{E^{ret}}{E^{ins}} \tag{2.102}$$

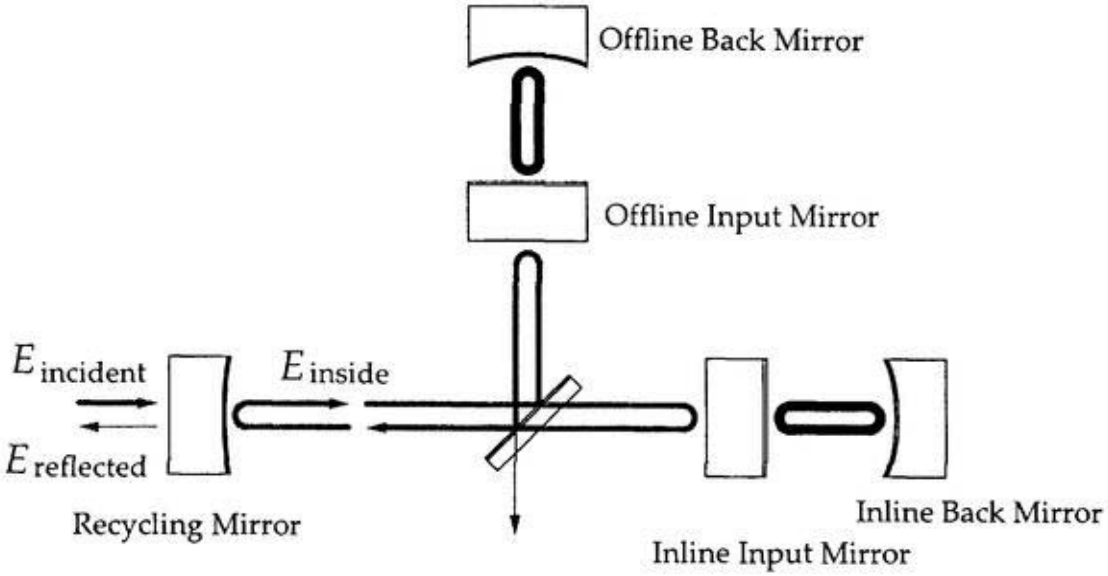

Figure 2.14: Schematic diagram of configuration and definition of circulating fields inside interferometer.

$$
\begin{aligned}
&= \frac{1}{2}\left\{H^{OFCAV}\mathrm{e}^{-i\phi^{OF}} + H^{INCAV}\mathrm{e}^{-i\phi^{IN}}\right\} \\
H^{DIF} &\equiv \frac{E^{ant}}{E^{ins}} \\
&= \frac{1}{2}\left\{H^{OFCAV}\mathrm{e}^{-i\phi^{OF}} - H^{INCAV}\mathrm{e}^{-i\phi^{IN}}\right\}
\end{aligned}
\tag{2.103}
$$

With well balanced interferometer, the differential output is kept dark fringe for the carrier light at operation, which means perfect interference at the beam splitter. However, practical interferometer have many imperfections, for example, slight misalignment of the arm cavity mirrors due to DC offset and/or to resonance motion of the suspension system or imperfections of optics. These are most possible hosts which can cause imperfect interference at BS and interference efficiency is fluctuating with about a few percent stationary even in the midnight at the site of Tokyo. From these point of view, it is important to take its effect into account to the field expression for signal separation calculation in order to simulate as much realistic as possible. It is not easy to fully formalize the interference efficiency because its mechanism have not been investigated closely. So, only leak out effect to the differential port is adopted in these series of calculations.

The response functions which are used in later full calculations are modified as follows for carrier and both side bands,

$$H^{COM}_{CR} = \frac{E^{ret}_{CR}}{E^{ins}_{CR}} = -r^{CAV}_{CR}\cos\mathcal{E}_{CR} \tag{2.104}$$

$$H^{DIF}_{CR} = \frac{E^{ant}_{CR}}{E^{ins}_{CR}} = -r^{CAV}_{CR}\sin\mathcal{E}_{CR} \tag{2.105}$$

$$H^{COM}_{USB} = \frac{E^{ret}_{USB}}{E^{ins}_{USB}} = -r^{CAV}_{USB}\mathrm{e}^{-i\psi}\cos\alpha_{USB} \tag{2.106}$$

$$H^{DIF}_{USB} = \frac{E^{ant}_{USB}}{E^{ins}_{USB}} = ir^{CAV}_{USB}\mathrm{e}^{-i\psi}\sin\alpha_{USB} \tag{2.107}$$

$$H^{COM}_{LSB} = \frac{E^{ret}_{LSB}}{E^{ins}_{LSB}} = -r^{CAV}_{LSB}\mathrm{e}^{i\psi}\cos\alpha_{LSB} \tag{2.108}$$

$$H^{DIF}_{LSB} = \frac{E^{ant}_{LSB}}{E^{ins}_{LSB}} = -ir^{CAV}_{LSB}\mathrm{e}^{i\psi}\sin\alpha_{LSB} \tag{2.109}$$

where, $\alpha_{USB} = \alpha + \mathcal{E}_{USB}$ and $\alpha_{USB} = \alpha + \mathcal{E}_{USB}$ with $\mathcal{E}$ denoting a interference efficiency. In these definition, 0.23 [rad] of $\mathcal{E}$ corresponds to the 1% of degradation of interference efficiency.

Of course, expressions for reflected and internal fields of PRFPMI response functions are

modified using these common round trip response function.

$$H^{REF} = \frac{E^{ref}}{E^{inc}} = r_{REC} + \frac{t_{REC}^2 H^{COM}}{1 + r_{REC} H^{COM}} \tag{2.110}$$

$$H^{INS} = \frac{E^{ins}}{E^{inc}} = \frac{t_{REC}}{1 + r_{REC} H^{COM}} \tag{2.111}$$

And these functions take the forms for carrier and sidebands as

$$H_{CR}^{REF} = r_{REC} - \frac{t_{REC}^2 r_{CR}^{CAV} \cos\mathcal{E}_{CR}}{1 - r_{REC} r_{CR}^{CAV} \cos\mathcal{E}_{CR}} \equiv -r_{CR}^{PRFPMI} \tag{2.112}$$

$$H_{USB}^{REF} = r_{REC} + \frac{t_{REC}^2 r_{USB}^{CAV} e^{-i\psi} \cos\alpha_{USB}}{1 + r_{REC} r_{USB}^{CAV} e^{-i\psi} \cos\alpha_{USB}} \equiv -r_{USB}^{PRFPMI} \tag{2.113}$$

$$H_{LSB}^{REF} = r_{REC} + \frac{t_{REC}^2 r_{LSB}^{CAV} e^{i\psi} \cos\alpha_{LSB}}{1 + r_{REC} r_{LSB}^{CAV} e^{i\psi} \cos\alpha_{LSB}} \equiv -r_{LSB}^{PRFPMI} \tag{2.114}$$

$$H_{CR}^{INS} = \frac{t_{REC}}{1 - r_{REC} r_{CR}^{CAV} \cos\mathcal{E}_{CR}} \equiv g_{CR} \tag{2.115}$$

$$H_{USB}^{INS} = \frac{t_{REC}}{1 + r_{REC} r_{USB}^{CAV} e^{-i\psi} \cos\alpha_{USB}} \equiv g_{USB} \tag{2.116}$$

$$H_{LSB}^{INS} = \frac{t_{REC}}{1 + r_{REC} r_{LSB}^{CAV} e^{i\psi} \cos\alpha_{LSB}} \equiv g_{LSB} \tag{2.117}$$

Using these definitions, differentiate error signals from reflected, picked off and differential light with respect to common and differential degrees of freedom of arm cavity length Φ_{COM}, Φ_{DIF} and recycling cavity length ϕ_{COM}, ϕ_{DIF} can be calculated as follows,

$$\begin{aligned}\left.\frac{\partial v_I^{ref}}{\partial \Phi_{COM}}\right|_R = \Im\Big\{ & \frac{1}{2} g_{CR}^2 r_{CR}'^{CAV} \cos\mathcal{E}_{CR} \left(r_{USB}^{PRFPMI} e^{i\gamma} + r_{LSB}^{PRFPMI} e^{-i\gamma} \right)^* \\ & - \frac{1}{2} r_{CR}^{PRFPMI} \left(g_{USB}^2 r_{USB}'^{CAV} \cos\alpha_{USB} e^{-i\psi} e^{i\gamma} \right. \\ & \left. + g_{LSB}^2 r_{LSB}'^{CAV} \cos\alpha_{LSB} e^{i\psi} e^{-i\gamma} \right)^* \Big\} \\ \rightarrow & -g_{CR}^2 |r_{CR}'^{CAV}| r_{SB}^{PRFPMI} + g_{SB}^2 |r_{SB}'^{CAV}| r_{CR}^{PRFPMI} \cos\alpha_{SB}\end{aligned} \tag{2.118}$$

$$\begin{aligned}\left.\frac{\partial v_I^{ref}}{\partial \Phi_{DIF}}\right|_R = \Im\Big\{ & -\frac{1}{2} g_{CR}^2 r_{CR}'^{CAV} \sin\mathcal{E}_{CR} \left(-r_{USB}^{PRFPMI} e^{i\gamma} - r_{LSB}^{PRFPMI} e^{-i\gamma} \right)^* \\ & + \frac{1}{2} r_{CR}^{PRFPMI} \left(i g_{USB}^2 r_{USB}'^{CAV} \sin\alpha_{USB} e^{-i\psi} e^{i\gamma} \right. \\ & \left. + i g_{LSB}^2 r_{LSB}'^{CAV} \sin\alpha_{LSB} e^{i\psi} e^{-i\gamma} \right)^* \Big\} \\ \rightarrow & \ 0\end{aligned} \tag{2.119}$$

$$\left.\frac{\partial v_I^{ref}}{\partial \phi_{COM}}\right|_{\aleph} = \Im\left\{-\frac{i}{2}g_{CR}^2 r_{CR}^{CAV}\cos\mathcal{E}_{CR}\left(r_{USB}^{PRFPMI}e^{i\gamma}+r_{LSB}^{PRFPMI}e^{-i\gamma}\right)^*\right.$$
$$+\frac{1}{2}r_{CR}^{PRFPMI}\left(ig_{USB}^2 r_{USB}^{CAV}\cos\alpha_{USB}e^{-i\psi}e^{i\gamma}\right.$$
$$\left.\left.+ig_{LSB}^2 r_{LSB}^{CAV}\cos\alpha_{LSB}e^{i\psi}e^{-i\gamma}\right)^*\right\}$$
$$\rightarrow -g_{CR}^2 r_{CR}^{CAV} r_{SB}^{PRFPMI} - g_{SB}^2 r_{CR}^{PRFPMI} r_{SB}^{CAV}\cos\alpha_{SB} \tag{2.120}$$

$$\left.\frac{\partial v_I^{ref}}{\partial \phi_{DIF}}\right|_{\aleph} = \Im\left\{\frac{i}{2}g_{CR}^2 r_{CR}^{CAV}\sin\mathcal{E}_{CR}\left(-r_{USB}^{PRFPMI}e^{i\gamma}-r_{LSB}^{PRFPMI}e^{-i\gamma}\right)^*\right.$$
$$+\frac{1}{2}r_{CR}^{PRFPMI}\left(g_{USB}^2 r_{USB}^{CAV}\sin\alpha_{USB}e^{-i\psi}e^{i\gamma}\right.$$
$$\left.\left.-g_{LSB}^2 r_{LSB}^{CAV}\sin\alpha_{LSB}e^{i\psi}e^{-i\gamma}\right)^*\right\}$$
$$\rightarrow 0 \tag{2.121}$$

$$\left.\frac{\partial v_Q^{ref}}{\partial \Phi_{COM}}\right|_{\aleph} = -\Re\left\{\frac{1}{2}g_{CR}^2 r_{CR}^{\prime CAV}\cos\mathcal{E}_{CR}\left(r_{USB}^{PRFPMI}e^{i\gamma}-r_{LSB}^{PRFPMI}e^{-i\gamma}\right)^*\right.$$
$$-\frac{1}{2}r_{CR}^{PRFPMI}\left(g_{USB}^2 r_{USB}^{\prime CAV}\cos\alpha_{USB}e^{-i\psi}e^{i\gamma}\right.$$
$$\left.\left.+g_{LSB}^2 r_{LSB}^{\prime CAV}\cos\alpha_{LSB}e^{i\psi}e^{-i\gamma}\right)^*\right\}$$
$$\rightarrow 0 \tag{2.122}$$

$$\left.\frac{\partial v_Q^{ref}}{\partial \Phi_{DIF}}\right|_{\aleph} = -\Re\left\{-\frac{1}{2}g_{CR}^2 r_{CR}^{\prime CAV}\sin\mathcal{E}_{CR}\left(-r_{USB}^{PRFPMI}e^{i\gamma}+r_{LSB}^{PRFPMI}e^{-i\gamma}\right)^*\right.$$
$$+\frac{1}{2}r_{CR}^{PRFPMI}\left(ig_{USB}^2 r_{USB}^{\prime CAV}\sin\alpha_{USB}e^{-i\psi}e^{i\gamma}\right.$$
$$\left.\left.+ig_{LSB}^2 r_{LSB}^{\prime CAV}\sin\alpha_{LSB}e^{i\psi}e^{-i\gamma}\right)^*\right\}$$
$$\rightarrow g_{CR}^2|r_{CR}^{\prime CAV}|r_{SB}^{PRFPMI}\sin\alpha_{SB} \tag{2.123}$$

$$\left.\frac{\partial v_Q^{ref}}{\partial \phi_{COM}}\right|_{\aleph} = -\Re\left\{-\frac{i}{2}g_{CR}^2 r_{CR}^{CAV}\cos\mathcal{E}_{CR}\left(r_{USB}^{PRFPMI}e^{i\gamma}-r_{LSB}^{PRFPMI}e^{-i\gamma}\right)^*\right.$$
$$+\frac{1}{2}r_{CR}^{PRFPMI}\left(ig_{USB}^2 r_{USB}^{CAV}\cos\alpha_{USB}e^{-i\psi}e^{i\gamma}\right.$$
$$\left.\left.+ig_{LSB}^2 r_{LSB}^{CAV}\cos\alpha_{LSB}e^{i\psi}e^{-i\gamma}\right)^*\right\}$$
$$\rightarrow 0 \tag{2.124}$$

$$\left.\frac{\partial v_Q^{ref}}{\partial \phi_{DIF}}\right|_{\Re} = -\Re\left\{\frac{i}{2}g_{CR}^2 r_{CR}^{CAV}\sin\mathcal{E}_{CR}\left(-r_{USB}^{PRFPMI}e^{i\gamma}+r_{LSB}^{PRFPMI}e^{-i\gamma}\right)^*\right.$$
$$+\frac{1}{2}r_{CR}^{PRFPMI}\left(g_{USB}^2 r_{USB}^{CAV}\sin\alpha_{USB}e^{-i\psi}e^{i\gamma}\right.$$
$$\left.\left.+g_{LSB}^2 r_{LSB}^{CAV}\sin\alpha_{LSB}e^{i\psi}e^{-i\gamma}\right)^*\right\}$$
$$\rightarrow -g_{SB}^2 r_{CR}^{PRFPMI} r_{SB}^{CAV}\sin\alpha_{SB} \tag{2.125}$$

$$\left.\frac{\partial v_Q^{asy}}{\partial \Phi_{COM}}\right|_{\Re} = -\Re\left\{\left(-\frac{r_{rec}}{2t_{rec}}g_{CR}^2 r_{CR}^{CAV} r_{CR}^{\prime CAV}\sin\mathcal{E}_{CR}\cos\mathcal{E}_{CR}+\frac{1}{2}g_{CR}r_{CR}^{\prime CAV}\sin\mathcal{E}_{CR}\right)\right.$$
$$\left(ig_{USB}r_{USB}^{CAV}\sin\alpha_{USB}e^{-i\psi}e^{i\gamma}+ig_{LSB}r_{LSB}^{CAV}\sin\alpha_{LSB}e^{i\psi}e^{-i\gamma}\right)^*$$
$$-g_{CR}r_{CR}^{CAV}\sin\mathcal{E}_{CR}$$
$$\left\{\left(-\frac{ir_{rec}}{2t_{rec}}g_{USB}^2 r_{USB}^{CAV} r_{USB}^{\prime CAV}\sin\alpha_{USB}\cos\alpha_{USB}e^{-2i\psi}+\frac{i}{2}g_{USB}r_{USB}^{\prime CAV}\sin\alpha_{USB}e^{-i\psi}\right)e^{i\gamma}\right.$$
$$\left.\left.-\left(\frac{ir_{rec}}{2t_{rec}}g_{LSB}^2 r_{LSB}^{CAV} r_{LSB}^{\prime CAV}\sin\alpha_{LSB}\cos\alpha_{LSB}e^{2i\psi}-\frac{i}{2}g_{LSB}r_{LSB}^{\prime CAV}\sin\alpha_{LSB}e^{i\psi}\right)e^{-i\gamma}\right\}^*\right\}$$
$$\rightarrow 0 \tag{2.126}$$

$$\left.\frac{\partial v_Q^{asy}}{\partial \Phi_{DIF}}\right|_{\Re} = -\Re\left\{\left(-\frac{r_{rec}}{2t_{rec}}g_{CR}^2 r_{CR}^{CAV} r_{CR}^{\prime CAV}\sin^2\mathcal{E}_{CR}+\frac{1}{2}g_{CR}r_{CR}^{\prime CAV}\cos\mathcal{E}_{CR}\right)\right.$$
$$\left(ig_{USB}r_{USB}^{CAV}\sin\alpha_{USB}e^{-i\psi}e^{i\gamma}+ig_{LSB}r_{LSB}^{CAV}\sin\alpha_{LSB}e^{i\psi}e^{-i\gamma}\right)^*$$
$$+\frac{1}{2}g_{CR}r_{CR}^{CAV}\sin\mathcal{E}_{CR}$$
$$\left\{\left(\frac{r_{rec}}{t_{rec}}g_{USB}^2 r_{USB}^{CAV} r_{USB}^{\prime CAV}\sin^2\alpha_{USB}e^{-2i\psi}+g_{USB}r_{USB}^{\prime CAV}\cos\alpha_{USB}e^{-i\psi}\right)e^{i\gamma}\right.$$
$$\left.\left.-\left(\frac{r_{rec}}{t_{rec}}g_{LSB}^2 r_{LSB}^{CAV} r_{LSB}^{\prime CAV}\sin^2\alpha_{LSB}e^{2i\psi}+g_{LSB}r_{LSB}^{\prime CAV}\cos\alpha_{LSB}e^{i\psi}\right)e^{-i\gamma}\right\}^*\right\}$$
$$\rightarrow g_{CR}g_{SB}r_{SB}^{CAV}|r_{CR}^{\prime CAV}|\sin\alpha_{SB} \tag{2.127}$$

$$\left.\frac{\partial v_Q^{asy}}{\partial \phi_{COM}}\right|_{\Re} = -\Re\left\{\left(\frac{ir_{rec}}{2t_{rec}}g_{CR}^2 r_{CR}^{CAV} r_{CR}^{CAV}\sin\mathcal{E}_{CR}\cos\mathcal{E}_{CR}-\frac{i}{2}g_{CR}r_{CR}^{CAV}\sin\mathcal{E}_{CR}\right)\right.$$
$$\left(ig_{USB}r_{USB}^{CAV}\sin\alpha_{USB}e^{-i\psi}e^{i\gamma}+ig_{LSB}r_{LSB}^{CAV}\sin\alpha_{LSB}e^{i\psi}e^{-i\gamma}\right)^*$$
$$-g_{CR}r_{CR}^{CAV}\sin\mathcal{E}_{CR}$$
$$\left\{\left(-\frac{r_{rec}}{2t_{rec}}g_{USB}^2 r_{USB}^{CAV} r_{USB}^{CAV}\sin^2\alpha_{USB}e^{-2i\psi}+\frac{1}{2}g_{USB}r_{USB}^{CAV}\sin\alpha_{USB}e^{-i\psi}\right)e^{i\gamma}\right.$$
$$\left.\left.-\left(\frac{r_{rec}}{2t_{rec}}g_{LSB}^2 r_{LSB}^{CAV} r_{LSB}^{CAV}\sin^2\alpha_{LSB}e^{2i\psi}-\frac{1}{2}g_{LSB}r_{LSB}^{CAV}\sin\alpha_{LSB}e^{i\psi}\right)e^{-i\gamma}\right\}^*\right\}$$
$$\rightarrow 0 \tag{2.128}$$

$$\left.\frac{\partial v_Q^{asy}}{\partial \phi_{DIF}}\right|_{\aleph} = -\Re\left\{\left(\frac{ir_{rec}}{2t_{rec}} g_{CR}^2 r_{CR}^{CAV} r_{CR}^{CAV} \sin^2 \mathcal{E}_{CR} - \frac{i}{2} g_{CR} r_{CR}^{CAV} \cos \mathcal{E}_{CR}\right)\right.$$
$$\left(i g_{USB} r_{USB}^{CAV} \sin \alpha_{USB} e^{-i\psi} e^{i\gamma} + i g_{LSB} r_{LSB}^{CAV} \sin \alpha_{LSB} e^{i\psi} e^{-i\gamma}\right)^*$$
$$-g_{CR} r_{CR}^{CAV} \sin \mathcal{E}_{CR}$$
$$\left\{\left(\frac{ir_{rec}}{2t_{rec}} g_{USB}^2 r_{USB}^{CAV} r_{USB}^{CAV} \sin^2 \alpha_{USB} e^{-2i\psi} + \frac{i}{2} g_{USB} r_{USB}^{CAV} \cos \alpha_{USB} e^{-i\psi}\right) e^{i\gamma}\right.$$
$$\left.\left. - \left(\frac{ir_{rec}}{2t_{rec}} g_{LSB}^2 r_{LSB}^{CAV} r_{LSB}^{CAV} \sin^2 \alpha_{LSB} e^{2i\psi} + \frac{i}{2} g_{LSB} r_{LSB}^{CAV} \cos \alpha_{LSB} e^{i\psi}\right) e^{-i\gamma}\right\}^*\right\}$$
$$\rightarrow g_{CR} g_{SB} r_{CR}^{CAV} r_{SB}^{CAV} \sin \alpha_{SB} \tag{2.129}$$

$$\left.\frac{\partial v_I^{rep}}{\partial \Phi_{COM}}\right|_{\aleph} = \Im\left\{-\frac{1}{2t_{rec}} g_{CR}^2 r_{CR}^{\prime CAV} \cos \mathcal{E}_{CR}\right.$$
$$\left(g_{USB} r_{USB}^{CAV} \cos \alpha_{USB} e^{-i\psi} e^{i\gamma} + g_{LSB} r_{LSB}^{CAV} \cos \alpha_{LSB} e^{i\psi} e^{-i\gamma}\right)^*$$
$$-\frac{1}{2t_{rec}} g_{CR} r_{USB}^{CAV} \cos \mathcal{E}_{CR}$$
$$\left.\left(g_{USB}^2 r_{USB}^{\prime CAV} \cos \alpha_{USB} e^{-i\psi} e^{i\gamma} + g_{LSB}^2 r_{LSB}^{\prime CAV} \cos \alpha_{LSB} e^{i\psi} e^{-i\gamma}\right)^*\right\}$$
$$\rightarrow \frac{1}{t_{rec}} g_{CR} g_{SB} \left(g_{CR} |r_{CR}^{\prime CAV}| r_{SB}^{CAV} + g_{SB} r_{CR}^{CAV} |r_{SB}^{\prime CAV}|\right) \cos \alpha_{SB} \tag{2.130}$$

$$\left.\frac{\partial v_I^{rep}}{\partial \Phi_{DIF}}\right|_{\aleph} = \Im\left\{-\frac{1}{2t_{rec}} g_{CR}^2 r_{CR}^{CAV} \sin \mathcal{E}_{CR}\right.$$
$$\left(g_{USB} r_{USB}^{CAV} \cos \alpha_{USB} e^{-i\psi} e^{i\gamma} + g_{LSB} r_{LSB}^{CAV} \cos \alpha_{LSB} e^{i\psi} e^{-i\gamma}\right)^*$$
$$-\frac{1}{2t_{rec}} g_{CR} r_{USB}^{CAV} \cos \mathcal{E}_{CR}$$
$$\left.\left(-i g_{USB}^2 r_{USB}^{\prime CAV} \sin \alpha_{USB} e^{-i\psi} e^{i\gamma} + i g_{LSB}^2 r_{LSB}^{\prime CAV} \sin \alpha_{LSB} e^{i\psi} e^{-i\gamma}\right)^*\right\}$$
$$\rightarrow 0 \tag{2.131}$$

$$\left.\frac{\partial v_I^{rep}}{\partial \phi_{COM}}\right|_{\aleph} = \Im\left\{\frac{i}{2t_{rec}} g_{CR}^2 r_{CR}^{CAV} \cos \mathcal{E}_{CR}\right.$$
$$\left(g_{USB} r_{USB}^{CAV} \cos \alpha_{USB} e^{-i\psi} e^{i\gamma} + g_{LSB} r_{LSB}^{CAV} \cos \alpha_{LSB} e^{i\psi} e^{-i\gamma}\right)^*$$
$$+\frac{1}{2t_{rec}} g_{CR} r_{USB}^{CAV} \cos \mathcal{E}_{CR}$$
$$\left.\left(i g_{USB}^2 r_{USB}^{CAV} \cos \alpha_{USB} e^{-i\psi} e^{i\gamma} + i g_{LSB}^2 r_{LSB}^{\prime CAV} \cos \alpha_{LSB} e^{i\psi} e^{-i\gamma}\right)^*\right\}$$
$$\rightarrow \frac{1}{t_{rec}} g_{CR} g_{SB} (g_{CR} - g_{SB}) r_{CR}^{CAV} r_{SB}^{CAV} \cos \alpha_{SB} \tag{2.132}$$

$$\begin{aligned}\left.\frac{\partial v_I^{rep}}{\partial \phi_{DIF}}\right|_{\aleph} &= \Im\Big\{-\frac{i}{2t_{rec}}g_{CR}^2 r_{CR}^{CAV}\sin\mathcal{E}_{CR} \\ &\quad \left(g_{USB}r_{USB}^{CAV}\cos\alpha_{USB}e^{-i\psi}e^{i\gamma}+g_{LSB}r_{LSB}^{CAV}\cos\alpha_{LSB}e^{i\psi}e^{-i\gamma}\right)^* \\ &\quad -\frac{1}{2t_{rec}}g_{CR}r_{USB}^{CAV}\cos\mathcal{E}_{CR} \\ &\quad \left(-g_{USB}^2 r_{USB}^{CAV}\sin\alpha_{USB}e^{-i\psi}e^{i\gamma}+g_{LSB}^2 r_{LSB}^{CAV}\sin\alpha_{LSB}e^{i\psi}e^{-i\gamma}\right)^*\Big\} \\ &\to 0\end{aligned} \tag{2.133}$$

Then the signal matrix for symmetric interferometer; $\Psi = \psi = 0$ become numerically

$$\begin{array}{c} \\ v_Q^{ANT} \\ v_Q^{REF} \\ v_I^{PCK} \\ v_I^{REF} \end{array}\begin{array}{c} \begin{array}{cccc} \Phi_{DIF} & \phi_{DIF} & \Phi_{COM} & \phi_{COM} \end{array} \\ \begin{pmatrix} -1.96\times10^3 & -5.09\times10^0 & 0 & 0 \\ 3.56\times10^{-3} & 1.18\times10^0 & 0 & 0 \\ 0 & 0 & -2.41\times10^5 & 4.40\times10^1 \\ 0 & 0 & -2.76\times10^3 & -1.37\times10^0 \end{pmatrix} \end{array} \tag{2.134}$$

$$= \begin{pmatrix} 1 & 3.01\times10^{-3} & 0 & 0 \\ 3.02\times10^{-3} & 1 & 0 & 0 \\ 0 & 0 & 1 & -1.83\times10^{-4} \\ 0 & 0 & 1 & 4.96\times10^{-2} \end{pmatrix}.$$

As can be seen, differential degrees of freedom are well diagonalized, while common mode degrees do not. In this calculations, demodulation phases are complete in-phase and quadrature-phase, in other words, γ was set to be 0. With these conditions, off-diagonal sells of this matrix are exactly 0 on calculations. So, it is difficult to extract the signal for ϕ_{COM} as is reported. [14]

Suppose there are some asymmetry which is denoted by Ψ, this matrix will change a little bit because the sidebands inside recycling cavity rotate a little compared with symmetric case. By choosing appropriate demodulation phase γ, matrix can become

$$\begin{array}{c} \\ v_Q^{ANT} \\ v_Q^{REF} \\ v_I^{PCK} \\ v_I^{REF} \end{array}\begin{array}{c} \begin{array}{cccc} \Phi_{DIF} & \phi_{DIF} & \Phi_{COM} & \phi_{COM} \end{array} \\ \begin{pmatrix} -1.68\times10^3 & -5.07\times10^0 & 0 & 0 \\ 3.13\times10^{-3} & 7.80\times10^{-1} & 1.72\times10^3 & 1.50\times10^{-3} \\ 2.99\times10^{-1} & 7.44\times10^1 & 2.08\times10^5 & -1.35\times10^{-3} \\ -4.61\times10^{-3} & -1.14\times10^0 & -8.68\times10^{-2} & 1.42\times10^0 \end{pmatrix} \end{array} \tag{2.135}$$

$$= \begin{pmatrix} 1 & 3.02 \times 10^{-3} & 0 & 0 \\ 4.01 \times 10^{-3} & 1 & 2.20 \times 10^{3} & 1.92 \times 10^{-3} \\ 1.44 \times 10^{-6} & 3.58 \times 10^{-4} & 1 & 6.49 \times 10^{-9} \\ -3.25 \times 10^{-3} & -8.0 \times 10^{-1} & 6.11 \times 10^{-2} & 1 \end{pmatrix}$$

The importance of these results is that the demodulation phases can diagonalize the signal matrix with presence of some asymmetry, which is often the case for interferometer unless the recycling cavity length are adjusted with accuracy of sub-millimeter. In return, off diagonal sells have non-zero elements. Further more, when finite defects in interference at the beam splitter is taken into account, some part of carrier will leak out to differential port. This carries signals for common degrees o freedom, and thus this degrade the diagonalizing matrix.

Another way of diagonalizing is to make use of optical matching.[14] Basically, the signal $\partial v_I^{REF}/\partial\Phi_{COM}$ is dominated by the first term of Eqn.2.118, and this will vanish by make $r_{SB}^{PRFPMI} = 0$. This can be realized by making reflectivity of recycling mirror equal to that of FPMI, then both side bands does not return toward reflection port. This technique is excellent but required accuracy of reflectivity of recycling mirror is 10ppm.

On the other hand, signals for independent control scheme becomes

$$\begin{array}{c} \\ v_I^{IN} \\ v_I^{OF} \end{array} \begin{array}{c} \begin{array}{cccc} \Phi_{IN} & \Phi_{OF} & \phi_{DIF} & \phi_{COM} \end{array} \\ \begin{pmatrix} 1.27 \times 10^5 & 1.17 \times 10^5 & - & - \\ 1.15 \times 10^5 & 1.25 \times 10^5 & - & - \end{pmatrix} \end{array} \tag{2.136}$$

$$= \begin{pmatrix} 1 & 9.21 \times 10^{-1} & - & - \\ 9.20 \times 10^{-1} & 1 & - & - \end{pmatrix} \tag{2.137}$$

In contrast with independent control for FPMI, the error signals for both arm cavities are almost completely mixed and cannot be separated by demodulation phase any more.

To summarize, two signals for arm cavities, Φ_{DIF} and Φ_{COM} can be extracted easily from pick off port and differential port stably. This is owing to its large size of signals which comes from finesse of arm cavities and they are tolerant to imperfections of optics and electronics; asymmetry of side bands phase or demodulation phase error. The difficulties are signals for recycling cavity, ϕ_{DIF} and ϕ_{COM}. They are intrinsically small, so they should be carefully extracted from reflected light from PRFPMI. Even for the symmetric case, $\Psi = \psi = 0$, required accuracy of demodulation phase is 100 μrad in order to maintain the priority of specific signals. From these point of view, it is difficult to expect completely diagonalized

signal matrix for interferometer in use and feed back system should compensate these difficulties.

2.6 Signal Extraction for Alignment Control

2.6.1 Detection of Field

Suppose the field contains spatial fundamental and first higher order modes for both carrier and side bands at some detection point as follows,

$$\begin{aligned} E = &(E_{CR00} + E_{CR10}) \\ &+(E_{USB00} + E_{USB10})e^{i\Omega t} + (E_{LSB00} + E_{LSB10})e^{-i\Omega t} \end{aligned} \tag{2.138}$$

This field can be detected by photo diode and converted to photo current as,

$$\begin{aligned} i_{PD} &= |(E_{CR00} + E_{CR10}) \\ &\quad +(E_{USB00} + E_{USB10})e^{i\Omega t} + (E_{LSB00} + E_{LSB10})e^{-i\Omega t}|^2 && (2.139) \\ &= I_{DC} + (I_\Omega e^{i\Omega t} + C.C.) + (I_{2\Omega} e^{2i\Omega t} + C.C.) && (2.140) \\ I_\Omega &= (E_{CR00} + E_{CR10})(E^*_{LSB00} + E^*_{LSB10}) + (E_{USB00} + E_{USB10})(E^*_{CR00} + E^*_{CR10}) \\ I_{2\Omega} &= (E_{USB00} + E_{USB10})(E^*_{LSB00} + E^*_{LSB10}) \end{aligned}$$

here, efficiency of photo detector was set to be unity as same for the length sensing. This photo current are demodulated and only I_Ω term is down converted to DC signal as,

$$\begin{aligned} i_{demo} &= \Re\{(E_{CR00} + E_{CR10})(E^*_{LSB00} + E^*_{LSB10})e^{-i\gamma} && (2.141) \\ &\quad +(E_{USB00} + E_{USB10})(E^*_{CR00} + E^*_{CR10})e^{i\gamma}\} \\ &\rightarrow \Re\{E_{CR00}(E_{USB10}e^{-i\gamma} + E_{LSB10}e^{i\gamma})^* && (2.142) \\ &\quad +E_{CR10}(E_{USB00}e^{-i\gamma} + E_{LSB00}e^{i\gamma})^*\} \\ &= \Im\{H_{CR00}(H_{USB10}e^{-i\gamma} + H_{LSB10}e^{i\gamma})^* && (2.143) \\ &\quad +H_{CR10}(H_{USB00}e^{-i\gamma} + H_{LSB00}e^{i\gamma})^*\}E^{inc}_{CR}E^{inc}_{SB}\int U_{00}U^*_{10}dS \end{aligned}$$

where,

$$E_{x00} = \int U_{00}dSH_{x00}E^{inc}_x, \quad E_{x10} = \int U_{10}dSH_{x10}E^{inc}_x \tag{2.144}$$

and

$$E_{CR}^{inc} = J_0 E^{inc}, \quad E_{SB}^{inc} = iJ_1 E^{inc} \tag{2.145}$$

$$\int U_{00}U_{10}^{*}dS = \int U_{00}^{*}U_{10}dS = \left(\frac{2}{w(z)}\right)^{1/2} \tag{2.146}$$

Note that Product of TEM_{00} and TEM_{00} will vanish because the two signals detected by two halves of segmented photo diode are subtracted each other. As a result, cross term of TEM_{00} and TEM_{10} will survive in the signals and normalized signal can be defined as,

$$\begin{aligned} v_{demo}|_N \equiv \Im\{&H_{CR00}(H_{USB10}e^{-i\gamma} + H_{LSB10}e^{i\gamma})^* \\ &+H_{CR10}(H_{USB00}e^{-i\gamma} + H_{LSB00}e^{i\gamma})^*\} \end{aligned} \tag{2.147}$$

2.6.2 Signal Extraction

Cavity Control

For the calculation of signals for alignment sensing, the essential feature of the procedure is that the transition probability between TEM_{00} mode and higher order transverse mode has a non-zero components. As there are two degrees of freedom for each mirror misalignment, that is, pitch and yaw motion, mirror misalignment matrix should be represented with 3 by 3 matrix, whose components give transition probabilities between TEM_{00}, TEM_{10} and TEM_{01} modes.[17] However, these two degrees of freedom are intrinsically independent and will not have cross term in the further calculations, so the matrix can be reduced to 2 by 2 matrix for tractability. So, if misalignment effects are sufficiently small to be expanded with up to the first higher order mode, the 2 by2 transition matrix can be defined and incident beam modes are scattered as follows.

$$\boldsymbol{E}_{scattered} = \boldsymbol{M}_{2\times 2}\boldsymbol{E}_{incident} \tag{2.148}$$

$$\boldsymbol{E}_{incident} = \begin{pmatrix} U_{00} \\ U_{10} \end{pmatrix} \tag{2.149}$$

For example, propagator operator can be expressed as

$$\boldsymbol{T}_{translate} = \begin{pmatrix} e^{i\eta} & 0 \\ 0 & e^{2i\eta} \end{pmatrix} e^{-i\Phi} \tag{2.150}$$

where, Φ denotes the phase evolution of plain wave and η is a Guoy phase shift due to propagation. The important characteristic is that Guoy phase shift depends on the spatial

mode of the beam and this is the very reason for signal separation. And mirror misalignment matrix become

$$\boldsymbol{M}_{tilt} = \begin{pmatrix} 1 & -2i\Theta_x \\ -2i\Theta_x & 1 \end{pmatrix} \tag{2.151}$$

where, Θ_x is normalized angle, which is defined by[17]

$$\Theta_x = \frac{\pi w(z)}{\lambda}\theta_x \tag{2.152}$$

As a simple case, consider a simple Fabry-Perot optical cavity which is compose of flat and concave mirrors. It is convenient to use the same calculation formalism for the length sensing. The misalignment matrices for the mirrors of Fabry-Perot cavity are

$$\boldsymbol{M}_{IM} = \begin{pmatrix} 1 & -2i\Theta_{IM} \\ -2i\Theta_{IM} & 1 \end{pmatrix} \tag{2.153}$$

$$\boldsymbol{M}_{BM} = \begin{pmatrix} 1 & -2i\Theta_{BM} \\ -2i\Theta_{BM} & 1 \end{pmatrix} \tag{2.154}$$

and translation matrix for one pass propagation becomes using round trip phase Φ,

$$\boldsymbol{T}_{ARM} = \begin{pmatrix} e^{i\eta_{ARM}} & 1 \\ 1 & e^{2i\eta_{ARM}} \end{pmatrix} e^{\left(-i\frac{\Phi}{2}\right)} \tag{2.155}$$

where, η_{ARM} corresponds to Guoy phase evolution due to propagation inside a cavity. Resonance condition for carrier is $\Phi_{CR} - 2\eta_{ARM} = \pi$ and $\Phi_{SB} - 2\eta_{ARM} = 0 \pm \Psi$ for both side bends. Using these relation, reflected light from the cavity can be extracted as follows,

$$\boldsymbol{M}^{ref} = r_{IM}\boldsymbol{M}^{*}_{IM} - \{t_{IM}r_{BM}\boldsymbol{T}\boldsymbol{M}_{BM}\boldsymbol{T}t_{IM}\}\{\boldsymbol{I} - r_{IM}r_{BM}\boldsymbol{M}_{IM}\boldsymbol{T}\boldsymbol{M}_{BM}\boldsymbol{T}\}^{-1} \tag{2.156}$$

$$= r_{IM}\boldsymbol{M}^{*}_{IM}\left\{\boldsymbol{I} - \frac{r^2_{IM} + t^2_{BM}}{r^2_{IM}}\boldsymbol{M}^{RT}\right\}\left\{\boldsymbol{I} - \boldsymbol{M}^{RT}\right\}^{-1} \tag{2.157}$$

$$\boldsymbol{M}^{RT}_{CR} = r_{IM}r_{BM}\boldsymbol{M}_{IM}\boldsymbol{T}_{CR}\boldsymbol{M}_{BM}\boldsymbol{T}_{CR} \tag{2.158}$$

$$\simeq r_{IM}r_{BM}\begin{pmatrix} 1 & -2i(\Theta_{BM} + \Theta_{IM}e^{i\eta})e^{i\eta} \\ -2i(\Theta_{IM} + \Theta_{BM}e^{i\eta}) & e^{2i\eta} \end{pmatrix} \tag{2.159}$$

$$\boldsymbol{M}^{RT}_{USB} = r_{IM}r_{BM}\boldsymbol{M}_{IM}\boldsymbol{T}_{USB}\boldsymbol{M}_{BM}\boldsymbol{T}_{USB} \tag{2.160}$$

$$\simeq r_{IM}r_{BM}\begin{pmatrix} 1 & -2i(\Theta_{BM} + \Theta_{IM}e^{i\eta})e^{i\eta} \\ -2i(\Theta_{IM} + \Theta_{BM}e^{i\eta}) & e^{2i\eta} \end{pmatrix} e^{-i\Psi} \tag{2.161}$$

$$\boldsymbol{M}^{RT}_{LSB} = r_{IM}r_{BM}\boldsymbol{M}_{IM}\boldsymbol{T}_{LSB}\boldsymbol{M}_{BM}\boldsymbol{T}_{LSB} \tag{2.162}$$

$$\simeq r_{IM}r_{BM}\begin{pmatrix} 1 & -2i(\Theta_{BM} + \Theta_{IM}e^{i\eta})e^{i\eta} \\ -2i(\Theta_{IM} + \Theta_{BM}e^{i\eta}) & e^{2i\eta} \end{pmatrix} e^{i\Psi} \tag{2.163}$$

Using these matrices, reflection matrix for carrier and both side bands are

$$M_{CR}^{ref} \equiv \begin{pmatrix} H_{CR00}^{ref} & H_{CR00*}^{ref} \\ H_{CR10}^{ref} & H_{CR10*}^{ref} \end{pmatrix} = \begin{pmatrix} -r_{CR00}^{cav} & H_{CR00*}^{ref}(\Theta_{IM}, \Theta_{BM}) \\ H_{CR10}^{ref}(\Theta_{IM}, \Theta_{BM}) & -r_{CR10}^{cav} \end{pmatrix} \quad (2.164)$$

$$M_{USB}^{ref} \equiv \begin{pmatrix} H_{USB00}^{ref} & H_{USB00*}^{ref} \\ H_{USB10}^{ref} & H_{USB10*}^{ref} \end{pmatrix} = \begin{pmatrix} -r_{USB00}^{cav} & H_{USB00*}^{ref}(\Theta_{IM}, \Theta_{BM}) \\ H_{USB10}^{ref}(\Theta_{IM}, \Theta_{BM}) & -r_{USB10}^{cav} \end{pmatrix} \quad (2.165)$$

$$M_{LSB}^{ref} \equiv \begin{pmatrix} H_{LSB00}^{ref} & H_{LSB00*}^{ref} \\ H_{LSB10}^{ref} & H_{LSB10*}^{ref} \end{pmatrix} = \begin{pmatrix} -r_{LSB00}^{cav} & H_{LSB00*}^{ref}(\Theta_{IM}, \Theta_{BM}) \\ H_{LSB10}^{ref}(\Theta_{IM}, \Theta_{BM}) & -r_{LSB10}^{cav} \end{pmatrix} \quad (2.166)$$

These fields are sensed by quadrant wave front sensor and demodulated then down-converted to DC signal according to Eqn.2.147. Though these demodulated expression can be expanded analytically, it is very complicated function of Θ_{IM} and Θ_{BM}. So, the error signals are calculated by computer numerically. As the Guoy phase dependencies of the signals are shown in Fig.2.15, appropriate Guoy phase position can be chosen so that signal matrix will be diagonalized. If the two WFSs are optimally set to the positions

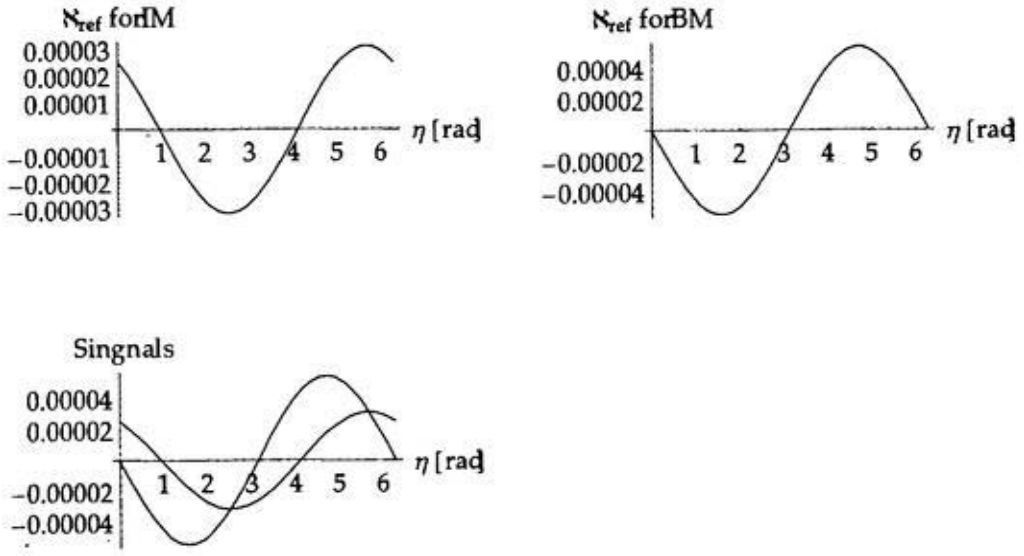

Figure 2.15: Alignment signals for IM and BM with Guoy phase evolution.

whose corresponding Guoy phases are around one and three, for back and input mirror respectively, the signal matrix will be completely diagonalized. The alignment sensing

matrix will become

$$\begin{array}{c} \\ v_I^{REF}(\eta \simeq 1) \\ v_I^{REF}(\eta \simeq 3) \end{array} \begin{array}{c} \begin{array}{cc} \Theta_{IM} & \Theta_{BM} \end{array} \\ \begin{pmatrix} 1.98 \times 10^4 & 0 \\ 0 & 8.60 \times 10^2 \end{pmatrix} \end{array} \tag{2.167}$$

Coupled Cavity Control

This formalism is extensible to more complicated optical system, coupled cavity by similar way for length sensing scheme. Again major modification from FP cavity is its back mirror reflection matrix, which should be replaced with reflection matrix of FP cavity. Each misalignment matrices and translation matrices are

$$\boldsymbol{M}_{IM} = \begin{pmatrix} 1 & -2i\Theta_{IM} \\ -2i\Theta_{IM} & 1 \end{pmatrix} \tag{2.168}$$

$$\boldsymbol{M}_{BM} = \begin{pmatrix} 1 & -2i\Theta_{BM} \\ -2i\Theta_{BM} & 1 \end{pmatrix} \tag{2.169}$$

$$\boldsymbol{M}_{CM} = \begin{pmatrix} 1 & -2i\Theta_{CM} \\ -2i\Theta_{CM} & 1 \end{pmatrix} \tag{2.170}$$

and translation matrix becomes using round trip phase Φ, ϕ for FP cavity and coupling cavity,

$$\boldsymbol{T}_{ARM} = \begin{pmatrix} e^{i\eta_{ARM}} & 0 \\ 0 & e^{2i\eta_{ARM}} \end{pmatrix} e^{-i\Phi/2} \tag{2.171}$$

$$\boldsymbol{T}_{CC} = \begin{pmatrix} e^{i\eta_{CC}} & 0 \\ 0 & e^{2i\eta_{CC}} \end{pmatrix} e^{-i\phi/2} \tag{2.172}$$

Using these matrices, reflection and picked off matrix can be extracted as follows,

$$\boldsymbol{M}^{CC} = r_{CM}\boldsymbol{M}_{CM}^{*} - \left\{t_{CM}^2 r_{BM}\boldsymbol{T}\boldsymbol{M}_{REF}\boldsymbol{T}\right\}\left\{\boldsymbol{I} - r_{CM}\boldsymbol{M}_{CM}\boldsymbol{T}\boldsymbol{M}^{REF}\boldsymbol{T}\right\}^{-1} \tag{2.173}$$

$$= r_{CM}\boldsymbol{M}_{CM}^{*}\left\{\boldsymbol{I} - \frac{r_{CM}^2 + t_{CM}^2}{r_{CM}^2}\boldsymbol{M}^{RT}\right\}\left\{\boldsymbol{I} - \boldsymbol{M}^{RT}\right\}^{-1} \tag{2.174}$$

$$\boldsymbol{M}^{PCK} = t_{CM}\boldsymbol{M}^{RT}\left\{\boldsymbol{I} - \boldsymbol{M}^{RT}\right\}^{-1} \tag{2.175}$$

Resonant conditions are $\Phi_{CR} - 2\eta_{ARM} = \pi$, $\Phi_{USB} - 2\eta_{ARM} = 0 + \Psi$ and $\Phi_{LSB} - 2\eta_{ARM} = 0 - \Psi$ for arm cavity and $\phi_{CR} - 2\eta_{CC} = 0$, $\phi_{USB} - 2\eta_{CC} = \pi + \psi$ and $\phi_{LSB} - 2\eta_{CC} = \pi - \psi$ for

coupling cavity. For symmetric optical designed cavity, $\Psi = 0, \psi = 0$, alignment signals will change with η as Fig.2.16 where, each signals are maximized by adjusting demodulation phase. So, resulting matrix become,

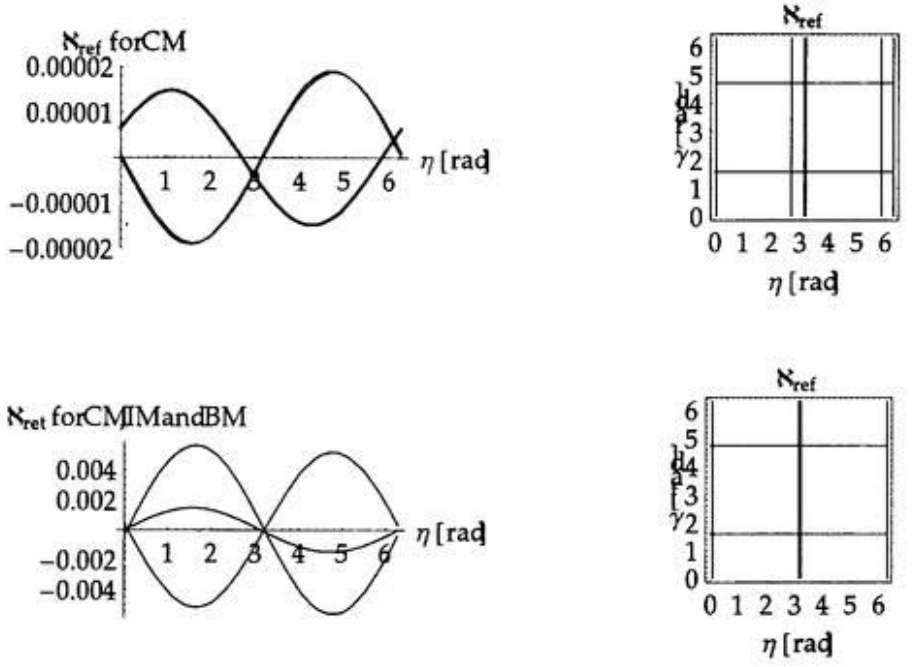

Figure 2.16: Alignment signals for coupled cavity with Guoy phase evolution. Ψ=0

$$\begin{array}{c} \\ v_I^{REF}(\eta = 3.17) \\ v_I^{PCK}(\eta = 2.7) \\ v_I^{REF}(\eta = 3.14) \end{array} \begin{array}{c} \begin{array}{ccc} \Theta_{CM} & \Theta_{IM} & \Theta_{BM} \end{array} \\ \begin{pmatrix} 1.07 \times 10^{-5} & 7.23 \times 10^{-7} & -9.15 \times 10^{-7} \\ 0 & 1.41 \times 10^{-5} & 1.29 \times 10^{-5} \\ -5.17 \times 10^{-3} & 5.17 \times 10^{-3} & 1.46 \times 10^{-3} \end{pmatrix} \end{array} \tag{2.176}$$

This means that information of input mirror and back mirror are mixing and cannot be separated. If $\Psi = \pi/3$ and with appropriate demodulation phase, signals will change according to η as Fig.2.17 and the matrix change to the form of

$$\begin{array}{c} \\ v_I^{REF}(\eta = 3.1) \\ v_I^{REF}(\eta = 3.2) \\ v_I^{REF}(\eta = 1.2) \end{array} \begin{array}{c} \begin{array}{ccc} \Theta_{CM} & \Theta_{IM} & \Theta_{BM} \end{array} \\ \begin{pmatrix} 1.04 \times 10^{-5} & 0 & 0 \\ 0 & 1.86 \times 10^{-6} & 0 \\ 0 & 0 & -7.69 \times 10^{-7} \end{pmatrix} \end{array} \tag{2.177}$$

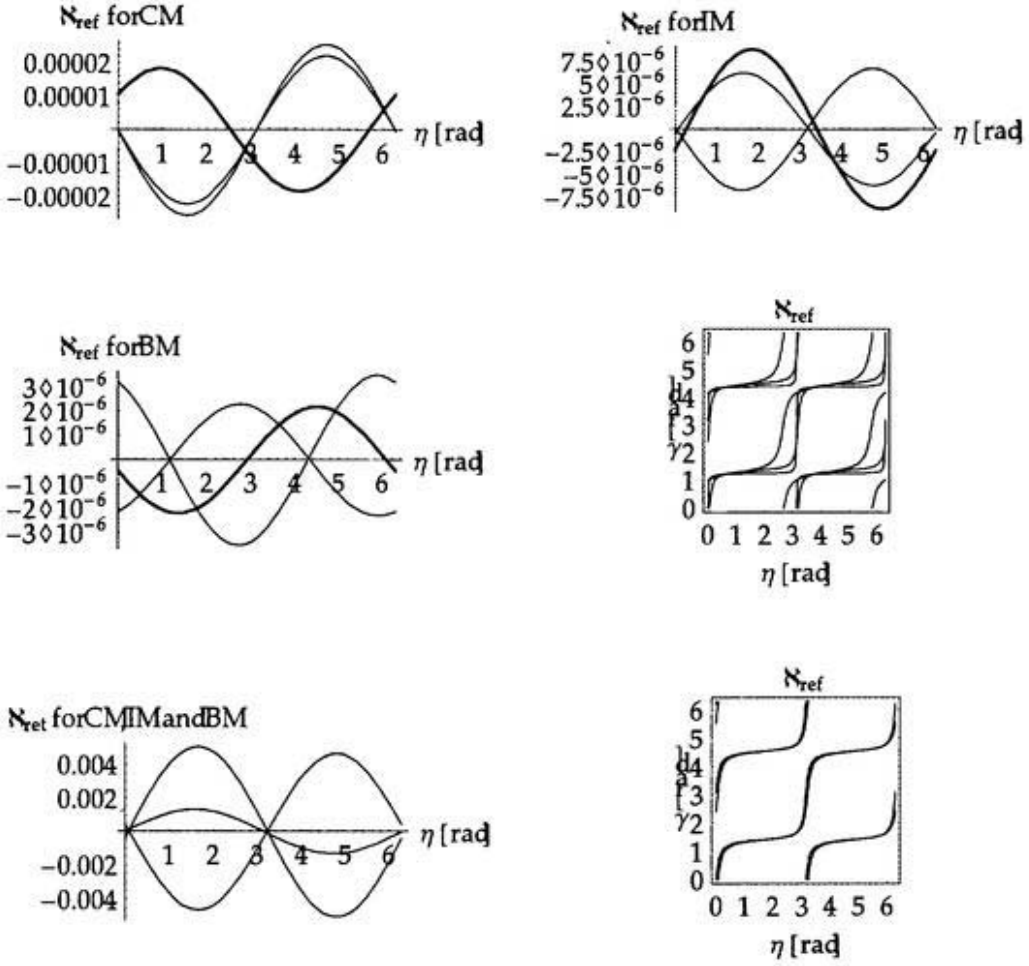

Figure 2.17: Alignment signals for coupled cavity with Guoy phase evolution. $\Psi = \pi/3$

By selecting the guoy phase and demodulation phase properly, the matrix can be almost diagonalized.

Interferometer Control

In order to expand this formulation to recycled interferometer, three additional formalities, namely asymmetry, optical recombine and recycling cavity, should be gone through. These procedures are completely analogous to that of length sensing scheme except that the coefficient is matrix for the alignment sensing scheme. From the consideration of previous section, the reflection coefficient matrix of the cavity with misaligned mirrors are summarized with matrix form, $\boldsymbol{M}^{ref}$. The effect of asymmetry can be translated to the displacement of the cavity axis along to the beam propagating axis, z-axis. (See Fig.2.18) As long as the displacement is small compared to the Rayleigh range, the main effect will

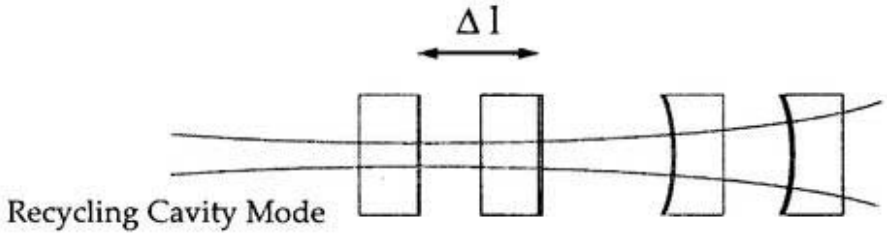

Figure 2.18: Displacement of the FP cavity due to the asymmetry of the interferometer.

appear only on the Guoy phase evolution due to beam propagation of displacement. So, this effect can be attributed to additional translation on recycling cavity. The translation matrices for carrier and sidebands are written as follows,

$$\boldsymbol{T}_{CR}^{IN} = \begin{pmatrix} e^{i(\eta_{RC}+\eta_{\Delta})} & 0 \\ 0 & e^{2i(\eta_{RC}+\eta_{\Delta})} \end{pmatrix} e^{-i\phi^{IN}/2} \tag{2.178}$$

$$\boldsymbol{T}_{CR}^{OF} = \begin{pmatrix} e^{i(\eta_{RC}-\eta_{\Delta})} & 0 \\ 0 & e^{2i(\eta_{RC}-\eta_{\Delta})} \end{pmatrix} e^{-i\phi^{OF}/2} \tag{2.179}$$

where, η_{RC} is Guoy phase for mean length of recycling cavity; $(l_{IN}+l_{OF})/2$ and η_{Δ} is that for half of the asymmetry; $(l_{IN}-l_{OF})/2$.

Each coefficient matrix can be defined as,

$$\boldsymbol{M}^{INS} = t_{RM}\left\{\boldsymbol{I}-\boldsymbol{M}^{RT}\right\}^{-1} \tag{2.180}$$

$$\boldsymbol{M}^{RT} = -r_{RM}\boldsymbol{M}_{RM}\boldsymbol{M}_{COM} \tag{2.181}$$

$$\boldsymbol{M}^{ref} = r_{RM}\boldsymbol{M}^{\star}_{RM}\left\{\boldsymbol{I}-\frac{r^2_{RM}+t^2_{RM}}{r^2_{RM}}\boldsymbol{M}^{RT}\right\}\left\{\boldsymbol{I}-\boldsymbol{M}^{RT}\right\}^{-1} \tag{2.182}$$

$$\boldsymbol{M}^{ant} = t_{RM}\boldsymbol{M}^{DIFF}\left\{\boldsymbol{I}-\boldsymbol{M}^{RT}\right\}^{-1} \tag{2.183}$$

$$\boldsymbol{M}^{ret} = t_{RM}\boldsymbol{M}^{RT}\left\{\boldsymbol{I}-\boldsymbol{M}^{RT}\right\}^{-1} \tag{2.184}$$

$$\boldsymbol{M}^{COM} = \frac{1}{2}(\boldsymbol{T}^{OF}\boldsymbol{M}^{OF}\boldsymbol{T}^{OF}+\boldsymbol{T}^{IN}\boldsymbol{M}^{IN}\boldsymbol{T}^{IN}) \tag{2.185}$$

$$\boldsymbol{M}^{DIF} = \frac{1}{2}(\boldsymbol{T}^{OF}\boldsymbol{M}^{OF}\boldsymbol{T}^{OF}-\boldsymbol{T}^{IN}\boldsymbol{M}^{IN}\boldsymbol{T}^{IN}) \tag{2.186}$$

Resulting matrix components are very complicated function of misaligned angle and optical parameters of interferometer. So, following matrices are numerically calculated. For symmetric interferometer, $\Psi=\psi=0$, matrix will become

$$\begin{array}{c} \\ v_I^{REF} \\ v_I^{ANT} \\ v_I^{PCK} \\ v_I^{REF} \\ v_I^{ANT} \end{array}\begin{array}{c} \begin{array}{ccccc} \Theta_{IMDIF} & \Theta_{BMDIF} & \Theta_{IMCOM} & \Theta_{BMCOM} & \Theta_{RM} \end{array} \\ \begin{pmatrix} -6.15\times10^{1} & 5.58\times10^{-1} & -9.47\times10^{-2} & 8.60\times10^{-4} & 3.44\times10^{-1} \\ 5.79\times10^{1} & 1.74\times10^{2} & -1.95\times10^{0} & -5.87\times10^{0} & 2.13\times10^{0} \\ 2.72\times10^{0} & 1.24\times10^{1} & -4.5\times10^{2} & -1.86\times10^{3} & -1.46\times10^{1} \\ 1.4\times10^{0} & 4.95\times10^{0} & 8.50\times10^{2} & 3.66\times10^{3} & -1.43\times10^{3} \\ -5.54\times10^{-1} & 3.84\times10^{-1} & 1.19\times10^{-1} & 2.88\times10^{-1} & 1.97\times10^{0} \end{pmatrix} \end{array}$$

$$= \begin{pmatrix} 1 & -9.07\times10^{-3} & 1.54\times10^{-3} & -1.39\times10^{-5} & -5.59\times10^{-3} \\ 3.32\times10^{-1} & 1 & -1.12\times10^{-2} & -3.37\times10^{-2} & 1.12\times10^{-2} \\ -6.04\times10^{-3} & -2.75\times10^{-2} & 1 & 4.12\times10^{-0} & 3.20\times10^{-2} \\ 3.82\times10^{-4} & 1.35\times10^{-3} & 2.30\times10^{-1} & 1 & -3.90\times10^{-1} \\ -2.81\times10^{-1} & 1.95\times10^{-1} & 6.04\times10^{-2} & 1.46\times10^{-1} & 1 \end{pmatrix}$$

As can be seen, differential modes and are wall separated, while common modes for input and back mirrors are are significantly mixing. This comes from that the signals of common mode motion for both mirrors behave almost same in each detection port. There are little guoy phase or demodulation phase dependencies between two signals.

For $\Psi=\pi/3$, $\psi=0$ case, matrix will slightly change but general situation does not improve. In order to control full degree of freedom with analogue feed back system, this should be resolved.

Chapter 3

Power Recycling Experiments

3.1 20m Prototype Interferometer

3.1.1 Optical Layout

The prototype interferometer with the base line length of 20m have been developed at Mitaka campus of National Astronomical Observatory of Japan to test various optical configurations which are designed for full-scale gravitational wave detector, Fig.3.1. Originally, this interferometer was started to construct as one of prototypes to test Fabry-Perot Michelson Interferometer in contrast with Delay Line Interferometer at 1991 as a part of "Gravitational Wave Astronomy" project in Japan. Then this interferometer could demonstrate the operation of optically recombined FP Michelson interferometer with dark fringe locking by using Shnupp (pre-modulation) method for the first time as a standard prototype.[18] Also this interferometer is equipped with independently suspended mirror Mode Cleaner which was thought to be a essential for full scale interferometer and proved to be useful. This Mode Cleaner have been developed to the active transmission system of the phase modulation side bands, which will be described shortly in later section,[19] and this is the unique prototype interferometer in the world which is operated with suspended Mode Cleaner with side bands transmission. As is described historically here, 20m prototype have been introduced and demonstrated many advanced technologies, which are needed for full configured detector, in the forefront of the world. The final frontier, the recycling, as a advanced optical design of interferometer was a next subject of this prototype to investigate.

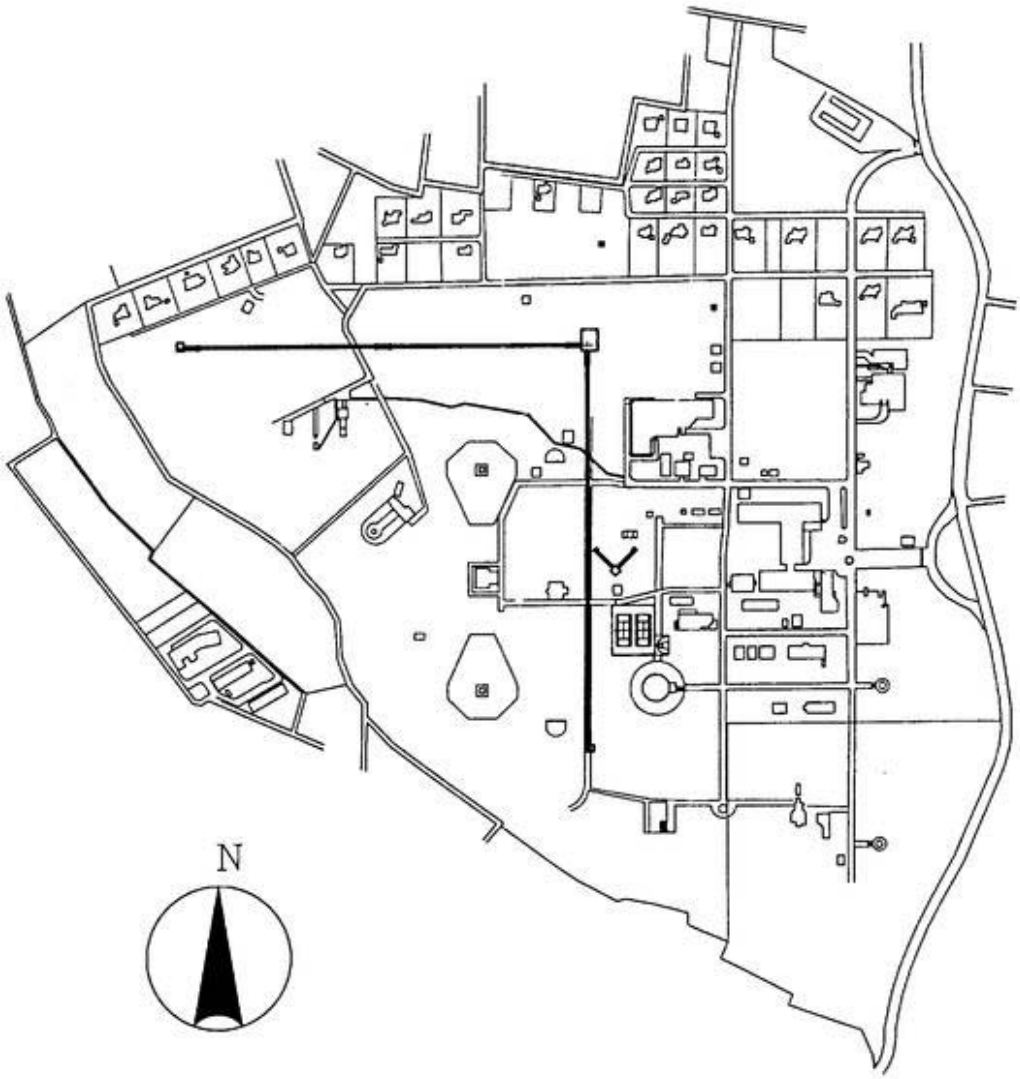

Figure 3.1: 20m prototype interferometer at Mitaka campus of National Astronomical Observatory of Japan. The big L-shape is TAMA300 and small L is the 20m prototype.

The schematic diagram of the interferometer is shown in Fig.3.2. The 20m interferometer

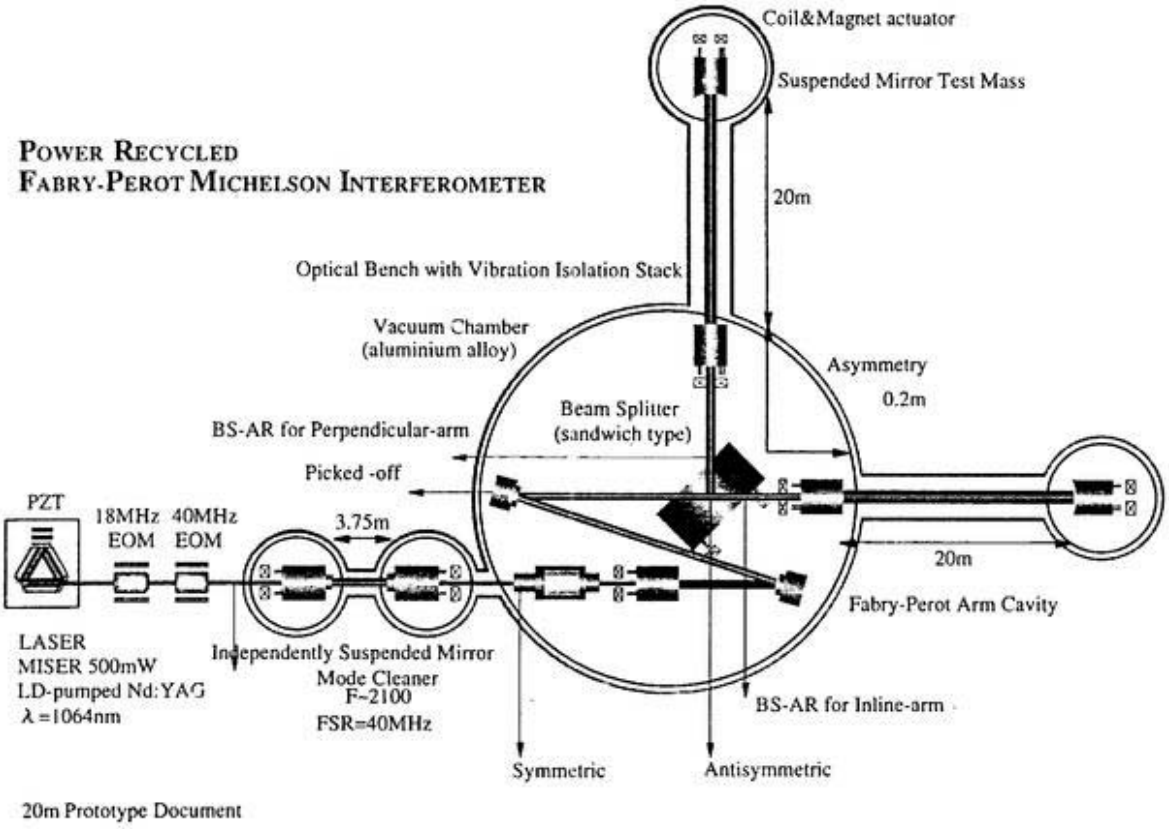

Figure 3.2: Schematic over view of optical layout of 20m prototype.

consists of large three optical parts: light source, Mode Cleaner (MC) and main interferometer. Laser light from the Nd:YAG laser is incident to the input mirror of the MC through the input optics chain, and then resonate inside the MC cavity to pass through toward the main interferometer. It will be stated later about light source and Mode Cleaner. The output beam from MC experiences two suspended steering mirrors before illuminating the beam splitter due to optical axis offset between MC cavity and inline arm cavity, which serve as beam pointing devices to arm cavity. As the recycling cavity requires length of

1875mm for 40MHz RF sidebands which is used for interferometer control, the cavity is folded due to limitation of center chamber space as is drawn in Fig.3.3. Moreover one of

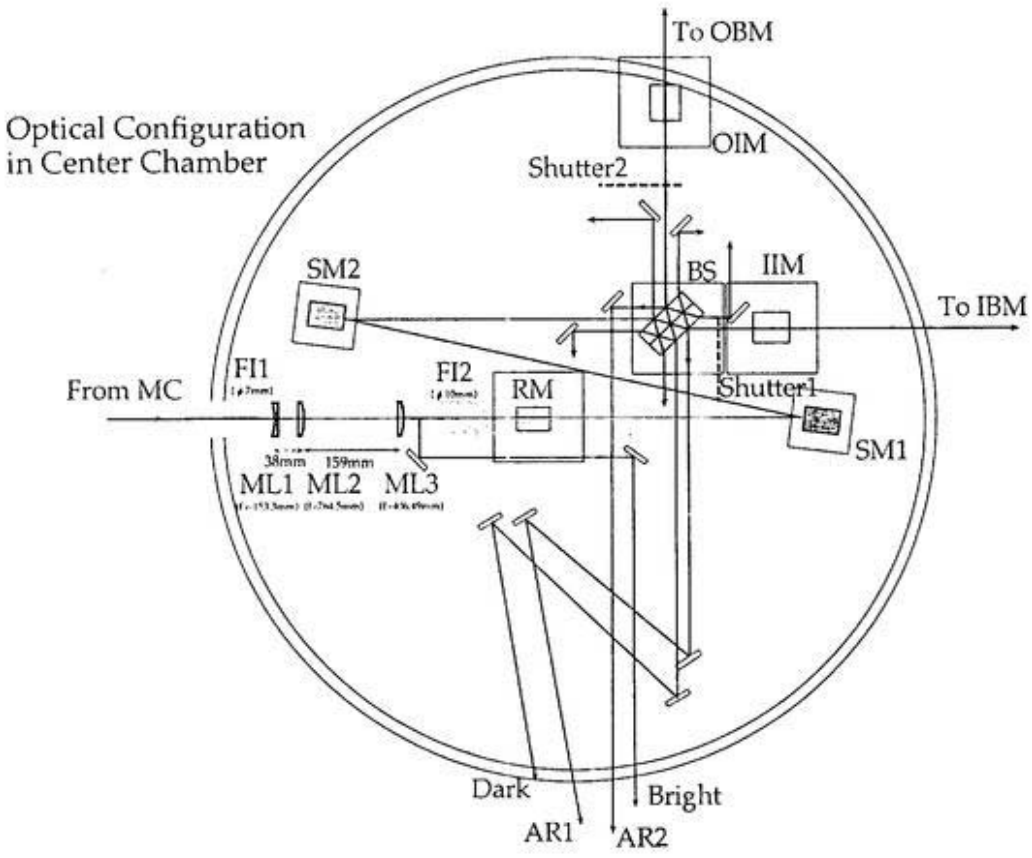

Figure 3.3: Configuration of optics inside the center chamber.

these steering mirrors is used as a pick off mirror in a recycling cavity by using a partially transmitted mirror. The optically recombined Fabry-Perot Michelson Interferometer (FP-MI) consists of 20m long two arm cavities, beam splitter and one more additional mirror, recycling mirror for power recycling between MC and beam splitter. The asymmetry for frontal modulation scheme, which is defined as the difference of distances between BS to coating surface of the input mirror for in-line and off-line arm cavities is 195mm.

3.1.2 Core1: Optics

Arm Cavity Mirrors

The substrates for all mirrors are basically monolithic fused silica, Sprasil P10, supplied by Shin-etsu quartz Co,Ltd. whose dimensions are 50mm in diameter and 60mm in thickness, Fig.3.4. In order to avoid the interference between main beam from reflecting surface

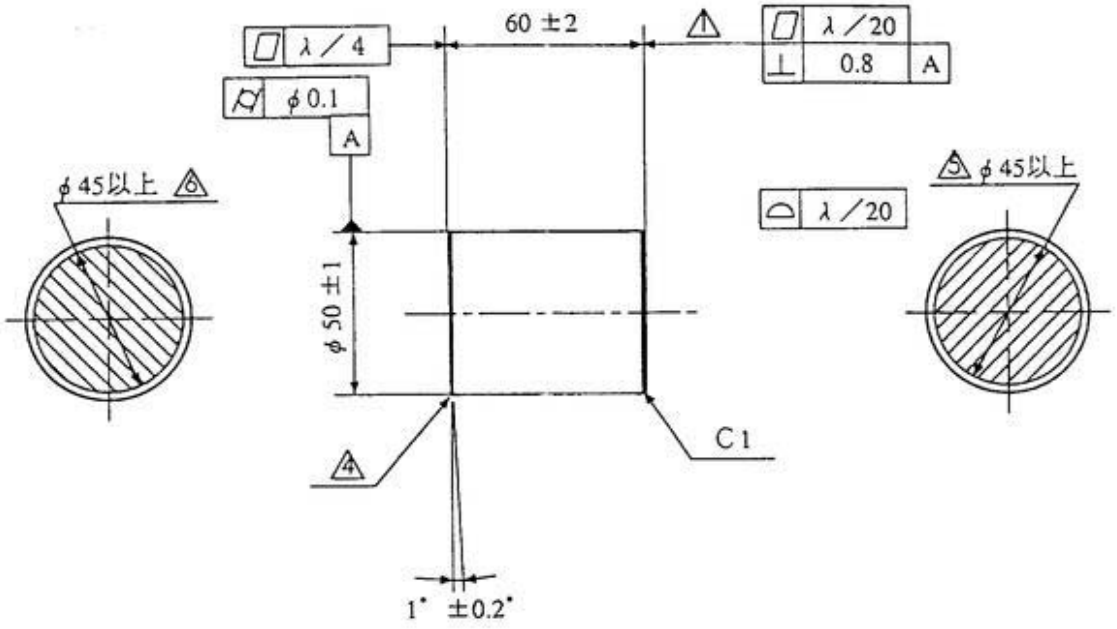

Figure 3.4: Design of monolithic mirror substrates for arm and recycling mirrors.

and that from the back surface, back side of input mirror substrates have a wedge of 1 degree. These substrates were polished and dielectric coated by Japan Aviation Electronics Industry Co,Ltd (JAE). Both surfaces of them were superpolished and the side was also polished to prevent the adsorption of a fine grain of silica and contamination by it. Reflecting surfaces for input mirrors are flat and radii of curvature for back mirrors are 30000mm, while the recycling mirror was polished with radius of curvature of 10800mm. This radius of curvature was determined by recycling cavity length of $\lambda_{mod}/4$=1875mm from mean position of two input mirrors. After polishing process, flatness, figure error and micro roughness of mirror surfaces were measured by JAE using IR interferometer (ZYGO GPI-XP HR) at λ=633nm and a stylus profiler (Talystep). All of the polishing results are

	Figure Error	Microroughness
Input Mirror 1	$\lambda/33$	$\sim$1Årms
Input Mirror 2	$\lambda/30$	$\sim$1Årms
Back Mirror 1	$\lambda/20$	$\sim$1Årms
Back Mirror 2	$\lambda/20$	$\sim$1Årms

Table 3.1: Results of polishing for mirrors.

summarized in Table.3.1

The high reflecting (HR) and the anti-reflecting (AR) surface on the other side were coated with dielectric multi-layer of SiO_2 and Ta_2O_5. All of the mirrors and test pieces which are used in the 20m prototype are manufactured by using Ion Beam Sputtering (IBS) machine, which is thought to be a most promising method to realize a high quality large size mirrors. High reflecting coating are realized by making use of the multi interference from each multi layered coatings. In order to enhance every fields from each layers, coating materials are piled up to the thickness of a quarter of wave length. And total reflectivity of the coating depends on the numbers of these layers, as is shown in Fig.3.5 For example, 29 layers of coatings corresponds to intensity reflectivity of about 0.9999. Original design of coating for back mirrors were 29 layers for $r^2_{BM} = 0.9999$ and for input mirrors were 15 layers for $r^2_{IM} = 0.9880$. These are same design for arm cavity of TAMA300 interferometer.

Beam Splitter

The beam splitter (BS) was made by optically contacting two fused silica plates, whose diameter is 100mm and 25mm in thickness, as is shown in Fig.3.6. The beam splitting coating was piled on contacting surface, which splits s-polarized light half to half in power. Other side of both substrates were coated with quasi AR coatings. So, the incident beam will be split at the center of the BS. Each quasi AR coating were intentionally designed to have 0.7% of reflectivity, so that reflected light from each arm cavity through AR reflection can be used for independent arm control.

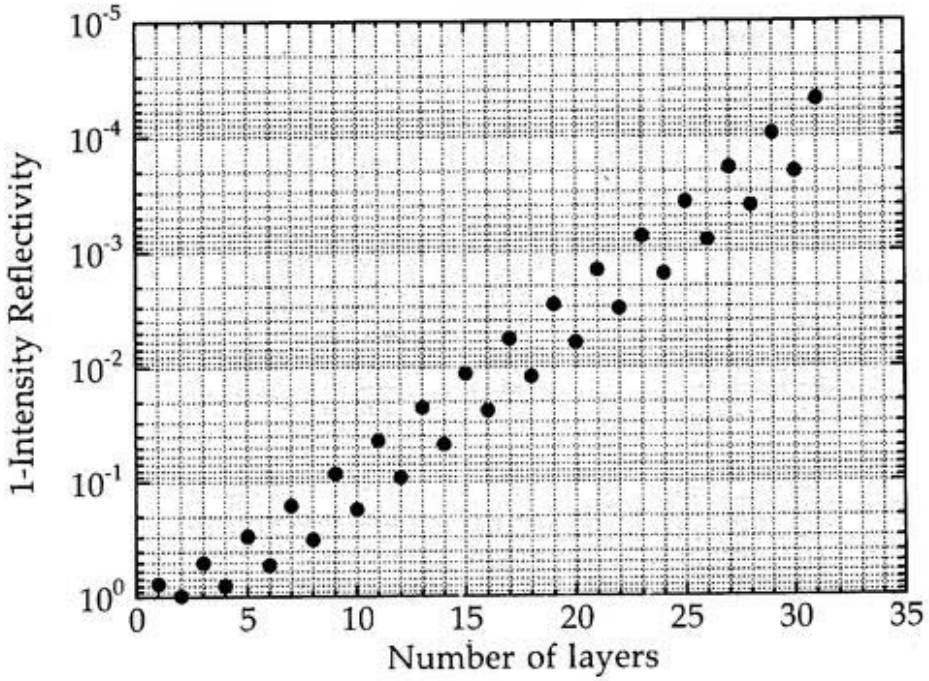

Figure 3.5: Number of layers and its designed reflectivity.

Pick Off Mirror and Steering Mirror

As is described in previous section, two steering mirrors are used in center chamber and one of them is also serving as a pick off mirror. The only difference between them is a design of coating and other features are almost same. Mirror substrates were super polished flat fused silica, which were supplied by General Optics Co, Ltd. with dimension of 1 inch in diameter and 0.375 inch in thickness. One of them was coated by JAE with design of 29 layers as highest possible reflectivity mirror, while the other was coated with 15 layers for 1.2% transmission. These plate mirrors were contacted on aluminum masses and then used as suspended mirrors.

Mode Cleaner Mirrors

Mirror substrates for MC are fused silica whose dimensions are 20mm in diameter and 5mm in thickness. Reflecting surface of input mirror of MC cavity is flat and radius of curvature of back mirror is 6000mm for 3.75m cavity. These were polished by JAE and resulting figure error were below $\lambda/10$ and microroughness were about 0.7Å. They were

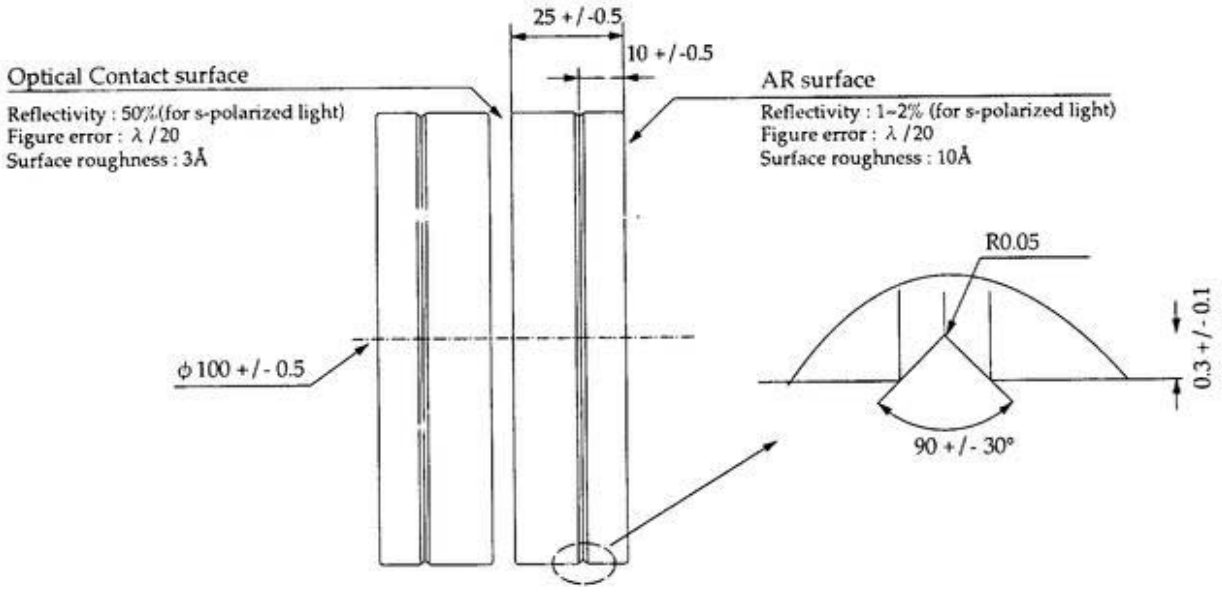

Figure 3.6: Design of Beam Splitter.

also coated by JAE with design of 21layers whose design reflectivity are $r_{MC}^2 = 0.9985$ and optically contacted on center holed fused silica spacer as is shown in Fig.3.7.

3.1.3 Core2: Light Source

Laser System

It is almost standard idea to use Nd:YAG laser as a light source for laser interferometric gravitational wave antenna, because of its high-efficiency of current-light conversion and its stability with respect to frequency and power. As a reference, typical characteristics on stabilities are summarized in table 3.2 about Nd:YAG laser and Ar^+ gas laser, which had been adopted for Delay Line prototype interferometer, TENKO100 at ISAS. [20, 21] The laser-diode (LD) pumped Nd:YAG laser whose emission wave length is 1064nm was employed as a light source also for 20m prototype. It was a first experimental trial to use high power IR light over 100mW on prototype class interferometer at that time.[18] One of most stable commercial model (MISER, Model:122- 1064-500-F, Lightwave Electronics Corp.) was selected which has Non-Planar Ring Oscillator (NPRO) configuration in its laser

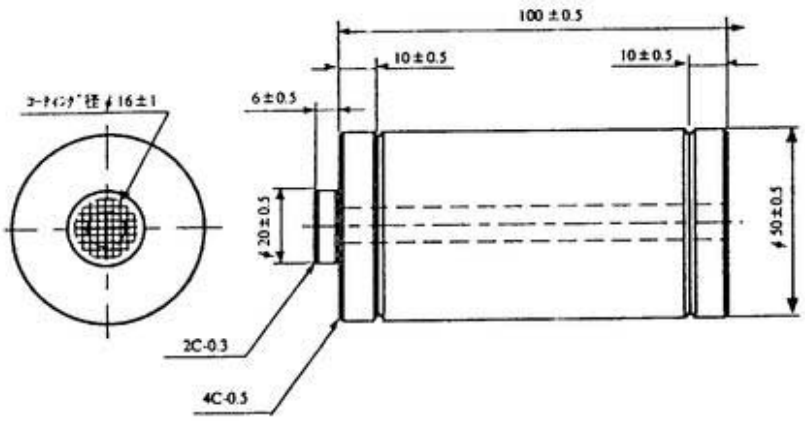

Figure 3.7: Design of MC mirrors.

	Nd:YAG	Ar^+
Frequency Noise [Hz/$\sqrt{\text{Hz}}$]	10^2@100 [Hz]	10^5@100 [Hz]
	10^{-1}@100 [kHz]	10^0@100 [kHz]
Intensity Noise	< 0.1 [% rms]	1 [%]

Table 3.2: Comparison of frequency and intensity stability of free running laser, between Nd:YAG and Ar^+ laser.

Model	Wavelength	Material	Q	Aperture	Modulation Depth
4003 nominal	1.0-1.6 [μm]	$LiNbO_3$	100	2mmϕ	> 0.2[rad/V]
(18MHz) measured					0.21[rad/V]
4003 nominal	1.0-1.6 [μm]	$LiTaO_3$	100-200	2mmϕ	> 0.2[rad/V]
(40MHz) measured					0.23[rad/V]

Table 3.3: Specifications for 18 and 40 MHz resonant Electro-Optic Modulator.

head as a resonator. The output power is 511mW and its wave length can be thermally controlled and be tunable with attached PZT on the resonator.

Phase Modulators

Optical phase modulations are imposed on incident laser light to the MC in order to utilize the Pound-Drever-Hall locking technique for control of MC and interferometer, which will be described in later section. The modulation frequencies were chosen to be RF frequencies, 18 and 40 MHz for MC and main interferometer control respectively, so as to avoid the effect of intensity noise of the laser light over shot noise on phase modulated sidebands. These phase modulations were realized by using Electro-Optic Modulators (EOM) supplied by New Focus, Inc. (Model 4003). The electro-optic crystals, lithium tantalate, are equipped with resonant circuits which were tuned to each specific frequencies so that low input voltage can drive EOMs and maintain the appropriate modulation index. The modulation performances were measured by previous work as is listed in Tabel 3.3.[20, 18]

Mode Cleaner

This prototype interferometer is equipped with a pre-Fabry-Perot cavity, called a Mode Cleaner (MC), which mainly provides a mode-cleaning effect and reduces the beam jitter of the laser light.[23] Two small mirrors which were optically contacted on the silica rods were independently suspended by double pendulums with 3.75m separation and housed by vacuum chambers. These two mirrors compose a FP cavity, that is, a linear MC and laser light illuminate the cavity from the flat mirror side. Designed reflectivities for each mirror were both $R = 0.9986$ and measured cavity finesse by using frequency response method was $\mathcal{F} \simeq 2100$, which can be interpreted to have equivalent reflectivity of $R = 0.9985$. The

throughput power ratio of the MC, $\eta_T^{MC} = P_{throughput}/P_{input}$, is about 0.8, which implies that the total loss of the MC cavity per one optic is about 100 ppm.

Once the separation of two mirror ℓ is fixed, the wave length of the light which can resonate inside the cavity can be determined exactly by the resonant condition $\exp(-i4\pi\nu\ell/c) = -1$. Frequency separation between neighboring resonance is called as Free Spectral Range (FSR), which can be defined as $\nu_{FSR} = c/2\ell$. In order to pass the 40MHz RF phase modulation sidebands for interferometer control through the mode cleaner, the cavity length of MC was chosen to be 3750mm to make its FSR agree with 40MHz, as is seen in Fig. 3.8. This technique is called "side band transmission", which is thought to

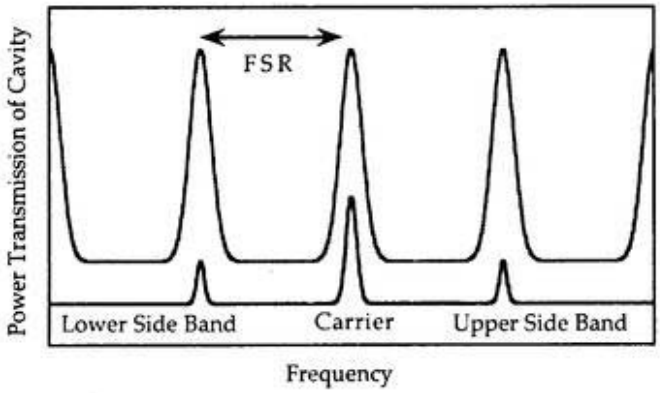

Figure 3.8: The relation of FSR and side band frequency for side ban transmission.

be preferable optical configuration for full configured interferometer. Because the EOM for interferometer control, which can degrade the spatial mode of cleaned beam from the MC, can be located in front of the MC. Moreover, the frequency difference between sidebands and corresponding FSR should be kept sufficiently small, for example with 1Hz accuracy[24], to avoid the excess intensity noise due to FM-AM conversion.

Another important feature for this MC is a roll of frequency reference. As the mode cleaner cavity and FP cavities in the interferometer are controlled by using Pound-Drever-

Hall method, the 18MHz and 40MHz phase modulations are impressed by the EOMs inserted after the laser. The error signal which was obtained by demodulating the reflected light of MC with 18MHz local RF signal is fed back to the coil-magnet actuators on the MC mirrors for length control of test masses in low frequency range (<30Hz) and to PZT actuator of the laser in high frequency range (>30Hz), so emission frequency of laser light is frequency stabilized by using MC cavity as a reference cavity in high frequency range. Frequency noise of free running laser was stabilized down to $10^{-3}\mathrm{Hz}/\sqrt{\mathrm{Hz}}$ at 1kHz by using MC as frequency reference as is shown in Fig.3.9.

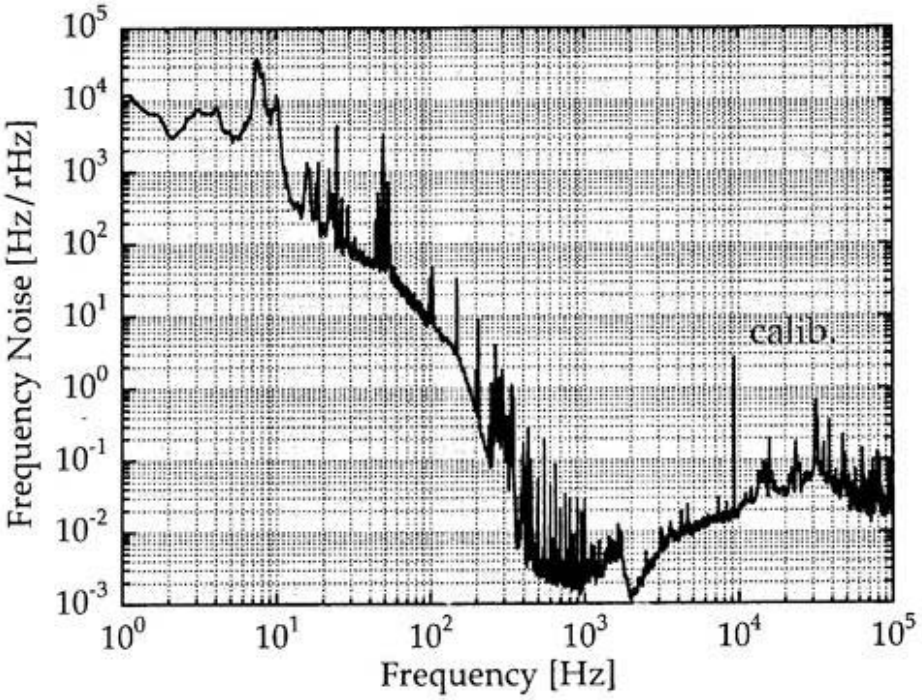

Figure 3.9: Stabilized frequency noise of transmitted light of Mode Cleaner. The noise was estimated by arm cavity as a independent reference.

3.1.4 Core3: Suspension System

Intrinsically, the interferometric gravitational wave detector have to measure the strain of the spacetime. In this meaning, mirrors of interferometer as references of space, have to be free from any force, in other words, have to be floating in a space. Though it is quite difficult to realize this condition in its real meaning on a ground based interferometer, in all direction at least, some devises can attain these requirement within a good approximation. It is common and simple way to use "pendulum-like" low-pass devices to isolate seismic motion of the ground by making use of their transfer functions. For many of prototype and full scale interferometers in the world, stack system and pendulum are standard devices as a "pendulum-like" devices.

Stack System

For many interferometers, the stack system is adopted as a supporting system of the bread boards, on which all of the optics inside the vacuum chamber are arranged. Basically, stack system are multi stage piling of masses and elastic bodies, which can be some kind of rubber or spring. These systems can have a typical resonance and the motion of the ground will be attenuated according to the transfer function of this system above resonant frequency. The designed stack system for TAMA300 and 20m prototype are compared in Fig.3.10 TAMA stack is fundamentally a three stage stack which can give 60dB/dec isolation ratio, while that for 20m is quasi-three stage stack which can provide equivalently about 20dB/dec isolation. Typical power spectrum of ground motion and that of attenuated seismic motion on the bread board by stack system of center chamber of 20m prototype is shown in Fig.3.11. These low frequency motion was sensed by using the accelerometer supplied by TEAC (Model 710) and fourier transformed by the FFT analyzer (Hewlett Packerd Model HP3562A). By dividing these spectra, the amplitude transfer function can be calculated as in the Fig.3.12. As is seen, the stack system has typical resonant frequency of about 6Hz and this system works as about 20dB/dec isolation device above this frequency.

Double Pendulum

As a final stage of suspension system, a pendulum is adopted for supporting test masses. Though this pendulum system is expected to attenuate surrounding motion as much as possible at observation frequency range, it is almost not realistic to attain a required

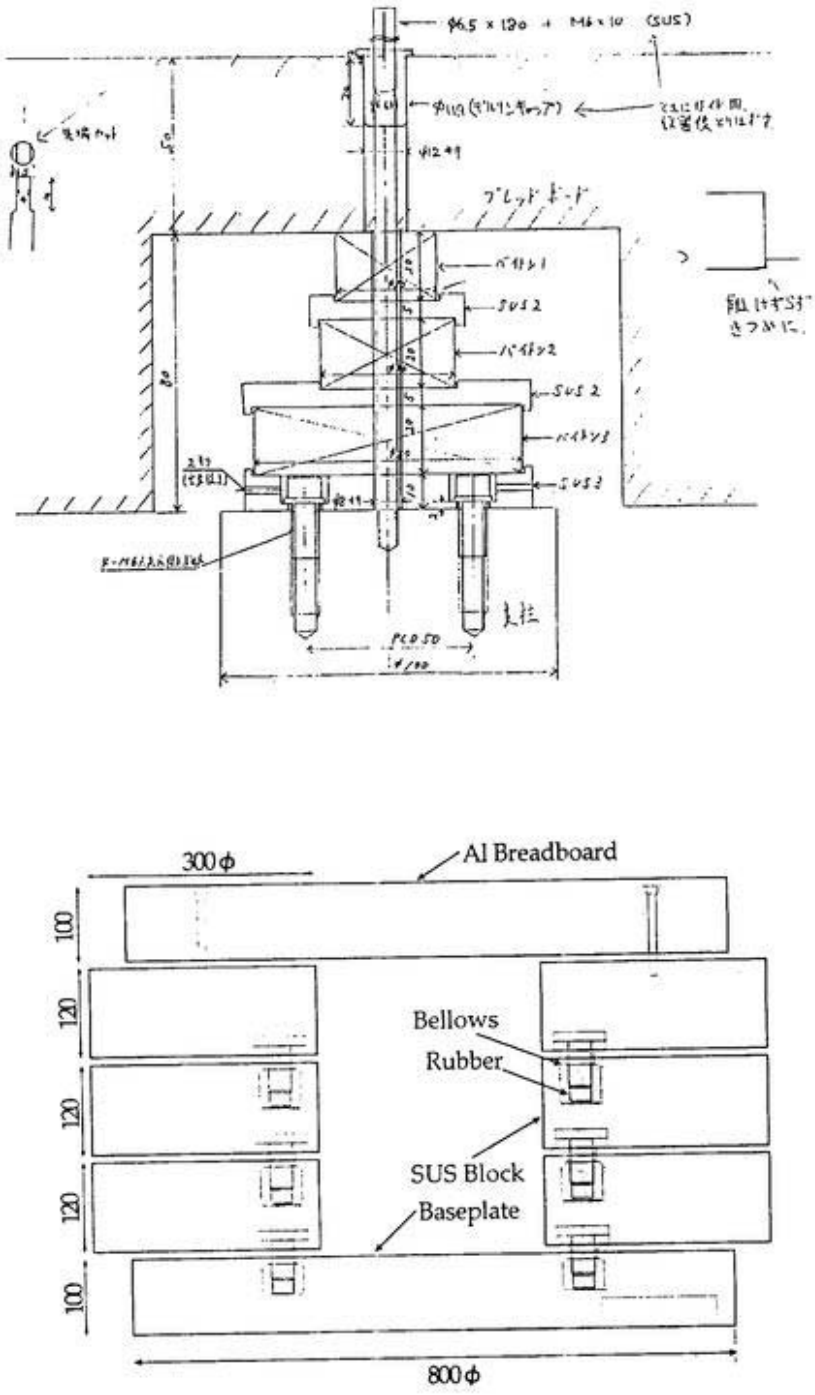

Figure 3.10: Stack systems for 20m prototype and for TAMA300.

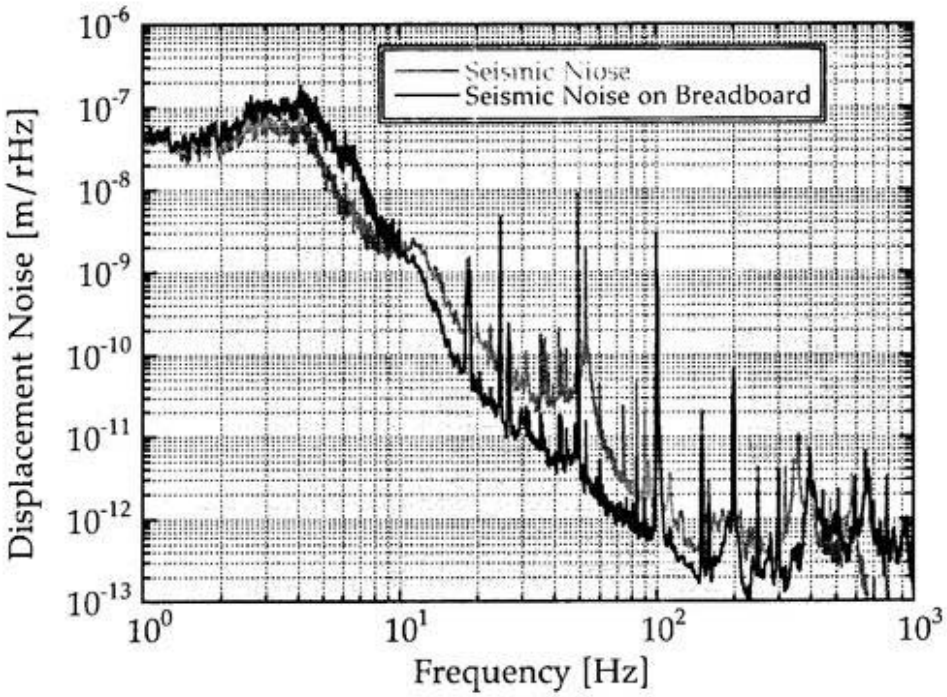

Figure 3.11: Seismic noise spectrum on the ground and that on the bread board.

isolation ratio by single pendulum with limited space: the lower resonant frequency, which mean the longer pendulum, will be needed for better isolation ratio at specific frequency range. So, it is easy to use multi stage pendulum with respect to the horizontal isolation ratio. From this point of view, double pendulum system is employed for this prototype and TAMA300. The whole view of double pendulum for arm mirrors and recycling mirror of 20m prototype are shown in Fig.3.13 In general, as the vibration isolation ratio of n-stage pendulum system above its resonance frequency can be approximated as 40dB/dec, 80dB/dec of isolation can be expected for double pendulum. However, pendulum has typical resonance and mass is swinging largely at resonant frequency, so intermediate mass is magnetically dumped in order to damp this resonance at the sacrifice of isolation ratio. As a result, these pendulum system have 60dB/dec of isolation ratio at high frequency range above about 10Hz in design.

For vertical isolation, blade springs are used at each side of cramp point of the wire of intermediate mass. Though this can attenuate the vertical motion and resulting pith motion of the mirror at above resonant frequency, it is resonating at resonant frequencies with no dumping system. This pith motion can be easily excited by seismic noise, especially by

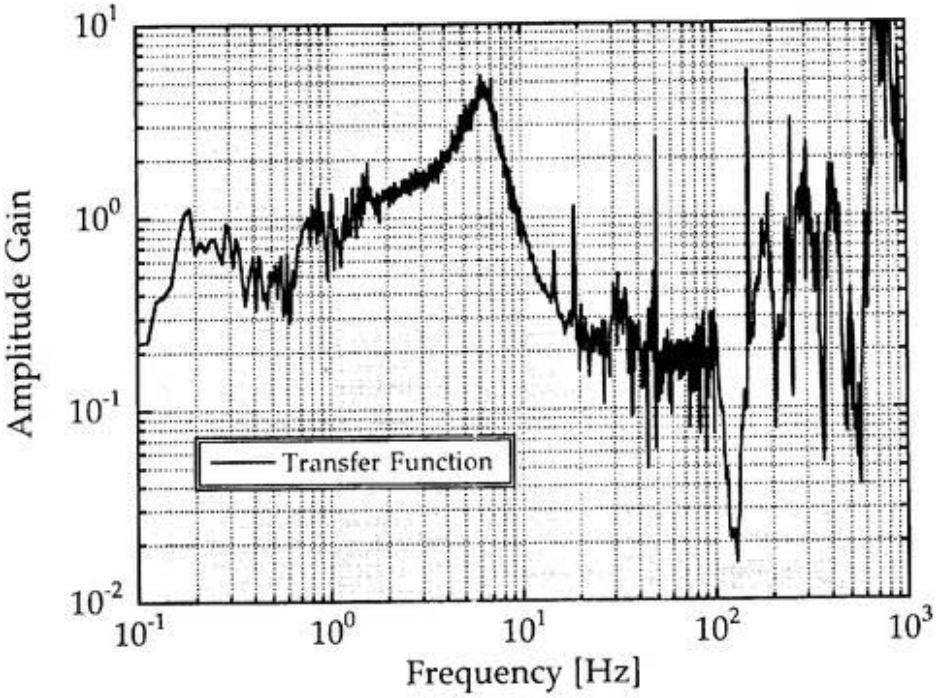

Figure 3.12: Transfer function of stack system of center chamber.

artificial ground motion, and become serious problem for recycling. This will be explained in later section about alignment control in detail.

Actuator System

In order to control the positions of mirrors to keep FP cavity resonant, coil-magnet actuator system was introduced combined with pendulum systems. Four Nd magnets which are stuck on the mirror and four coils fixed on the pendulum flame work as a actuator by applying the control current. Magnets whose dimension is 2mm in diameter and 10mm in length are stuck on a small silica spacer, which are optically contacted on the AR coating surface, with minimum adhesive. The reason for use of silica spacers was to avoid the direct contamination of the mirror coating surface due to an adhesive.

These four sets of magnet coil actuator systems are arranged as a square shape, each set can be actuated independently. Making use of this symmetrical configuration of actuators, not only the length control signal but alignment control signal can be fed back to these actuators.

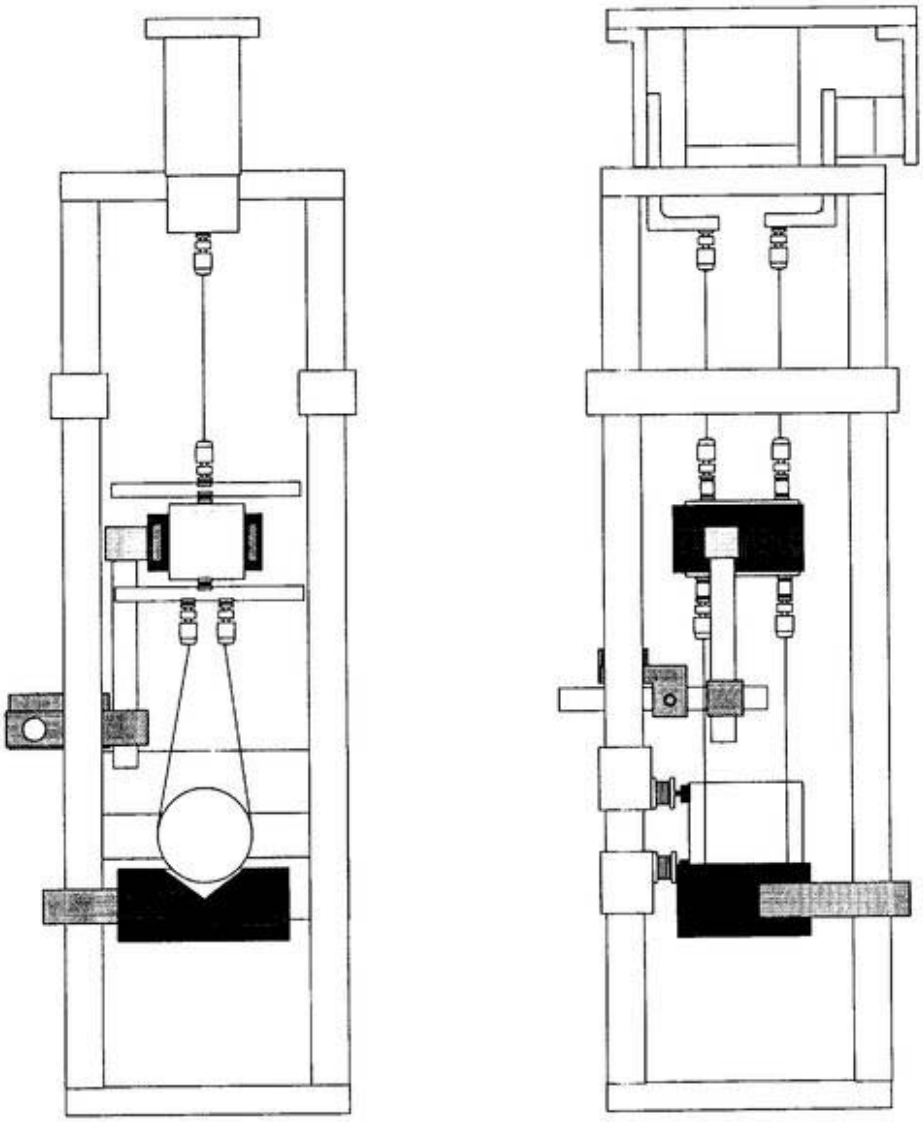

Figure 3.13: Design of double pendulum for 20m prototype. The intermediate mass is magnetically dumped with Nd magnets

Model	Photo Diode	Center frequency	Q	Conversion Gain	Dark Current
New Focus	InGaAs	38.5 [MHz]	10	1.3 [kV/W]	95 [μW]
1811	(0.3mmϕ)				
T.I.K.	InGaAs	~40 [MHz]	~10	1.5 [kV/A]	500 [μW]
	(1.0mmϕ)				

Table 3.4: Specifications of photo detectors for length sensing. Typical values are listed among five detectors for both models.

3.1.5 Detection System

Photo Detectors

In these experiment, three types of photo detector were used for length sensing and alignment sensing. For the length sensing (LS), two types of 40MHz resonant detector, supplied by New Focus, Inc. (model 1811) and fabricated by T.I.K. were adopted. Major deference between them are aperture of photo diode and maximum input power. These specifications are summarized in Table 3.4.

On the other hand, for alignment sensing , also 40MHz resonant type detectors, Wave Front Sensors (WFS), which was manufactured by Nihon Tsushinki Co, Ltd. was used. In this detector, large aperture of four segmented photo diode supplied by EG& G (model YAG-444-4A) was used, and noise performance was not so good compared to single diode detector at that time.

The reflected light from arm cavity is detected through AR reflection of beam splitter (designed for 0.7% reflection) by 40MHz resonant type photodetector PD1 and photocurrent is down-converted with 40MHz local signal and filtered to be fed back to the coil-magnet actuators of near mirror. The cavity transmitted light is monitored by photodetector PD2 and input light to the arm cavity is also monitored by PD3 from the light towered perpendicular arm as reference light for cavity response measurement.

Demodulation System

Both LS and WFS have two out outputs respectively, DC and RF. DC outputs are mainly used for monitoring, while RF outputs are demodulated, down converted to DC

and fed back to proper actuators through servo filters as control signals. Demodulation was realized by using passive double balanced mixer (DBM) multiplied properly phase shifted reference oscillator.

3.1.6 Vacuum System

Vacuum Chambers

All mirrors consists of resonating cavity, arm cavity, recycling cavity, MC cavity, are housed in vacuum chambers in order to avoid any acoustic noise and effects of fluctuations of the refractive index of the air. The designs of vacuum systems are shown in Fig.3.14 Two mirrors of MC with suspension systems were located in separate chambers, which were connected by 200mm pipe. These pipes and chambers are made of stainless steel. There is gate valve (GV) with optical window at the end of MC chamber, so MC systems can be evacuated and operated independently of main interferometer.

The main interferometer consists of three chambers, center and two end chambers, and connecting pipes. These chambers and pipes were made of aluminum alloy and each can be connected easily with quick coupling flange. The center chamber house a large bread board, whose dimension is 1200mm in diameter and 130mm in thickness, and steering optics, beam splitter and input mirrors of arm cavities were installed on it. On the other hand, end chambers house small size bread board with back mirror suspension system.

These all vacuum chambers and pipes were finally surface treated by glass beads blasting in oxygen and argon atmosphere (EX-GBB) with no baking and attainable pressure was below 10^{-7} torr without optics. Even at operational mode with full optics, the system can be evacuated down to the pressure of a few 10^{-7} at the center for the pipes and down to 10^{-8} torr at MC pipes.

Pumping System

The two sets of the Turbo Molecular Pump (TMP) and the rotary pump (PR) at the center of the arm pipes are used as a main pumping system and the cryogenic pumps are available for further pumping down to 10^{-8} torr. Another set of TMP and RP is equipped with MC for independent operation. In other words, MC can be kept vacuum at a few 10^{-8} torr during optical configuration change by opening the center chamber. Each specifications are summarized in Table3.5.

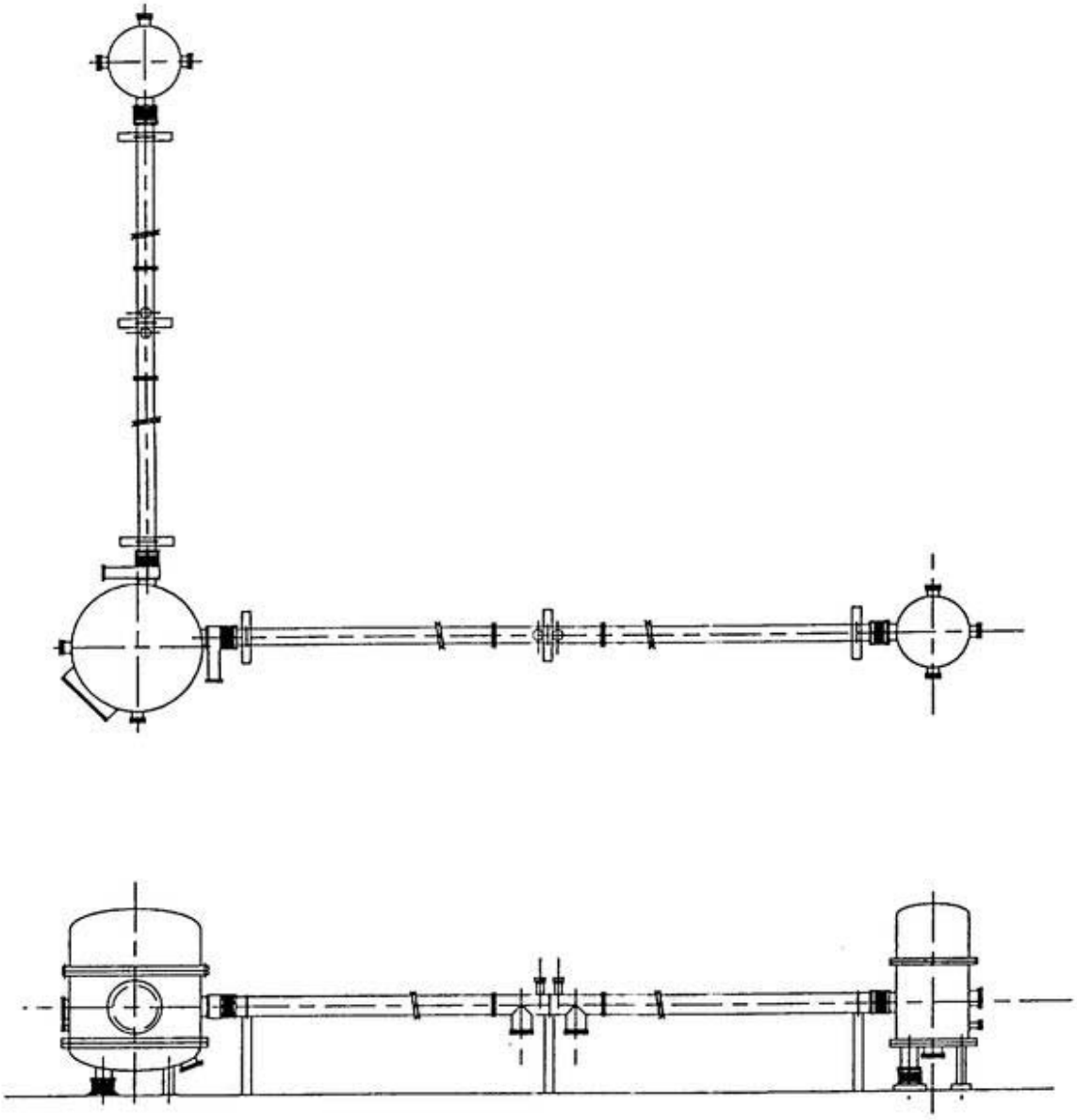

Figure 3.14: Whole vacuum systems of 20m prototype.

	Model	Evacuation Speed
TMP1,2	SEIKO Seiki	1000 [ℓ/sec]
TMP3	SEIKO Seiki	400 [ℓ/sec]
CP	DAIKIN	1500 [ℓ/sec]

Table 3.5: Specification of pumping systems.

3.2 Loss Measurement of Optics

3.2.1 Theory of Loss Measurement

In general, the transmission and reflection efficiency of a Fabry-Perot optical cavity comprising input and back mirrors are expressed as a function of their amplitude reflectance (r), transmission (t) and optical round trip phase between them. If these two mirrors are simultaneously coated using the same coating process and can be assumed to be identical, the on-resonant transmission and reflection efficiency (η_T, η_R) can be expanded as follows by using the intensity transmittance (T) of t^2, the reflectance (R) of r^2 and the total loss (A) of $A_a + A_s$ (absorption and scattering) of the mirrors:

$$\eta_T = \left(\frac{T}{1-R}\right)^2 = \left(\frac{T}{T+A}\right)^2 = \left(\frac{1}{1+A/T}\right)^2, \tag{3.1}$$

$$\eta_R = \left(\frac{A\sqrt{R}}{1-R}\right)^2 \simeq \left(\frac{A}{T+A}\right)^2 = \left(\frac{A/T}{1+A/T}\right)^2. \tag{3.2}$$

Thus, both η_T and η_R lead to the ratio of the transmittance and the total loss of one isolated mirror (A/T). On the other hand, the finesse of the cavity is expressed as

$$\mathcal{F} = \frac{\pi\sqrt{R}}{1-R}. \tag{3.3}$$

Hence, the total loss of the mirror can be calculated by measuring $\mathcal{F}, \eta_T$ or η_R and by using the energy-conservation relation $R + T + A = 1$.[25]

The quality of the mirrors for an interferometric gravitational wave detector should be finally characterized using the actual large-size beam with which the interferometer is operated, as compared with the area mapping of loss the factor with a small beam, if necessary. For this purpose, the mirrors for the 20m prototype interferometer should be

tested in two ways: one is a tabletop loss measurement with a small beam mainly for loss mapping; the other is a loss measurement using an interferometer arm cavity with a large beam for a total performance check. However, a short-length (shorter than 1m) tabletop Fabry-Perot cavity using 20m interferometer mirrors whose radii of curvature are infinity (flat) and 30m was very unstable and sensitive to seismic ground motion through the air-overpressure-spring-system of the optical table. These were mainly due to the geometrical instability of the cavity. The transverse-mode separation ratio to the longitudinal mode (the γ factor), which determines the optical-mode structure of the cavity uniquely according to its geometrical configuration, is expressed as

$$\gamma = \frac{1}{\pi}\cos^{-1}\sqrt{g_1 g_2}. \tag{3.4}$$

Here, $g_1 = 1 - \ell/R_1, g_2 = 1 - \ell/R_2$ are the geometrical factors, ℓ is the cavity length and R_1, R_2 are radii of curvature of the each mirror. [26] In this case, the γ-value was about 0.0412 for a 0.5m length cavity due to an imbalance between $\ell = 0.5$m and $R_2 = 30$m. For the conventional cavity design of the gravitational wave detector, the γ-value is selected so that the longitudinal and transverse modes do not degenerate, typically about 0.3 (for example, $g_1 = 1, g_2 = 1/3$). Consequently, the transverse modes were too close to the longitudinal mode to sufficiently isolate it and to keep the cavity lock stable and robust. Thus, small test pieces whose geometries were suitable for a short cavity ($\gamma = 0.3$) were used to map the loss distribution instead of the 20m interferometer mirrors, themselves.

For a loss measurement using the 20m prototype interferometer,since all of mirrors in the interferometer were independently suspended, as described below, a low-frequency (typically under 10Hz) mirror motion excited by seismic motion through pendulum resonances is usually large in comparison with a rigid or a fixed cavity on the optical table. Furthermore, the cavity should have a high finesse of over 10^4 and a storage time of over 1msec. This means that the cavity shows a typical dopplar effect on the resonant lineshape of the transmitted and reflected light when the mirrors are left to be free to oscillate along the optical axis.

On the other hand, as a method to measure the high- reflectance of a mirror which exceeds R=0.999, three techniques have been established: the AM sideband method, the transfer-function method[25] and the ring- down method.[27] From the above discussions, the frequency-response method, which is performed during cavity on-resonance, was most a suitable method for a finesse measurement, because the measurement accuracies of the

two other methods depend on the stillness of each mirror over a time scale equal to the storage time without any feed-back control.

3.2.2 Experimental Setup

Total-loss measurements were demonstrated with a tabletop experimental setup and with a suspended FP cavity of the 20m prototype interferometer (using a transmitted light through beam splitter), as shown in Fig.3.15, 3.16. Though the tabletop measurement was mainly performed by Dr. Miyoki, it is worth while to be described precisely here involved with the result of interferometer cavity.

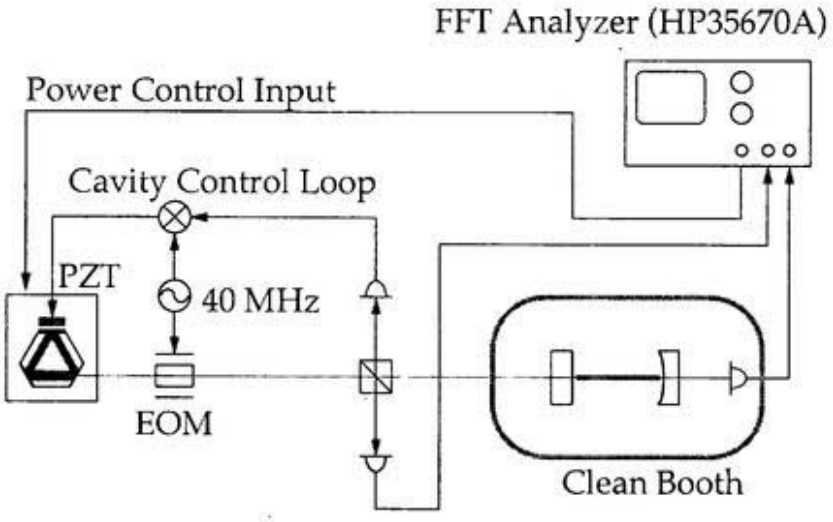

Figure 3.15: Optical configuration of the tabletop experiment.

The light sources were diode-pumped cw single frequency Nd:YAG lasers (Lightwave Electronics Co,Ltd Model 120 03A and Model 122) whose emission wavelengths were 1064nm and output powers were 40mW and 500mW, respectively, to illuminate the cavities.

Tabletop

The beam profiles of output light within vertical and horizontal plains are different due to its laser cavity configuration; Non-Planar Ring Oscillator (NPRO), so the cylindrical lenses and mode matching lens which are inserted in an input optics chain forms the beam shape in a plane perpendicular to the beam axis into round shape and makes it mode

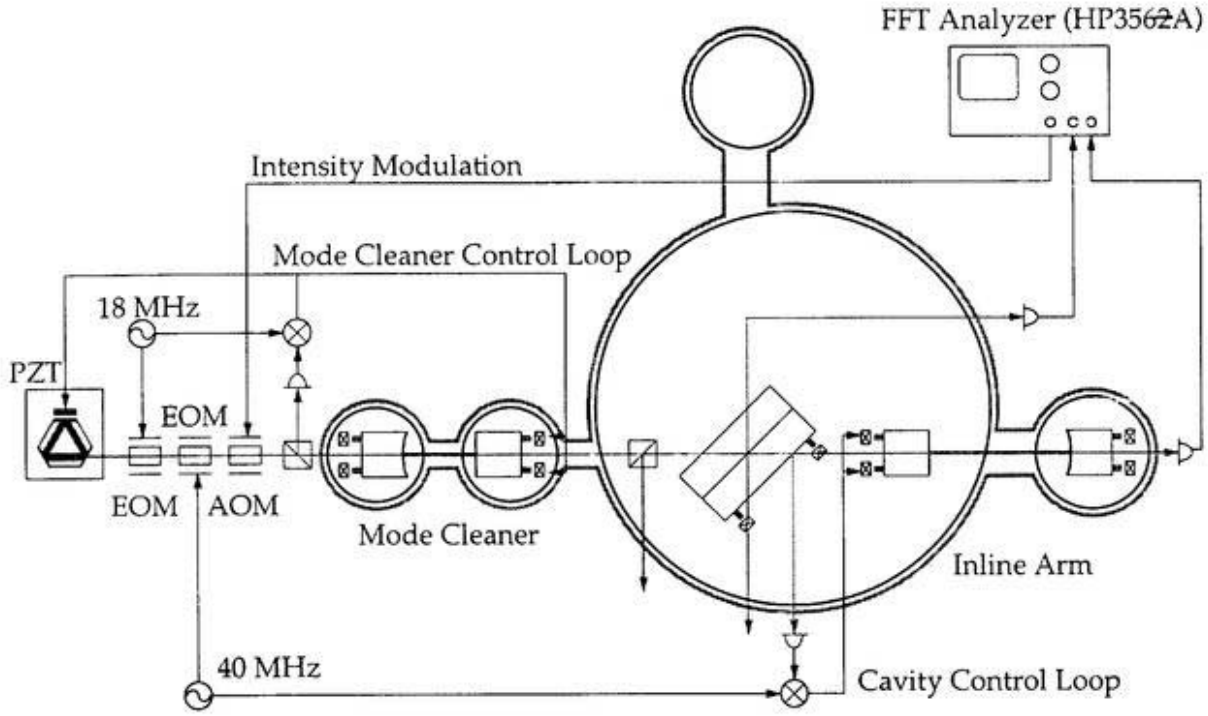

Figure 3.16: Optical configuration of the 20m base-line laser interferometer.

matched to the cavity. In order to length control the cavity using Pound-Drever method, the incident light is phase modulated by the electro-optic modulator(EOM) inserted after the laser with 40MHz and the light reflected by the cavity is picked up through optical circulator which consists of PBS and $\lambda/4$. This reflected light is detected by the 40MHz resonant type photodetector PD1 and demodulated with phase coherent 40MHz local signal to be fed back to the piezoelectric transducer (PZT) and thermal control of the laser as an feedback signal. The cavity is kept on resonance using this technique and laser frequency is stabilized by 'open cavity' as a reference cavity. The power control input of the laser serves as an intensity modulator for frequency response measurement of the cavity.

20m Interferometer

All of the Fabry-Perot cavities used in the setups were length controlled to be kept on the resonance using the Pound-Drever method, and the error signals were fed back to the piezoelectric transducer (PZT) of the laser and/or coil-magnet actuators of the mirrors.

Optics

The mirror substrates of the test pieces used for the tabletop experiment were 20mm in diameter and 5mm thick. The monolithic mirror blanks for the end mirrors of the interferometer had dimensions of 50mm in diameter and 60mm in thickness, and the substrates for the near mirrors were 1.5 inch in diameter with a thickness of 0.375 inch, which were used with aluminum test masses contacted on it. All of these mirror substrates were superpolished and coated by an IBS coating machine. The figure error of these substrates was measured to be better than $\lambda/20$ by a Zygo interferometer (ZYGO GPI-XP HR) at λ=633nm, and the microroughness was measured to be below 1Årms by a stylus profiler (Talystep) for monolithic mirrors. The high-reflectance coating was 29 layers of SiO_2/Ta_2O_5 quarter-wave films with an SiO_2 half-wave top layer, and its designed intensity reflectance was just below 0.9999.[28] Since these mirrors used for the interferometer and test pieces for the tabletop experiment were simultaneously coated by the same coating process, the macroscopic and microscopic features of the coatings were assumed to be identical, or equivalent, in the ideal case. Two high-reflectance mirrors for the tabletop cavity, whose radii of curvature were flat and 1000mm concave, were supported by mirror mounts which were rigidly fixed on the optical table and housed in an air clean bench with a separation of 600mm. In particular, since the mirror mount holding the input mirror was based on an x-y stage, the input mirror could be moved along its mirror surface and the incident beam could illuminate different positions of the coating surface of the input mirror.

The important features of this experiment, performed with the 20m interferometer, are its optical configurations. The expected cavity finesse is about 30000 and the mean storage time of each photon will exceed 1.27 msec using the designed mirror reflectance. This corresponds to a cavity line width of 125Hz, which is extremely narrow compared to the typical laser line width, and, in general, will make a cavity with swinging mirrors hard to acquire a lock. However, owing to the adequately-frequency stabilized laser light to a level of 10^{-3} Hz/$\sqrt{\text{Hz}}$ at 1kHz by the well- developed mode cleaner, cavity lock-acquisition was easily realized using only magnet-coil actuators; the lock was kept stable and robust for over one hour without any impulsive seismic excitations. The unity gain frequency was about a few kHz during the finesse measurement. This 20m-long cavity, demonstrated here, is the highest in finesse and the longest in storage time ever reported as an independently suspended mirror cavity, especially for an interferometric gravitational wave detector. The circulating power of light inside the cavity reached up to about 700W and the energy

density was over 4.6kW/cm^2 on the input mirror surface.

Finesse Measurement

The frequency-response function of a Fabry-Perot cavity is written in a complex domain as a function of the Fourier frequency (f),

$$H(f) = \frac{\alpha\Omega}{\omega} \sin\left(\frac{\omega l}{c}\right) e^{(-i\omega l/c)} \frac{1}{1 - r_1 r_2 e^{-2i\omega l/c}}, \tag{3.5}$$

and is expandable to the frequency dependencies of an amplitude gain and a phase, as in the limit of $R \sim 1$:

$$|H(f)| = \eta_T \frac{1}{\sqrt{1 + (f/f_c)^2}}, \tag{3.6}$$

$$\arg H(f) = -\arctan\left\{\frac{4l\mathcal{F}f}{c}\right\}, \tag{3.7}$$

$$\tag{3.8}$$

Here, f_c=$c/4\ell\mathcal{F}$ is the cut-off frequency of the cavity response function, ℓ the cavity length and $\mathcal{F}$ the finesse. Therefore, the finesse can be obtained by fitting the measured cavity transfer function with a theoretical expression, as can be seen in Figs.3.17,3.18.

The response function was measured with FFT spectrum analyzer (Hewlett Packerd Model HP35670A for tabletop experiment and HP3562A for 20m prototype) at frequency range between 10 and 10kHz by impressing an amplitude modulation on the incident beam by power controller and by AOM respectively.

Although the fitted finesses using the amplitude gain and phase for the 20m interferometer show good agreement within the accuracy, that for a tabletop experiment are different by about 1700, which corresponds to 6% of the finesse error. These discrepancies are considered to come from instabilities of the optical system, such as the change in the refractive index of air due to air flow or the very low-frequency drift of the optical system within the time of the frequency-response measurement sequence. From the partial derivative of R with respect to $\mathcal{F}$, $\partial R/\partial\mathcal{F}|_{R=0.999875} \simeq 5 \times 10^{-9}$, a finesse error of 1700 corresponds to a reflectance difference of 8.5ppm, which results in a 2ppm effect on the loss factor. The main purpose of this measurement, however, was to confirm the loss distribution of the mirror surface. Thus, an accuracy of 2ppm was sufficient to reveal the beam-size-dependencies of the mirror loss. Here, for a tabletop measurement, the finesse obtained with phase fitting

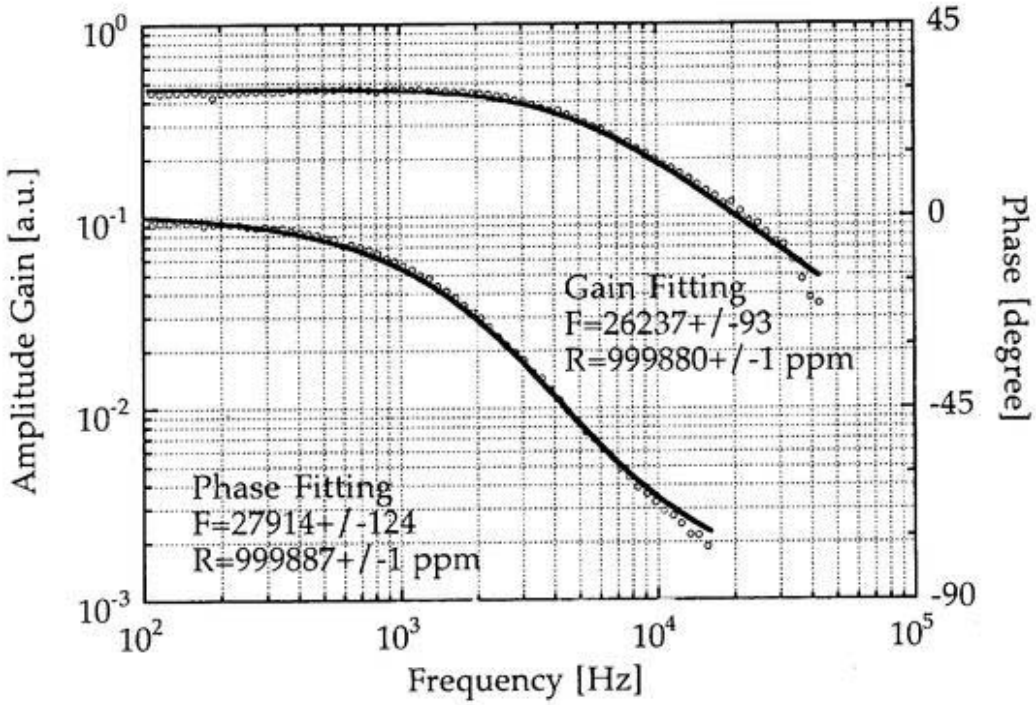

Figure 3.17: Amplitude gain and phase of the frequency-response function obtained by the tabletop experiment.

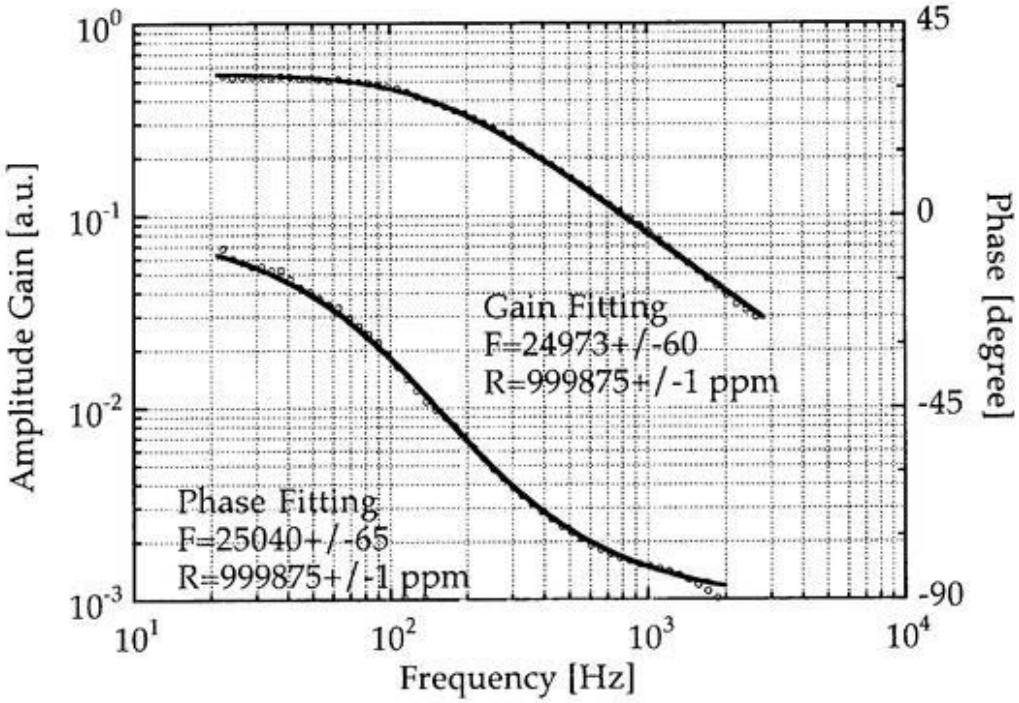

Figure 3.18: Amplitude gain and phase of the frequency-response function obtained by a loss measurement at the 20m interferometer.

Parameter	Tabletop	20m Interferometer
Beam diameter $2w$ [mm]	0.82	4.4
Cavity length [mm]	60	19900
$\mathcal{F}$	27900±130	25000±60
R [ppm]	999887±1	999875±1
η_T	0.73± 0.02	0.58±0.02
η_R	0.09± 0.002	0.045±0.002
T [ppm]	97±2	95±2
A [ppm]	16∓2	30∓2

Table 3.6: Results of total loss measurements.

was adopted for a further calculation because the uncertainty in the DC gain level of the amplitude gain made it difficult to determine the finesse.

Transmission and Reflection Efficiency

Using the incident power (P_i) matched to the cavity mode and the transmitted power (P_t), the transmission efficiency (η_T) is expressed as $\eta_T = P_t/P_i = P_t/MP_{tot}$, where P_{tot} is the total incident power and M is its mode-matching ratio to the cavity TEM_{00} mode. Note that for the interferometer, since the incident light to the arm cavity is also the output beam from the mode cleaner, the non-Gaussian component of the beam is naturally assumed to be small compared with the laser emission beam, itself. Furthermore, a mode calculation using the measured beam radii at a few points along its propagation axis assured that the mode-matching ratio exceeded 0.99. The measured parameters and their results are summarized in Table 3.6.

The attached error terms are based on the supposed standard deviations with a parameter fitting for the finesse and the fluctuation of the amplitude or the stability of the observables in the time domain for the transmission and the reflection efficiency. Intrinsically, the loss-transmission ratio (A/T) obtained by η_T and η_R should agree if the mode matching is perfect. Actually, the evaluated two losses using $\mathcal{F}, \eta_T$ and $\mathcal{F}, \eta_R$ are almost the same within the accuracy for the 20m interferometer, owing to its good mode-matching ratio and nearly perfect Gaussian beam. However, for a tabletop measurement, the resulting two

show a difference having about a factor of two, which results mainly from the insufficient mode-matching ratio without a mode cleaner, in spite of the use of two cylindrical lenses for better mode-matching. With these optical configurations (two mirrors are identical), since the beam component matched to the cavity mode will transmit the cavity, η_R is very sensitive to and affected by the mode-unmatched ingredients of the incident beam. From this point of view, it is more reliable to adopt that obtained by $\mathcal{F}$ and η_T.

Two Dimensional Loss Distribution

Furthermore, the loss distribution of the input mirror was mapped using the same method by moving the x-y stage mounting the input mirror with a 0.5mm step in the horizontal direction and a 1mm step in the vertical direction; the result of a two-dimensional loss mapping is shown in Fig.3.19.

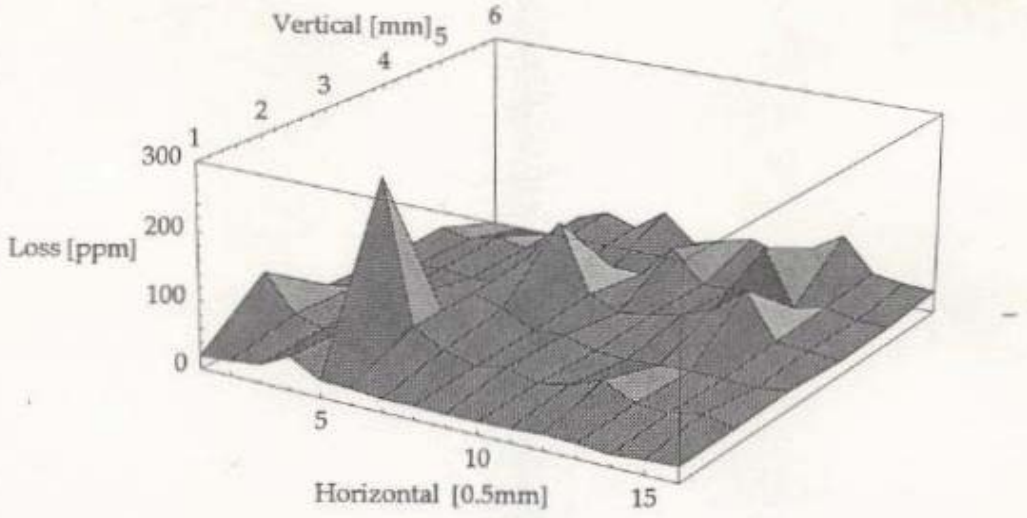

Figure 3.19: Loss distribution within a coating surface. The several high peaks are due to point-like defects.

Note that in this procedure the two mirrors are not exactly identical. The loss of the end mirror was fixed to be 16ppm and the decrease in the transmission efficiency of the cavity

was attributed to an increase in the loss of the input mirror. Although the loss increase rate to the transmission efficiency, $\partial A/\partial \eta_T$, depends on the loss mechanisms, they will agree within the accuracy of the series of measurements up to a few 10ppm of the additional loss.

3.2.3 Experimental Results

The total loss of the IBS coating mirrors was measured using the small beam on the table-top experiment and using the large beam of the 20m laser interferometer. The experimental result of a loss of 16ppm with a small beam of about $2w$=0.82mm is the best value around the center of the test piece, and that of the loss measurement at 20m interferometer shows a minimum loss of 30ppm for a beam with a spot size of $2w$=8mm at the end mirrors. These measured values are predominant over their accuracy of a few ppm, respectively. Since the Total Integrated Scattering (TIS) due to the microroughness σ of the mirror substrate, which is defined as TIS=$(4\pi\sigma/\lambda)^2$, is estimated to be below 1ppm, the microroughness of the substrate is negligible. And for the table-top experiment, total loss due to the air including absorption and scattering from particles can be limited to 0.8ppm/10cm according to previous work.[11] So, the scattering from the multi-layer coatings are most probable host which largely contributes to the total-loss factor of the mirror. According to loss mapp by moving the input mirror, the equivalent loss distribution is not uniform on the 0.5mm scale, and varies between 16 and 270ppm. These high-loss peaks seem to arise from point-like defects, scattering sources. Such defects are visible, and thought to be stimulated by the small dust included during coating processes. This map means that the fraction of the large beam ($w >$ a few mm) cannot avoid illuminating the lossy area on the coating surface, and thus the total loss for the large beam will increase. Though the area-averaged value around the plain area in Fig.3.19 gives a relatively small loss of 27ppm, which is close to the loss for the large beam, the averaged loss using all of the measured data increases up to 40 ppm due to several strong loss (scattering) sources. These results imply that the mirror loss depends on the structure of the loss distribution, and that its dependencies are not linear to the beam size; that is, the loss will increase with the beam size according to the density of such high-loss defects. In these experiment, as the mean separation of defects and beam size of 20m interferometer was comparable, it was possible to avoid major effects of these high-loss defects. As a result, the loss factor of 20m-size beam could be reproduced by averaging the mapped loss factor around the plain area, which shows no apparent evidence

on optical phase induced loss for big size beam. Though these point-like defects and its density will be further reduced by advanced coating techniques in near future, it is possible that beam propagation simulation program will become useful for further study, in which optical phase correlation from each part of mirror is important, for more large size beam, for example TAMA300.

Consequently, the loss distribution is acceptable for the 20m interferometer and the TAMA project with respect to the interferometer design and its requirements. Of course, it should be minimized as much as possible in order to reduce any optical losses in the interferometer. Further effort will be the next subject for the advanced detector or the full-scale detector, which may require even smaller losses for the optical elements.

3.3 Power Recycling

3.3.1 Optical Design

Configurations

The optical arrangement of power recycling is shown in Fig.3.20.

Optics

The optical parameters for all optics which are used in a recycled interferometer are summarized in Table 3.7. The designed reflectivity for the arm cavity mirrors are $R_{BM} = 0.9999$ for the back mirrors and $R_{IM} = 0.96$ for the input mirrors. Therefore, the expected finesse of cavities are 130 and reflection efficiency exceeds 0.99 with no loss assumption. The most important reason why the cavity finesse was lowered was to obtain a enough reflectivities of the FPMI even if BSAR losses are taken into account. Further more, this configuration of cavity is more tolerant to the mirror total loss in comparison with $\mathcal{F}$ =516 design cavity as is shown in Fig.3.21.

The reflectivity of the recycling mirror should be determined to be equal to that of FPMI in order to maximize the recycling gain. If the reflectivity of both recycling and compound mirror (FPMI) are exactly identical, all the carrier light will resonate in the recycling cavity and will dissipate inside the cavity. The reflectivity of FPMI can be estimated by using arm cavity reflectivity, BSAR loss, contrast of Michelson part and pick off mirror reflectivity as

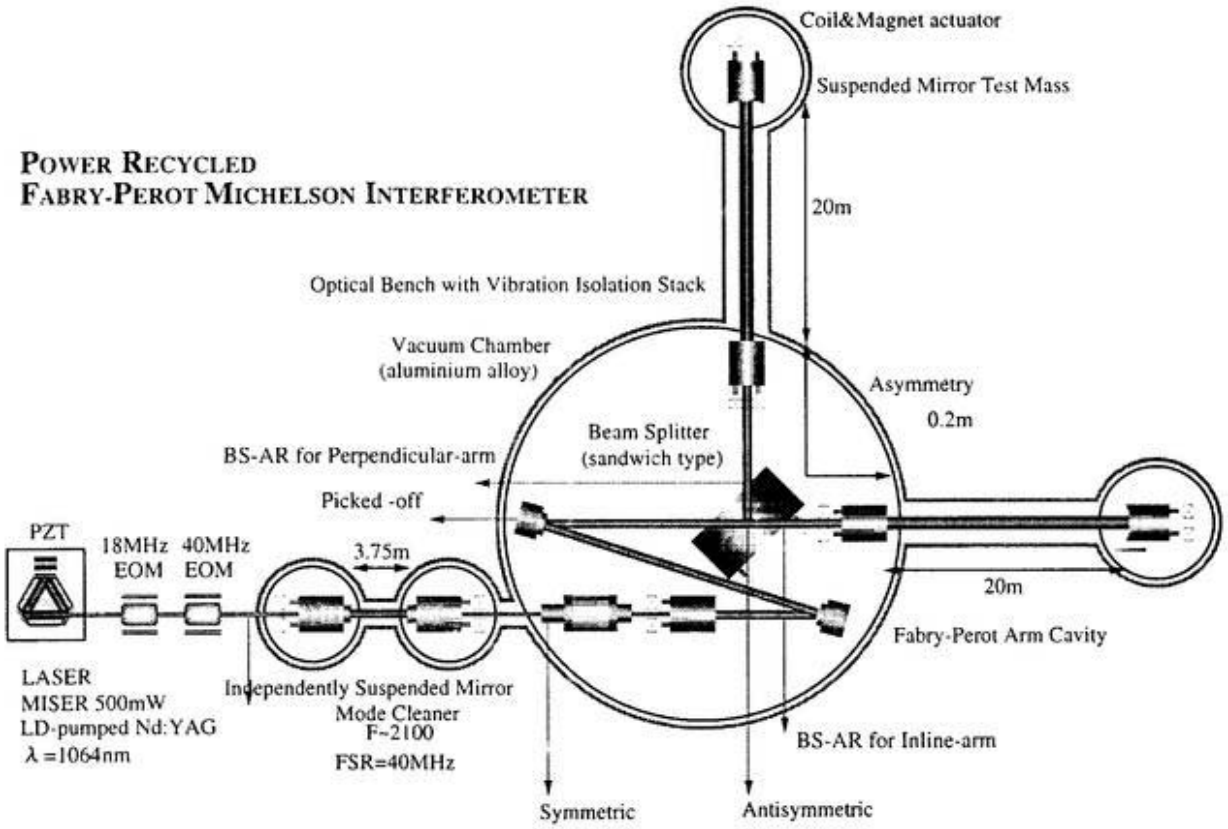

Figure 3.20: 20m.

	Coating	Designed Reflectivity
Input Mirrors	11layers	0.96
Back Mirrors	29 layers	0.9999
Recycling mirror 1	5 layers	0.7
Recycling mirror 2	7 layers	0.84
Recycling mirror 3	9 layers	0.91
Steering Mirror	29 layers	0.9999
Pick off Mirror	15layers	0.9880

Table 3.7: Design of mirrors for power recycling.

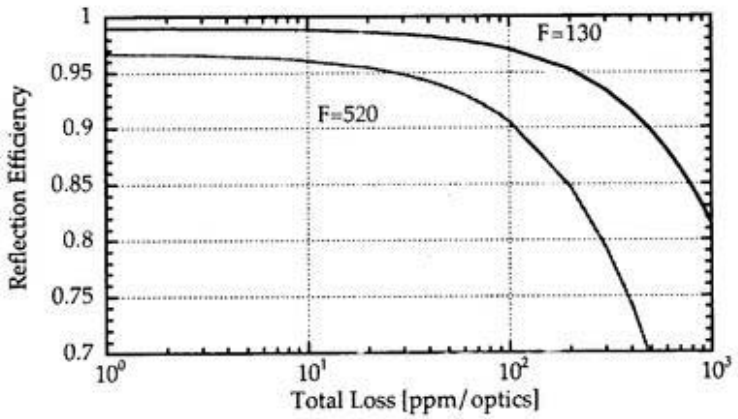

Figure 3.21: Degradation of cavity performance due to optical losses for $\mathcal{F}$ =516 and 130 cavities.

follows,

$$R_{FPMI} = \frac{P_{ref}}{P_{incident}} \tag{3.9}$$
$$= R_{cav} T_{BSAR}^4 C R_{pickoff} \tag{3.10}$$
$$= (0.98 \pm 0.02) \times (1 - 0.007)^4 \times (0.98 \pm 0.02) \times (0.988) \tag{3.11}$$
$$\simeq 0.92 \pm 0.02. \tag{3.12}$$

Similarly, the reflectivity of the FPMI for the side bands can be estimated as,

$$R_{FPMI} = \frac{P_{ref}}{P_{incident}} \tag{3.13}$$
$$= R_{cav} T_{BSAR}^4 C R_{pickoff} \cos^2 \alpha \tag{3.14}$$
$$= (0.98 \pm 0.02) \times (1 - 0.007)^4 \times (0.98 \pm 0.02) \times (0.988) \times (0.97) \tag{3.15}$$
$$\simeq 0.90 \pm 0.02. \tag{3.16}$$

In these estimations, most ambiguous factors are contrast and cavity reflectivity because the mirror loss including contamination and small misalignment can easily decrease the R_{FPMI} and contrast by a few percent. The arm cavity mirrors were aligned within a accuracy of the order of 1 [μrad] by using PZT for fine alignment tuning attached to the top of the pendulums.

Taking these estimation into account, a few recycling mirrors were fabricated by the IBS machine at the Research and Development center of National Astronomical Observatory. The designed reflectivities are 0.70, 0.84 and 0.91 with their numbers of multi-layer of 5, 7 and 9, respectively.

3.3.2 Control Design

Control Scheme

The control design is shown schematically in Fig.3.22. In these series of recycling ex-

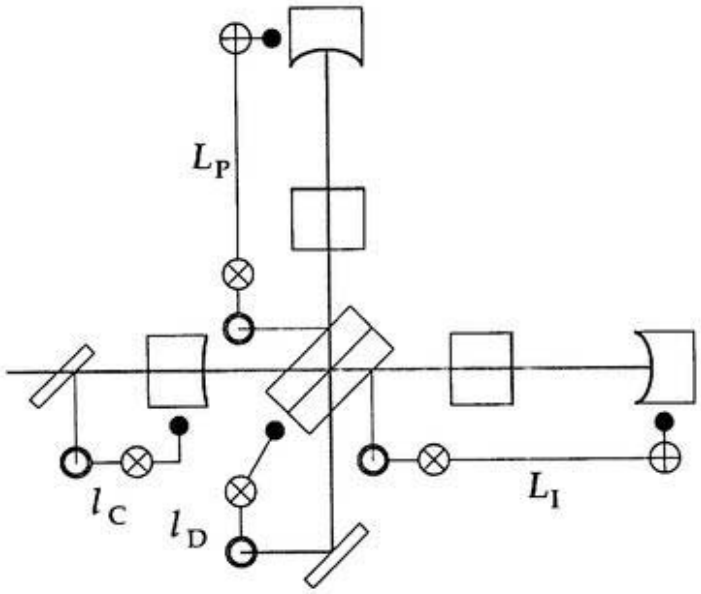

Figure 3.22: Control design for length sensing (Phase-I).

periments without alignment control system, the independent locking system was mainly used as length control design (Phase-I). The cavity reflected lights through AR reflection of beam splitter were used for each cavity control, L_I, L_P. In contrast with the case of non recycled FPMI, the control signals do not separate because the optical fields containing information of both cavity length are circulating inside the recycling cavity as is described in previous section. The signals for common length of recycling cavity l_C is expected from the

symmetric output to be fed back to the recycling mirror and differential degree of freedom l_D was pick up from the antisymmetric port to beam splitter.

As the circulating light inside the recycling cavity can be pick off through one of steering mirrors, it is possible to extract the control signals as common and differential mode of arm cavities and recycling cavity, L_C, L_D, l_C, l_D (Phase-II) Fig.3.23.

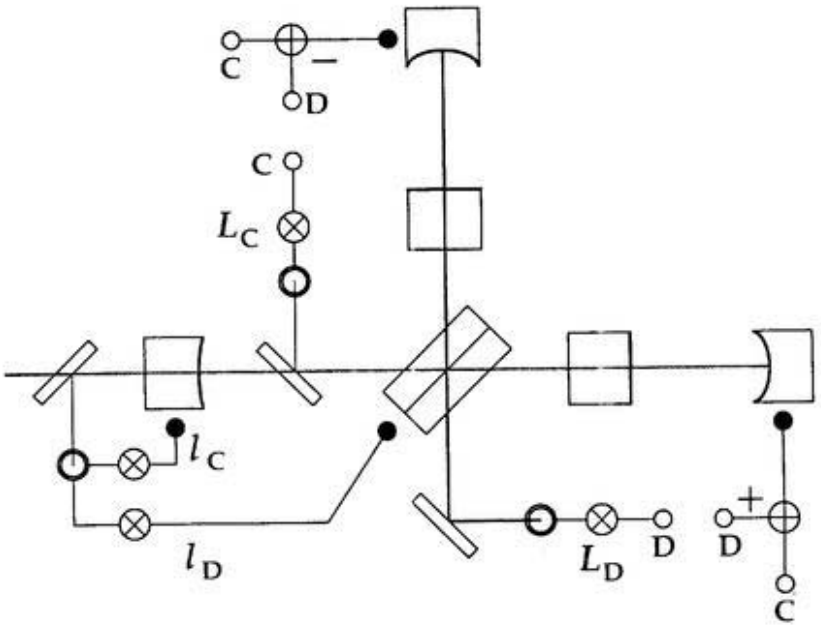

Figure 3.23: Control design for length sensing (Phase-II).

Servo Design

For Phase-I scheme, both arm cavities were locked independently first, while other degree of freedoms were kept free. This means that circulating power inside the recycling cavity changes seriously according to the free swinging motion of mirrors of Michelson part. Usually, pole-zero pair of servo circuit is used as a phase compensation for suspended mirror FP cavity. This is because lost phase of 180 degree due to pendulum transfer function have to be compensated electronically around the unity gain frequency (UGF). At the same time, phase margin can be maintained around UGF, and with this conditions closed servo system can work properly. In other words, as far as this conditions are maintained, the feed back

system is stable with gain change caused by optical and/or electronical gain fluctuations. So, the gain margin can be defined as a tolerant range of gain change which can keep the system locked. For these arm cavities, such tolerant servo filters are needed in order to absorb the optical gain change of recycling cavity.

The schematic diagram of feed back system is shown in Fig.3.24 The open loop transfer

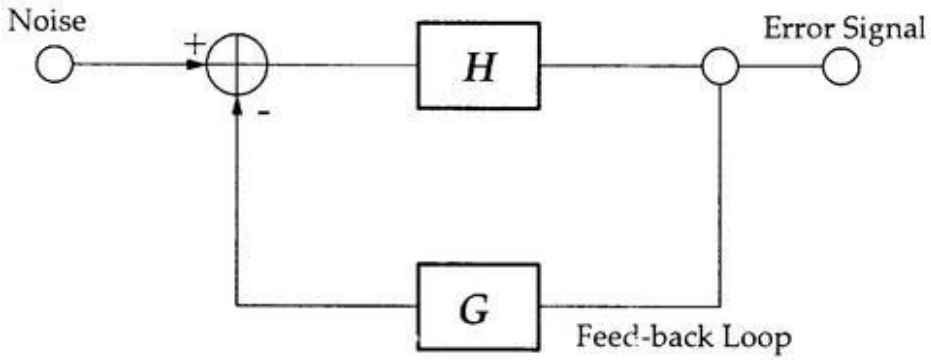

Figure 3.24: Schematic diagram of feed back system. G contains optical and detection System, while H denotes feedback and actuator system. Open loop transfer function is defined as GH.

function is defined as a product of transfer function of all elements consisting the loop. For example, open loop transfer function for one of arm cavities are shown in Fig.3.25 Major contributions around these frequency range are f^{-2} decrease due to pendulum and phase compensation around UGF, if other electronics have a flat transfer functions here. As can be seen, phase margin for 1kHz UGF is about 50 degree and 40dB of gain margin can be expected.

3.3.3 Lock Acquisition

Sequential Acquisition

For Phase I scheme, it is convenient to lock both arm cavities first because each signals are almost separate with recycling cavity unlocked. Lock was acquired quite quickly, within a second, which was same for plain FP cavity without coupling cavity. According to the

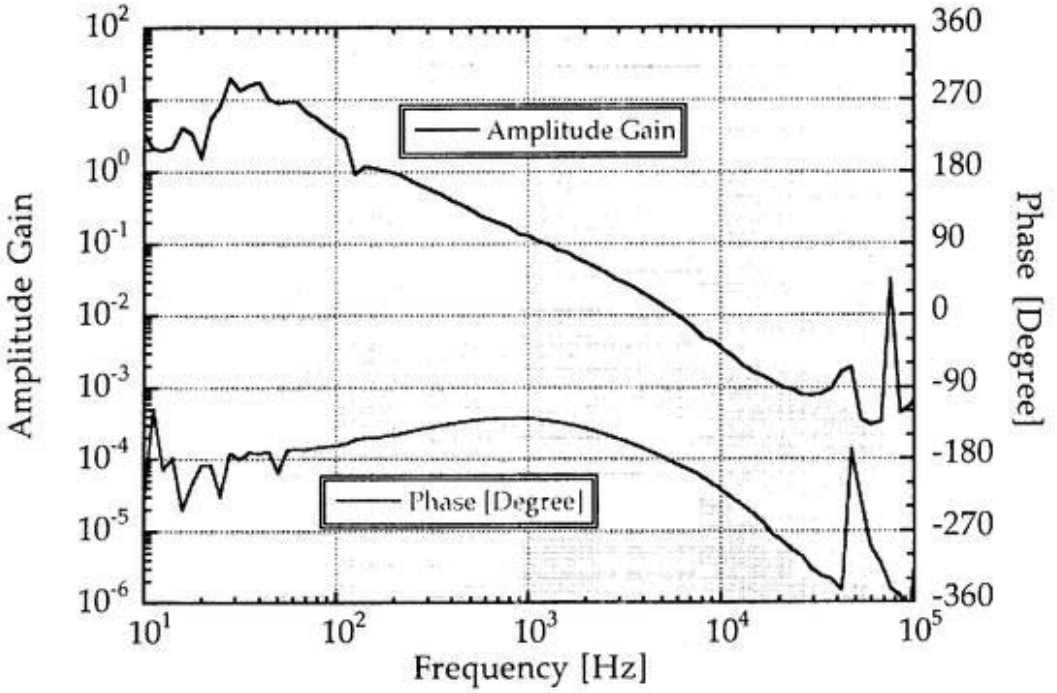

Figure 3.25: Open loop transfer function for arm cavity control loops.

resonance shape of recycling cavity, input power to the arm cavities, and resulting open loop gain changed by figures, but lock was not destroyed thanks to wide gain margin phase compensation.

Then recycling cavity was locked without Michelson control. Also for this loop, gain fluctuation of recycling cavity due to loss of Michelson fringe was serious. But feed back system could keep up with this change robustly. Finally, Michelson part was locked and whole interferometer was guided to lock.

Automatic Acquisition

When this prototype was operated as a FPMI, which was not yet recycled, automatic lock acquisition scheme was developed on this prototype for the first time. The FPMI was to be controlled with three degrees of freedom, L_C, L_D, l_D, and some special locking sequence was developed historically. For example, guided lock system on 3 meter interferometer at University of Tokyo or sign flip system on MK II at Caltech. But this prototype showed the capability of automatic lock acquisition, with which all three degrees of freedom were

locked by some order after closing three feed back loops.

Similarly, automatic acquisition is applicable to PRFPMI for both Phase I and II locking schemes. After closing four loops, which correspond to L_C, L_D, l_C, l_D , respectively, whole interferometer was lead to full lock within a minute typically. For Phase I, it was frequent to lock both arms first as can be expected.

3.3.4 Recycling Gain

Two kinds of recycling mirror were tested to demonstrate the power recycling of FPMI with super high quality optics as its mirrors. Main goals of this experiment are to realize high optical gain and to establish the lock acquisition sequence of such high gain recycled FPMI. The designed recycling gain for two recycling mirrors can be calculated by using the relation,

$$G_{REC} = \left(\frac{t_{REC}}{1 - r_{REC} r_{FPMI}} \right)^2 \tag{3.17}$$

which turns to be about G_{REC}=7.7 and 12.4 for recycling mirror of R=0.70 and 0.91, respectively, assuming $r^2_{FPMI} = 0.92$.

The resulting recycling gains are shown in Fig.3.26, 3.27. The transmitted powers of inline and perpendicular cavity were monitored and normalized with the transmitted power without recycling mirror. As only carrier light can resonate in the arm cavity, this enhancement factor of transmitted light corresponds to the carrier recycling gain G_0. Though the recycling gain of both configurations are somewhat fluctuating at low frequencies, the designed recycling gains were roughly achieved with a good repeatability.

It is worth noting that for both recycling experiment, the transmitted power from two arm cavities has excellent correlation and almost agree with each other within a calibration accuracy. This implies that fluctuation of the recycling gain does not comes from the degradation of transmission efficiency of local arm cavity, but from power fluctuation inside the recycling cavity. This is more clearly shown in the visibility of power recycled FPMI (PRFPMI) from symmetric port and contrast of Michelson interferometer from antisymmetric port. The recycling gain and the bright fringe (inverse of the contrast) has an anti-correlation, which means that good contrast gives high gain because good contrast increase the reflectivity of FPMI. On the other hand, recycling gain and visibility has a positive correlation, which can be explained as follows. When contrast is improved and the

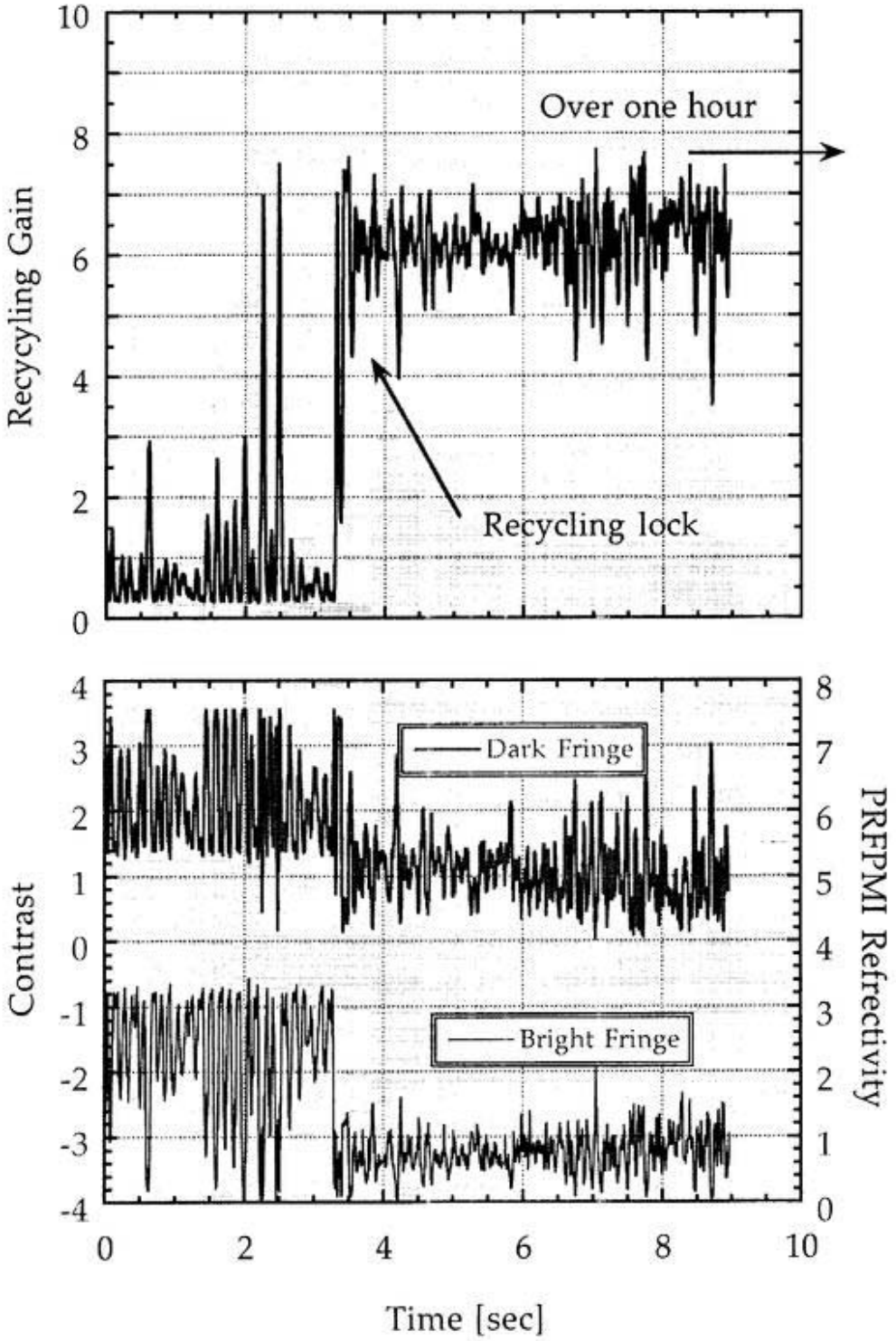

Figure 3.26: Attained recycling gain with $R = 0.70$ mirror.

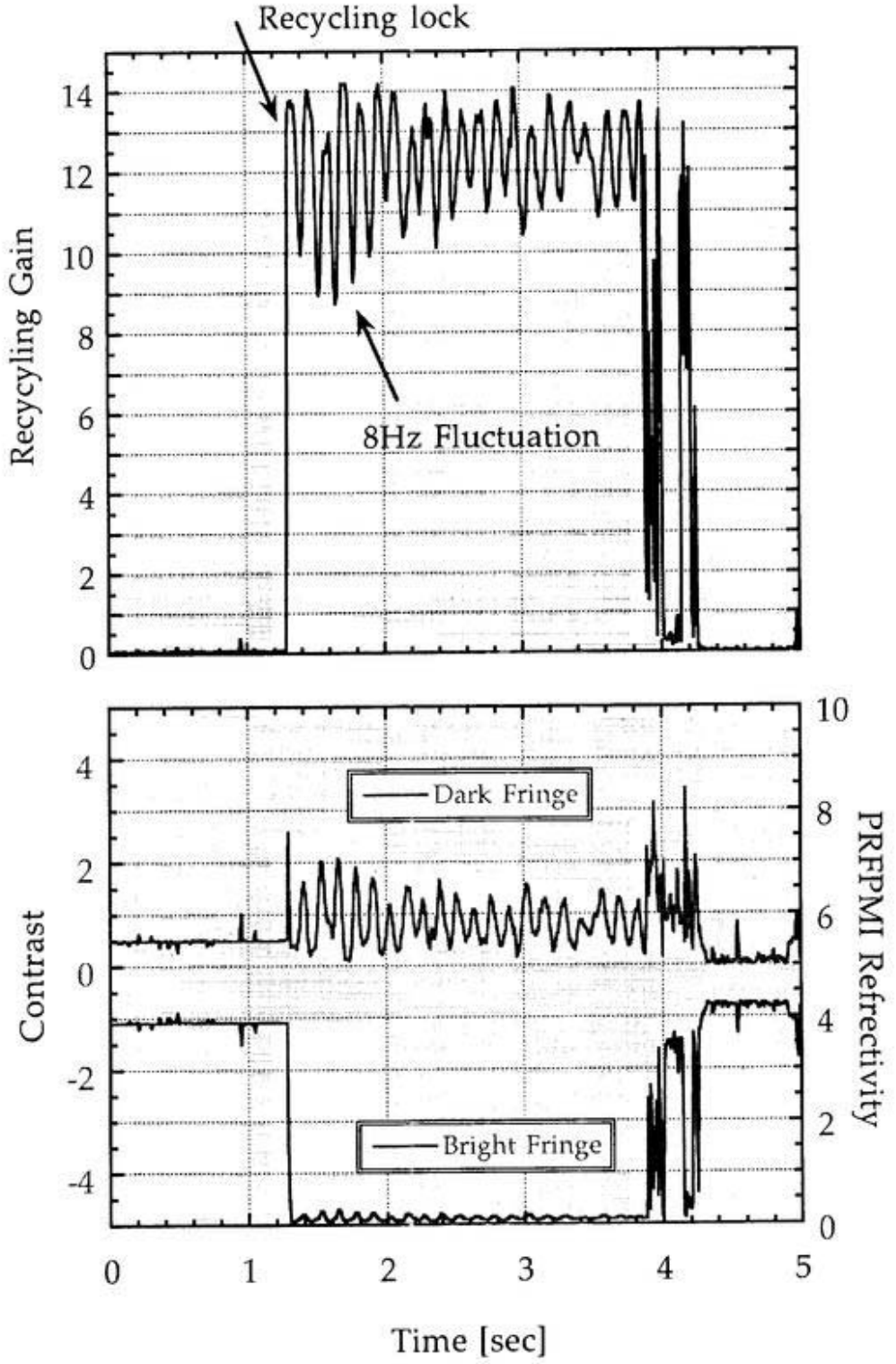

Figure 3.27: Attained recycling gain with $R = 0.91$ mirror.

reflectivity of FPMI is increased, the imbalance between two mirrors, recycling mirror and complex mirror (FPMI), will grow larger. So, this imbalance make visibility poor.

Another concern is the nature of the fluctuation of the recycling gain. As can be seen from the figures, main component of the oscillation appears at around 8Hz . This frequency component was also observed at the antisymmetric fringe of FPMI operation mainly due to the pitch motion of the arm mirrors, which was excited by the blade spring resonance. So, the possible mechanisms to make serious contrast defects are the degradation of the arm cavity reflectivity and contrast defects due to the imperfect interfere at the beam splitter caused by the optical axis tilt of the reflection beam. This can not be compensated by the length control system and should be stabilized by the alignment control system.

3.4 Wave Front Sensing

3.4.1 FP cavity Control

Configurations

In order to test the wave front sensor, demodulating system, feed back system and all other alignment control system to work properly, plain Fabry Perot cavity was tried to be alignment controlled using inline arm cavity of 20m prototype. The length and alignment control design for the cavity is shown in Fig.3.28. The reflected beam from the beam splitter towards the perpendicular arm was shuttered in front of the input mirror and recycling mirror was intentionally misaligned to prevent undesirable recycling cavity resonance. The reflected light from the BSAR was used for length control by using small aperture 40MHz resonant photodetector. The antisymmetric light which is about 70 times bigger in power compared with that from BSAR was separated by half beam splitter and used for two wave front sensors (WFSs).

Guoy Phase Telescopes

The Guoy phase telescopes (GPT) were additionally assembled to separate the input mirror and the end mirror degrees of freedom as described in previous section. The importance to design it is how GPT can be compact. The total optical path length to the WFS should be as short as possible to prevent to pickup the artificial wave front distortions due to air fluctuation, and total numbers of optics should be minimized to suppress the

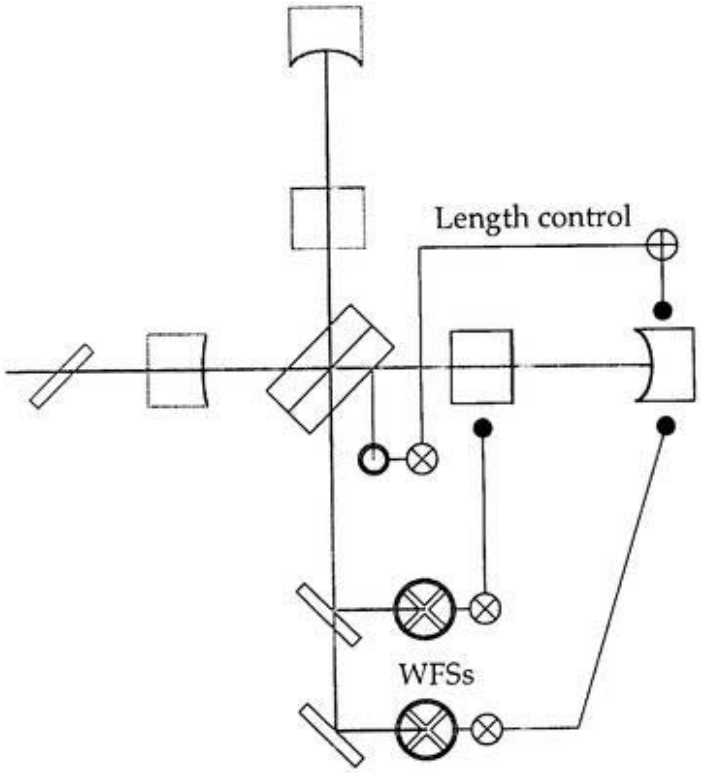

Figure 3.28: Optical configuration for alignment control of FP cavity.

wavefront distortions due to imperfect optics. The designed beam propagation and guoy phase evolutions with GPT are shown Fig.3.29 3.30 for η =1 and 3. The total optical path

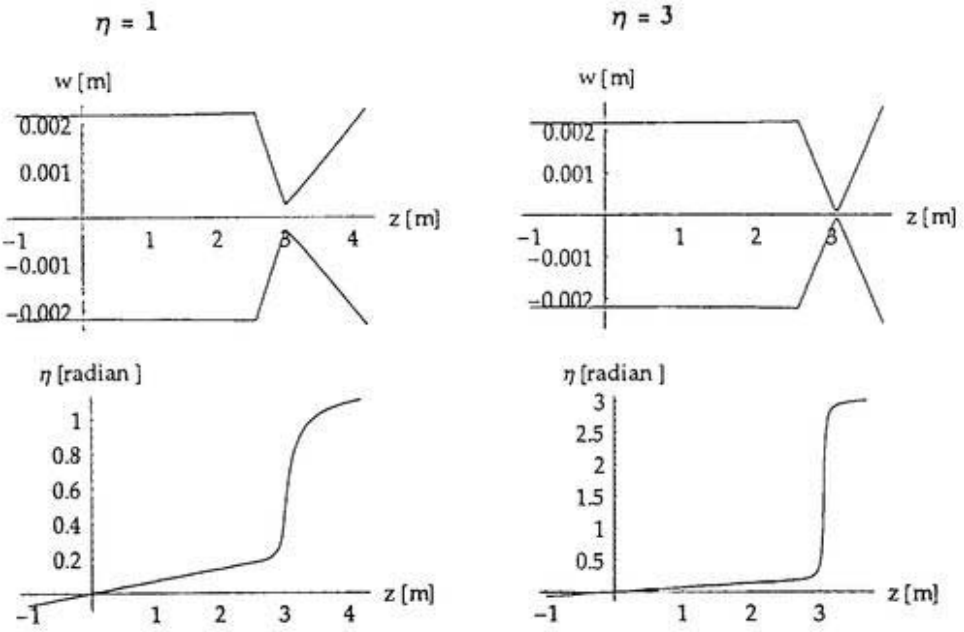

Figure 3.29: Beam propagation from the waist of the cavity mode to WFSs through GPT.

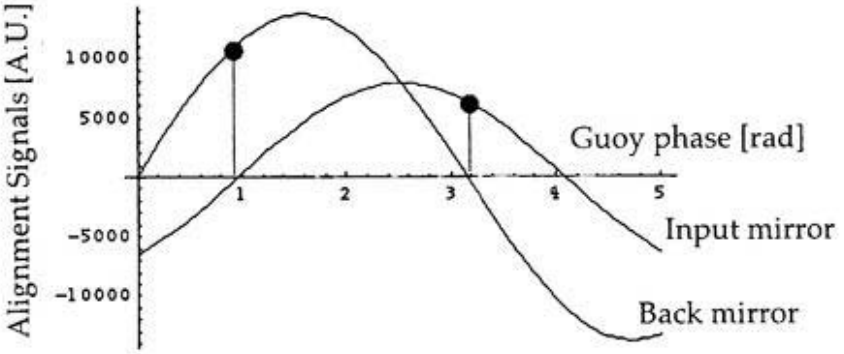

Figure 3.30: Alignment signals for IM and BM with Guoy phase evolution.

from input mirror to the WFS are less than 3m and it takes only 1.6m from the optical

window to the WSFs.

Servo Design

Obtained error signals for pitch and yaw degrees of freedom were fed back to the arm cavity mirrors through servo filter and signal matrix box. These servo filters employ one pole-zero pair with DC gain booster and typical unity gain frequencies were around 20Hz which was needed to sufficiently suppress the 8Hz pitch mode oscillations. The open loop transfer function for end mirror pitch control loop is shown in Fig.3.31. These control

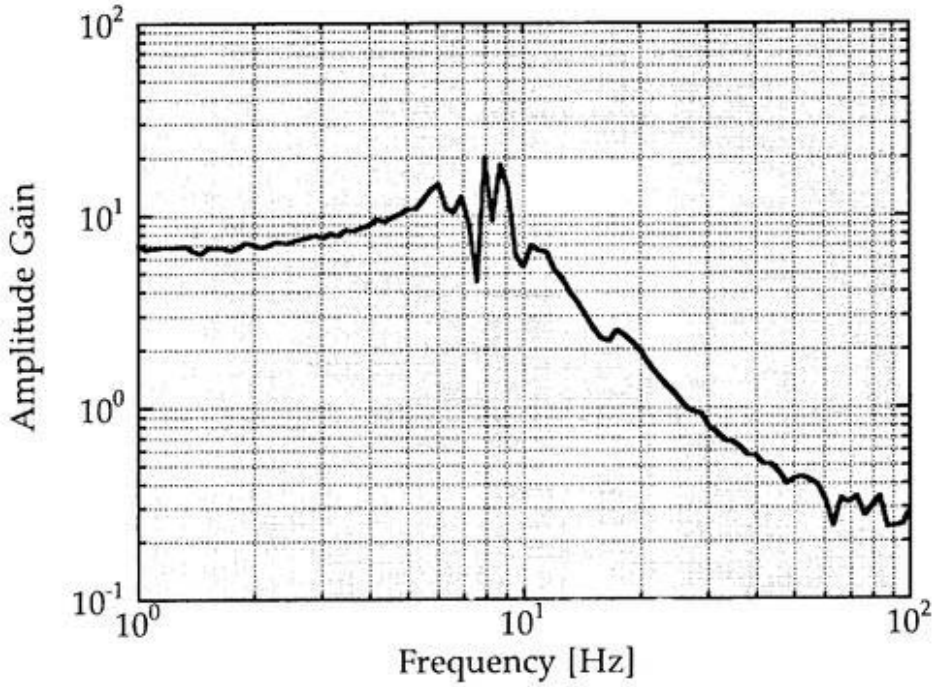

Figure 3.31: Open loop transfer function of alignment control loop.

signals for pitch and yaw degrees of freedom are inserted into signal matrix together with the length signal and summed to four control signals which corresponds to four coil magnet actuators after adding and subtracting processes.

Alignment Controlled Cavity

The effect of alignment control using wave front sensing on cavity stability is shown in Fig.3.32. Initial state is an alignment control free locking, which has a typical 8Hz

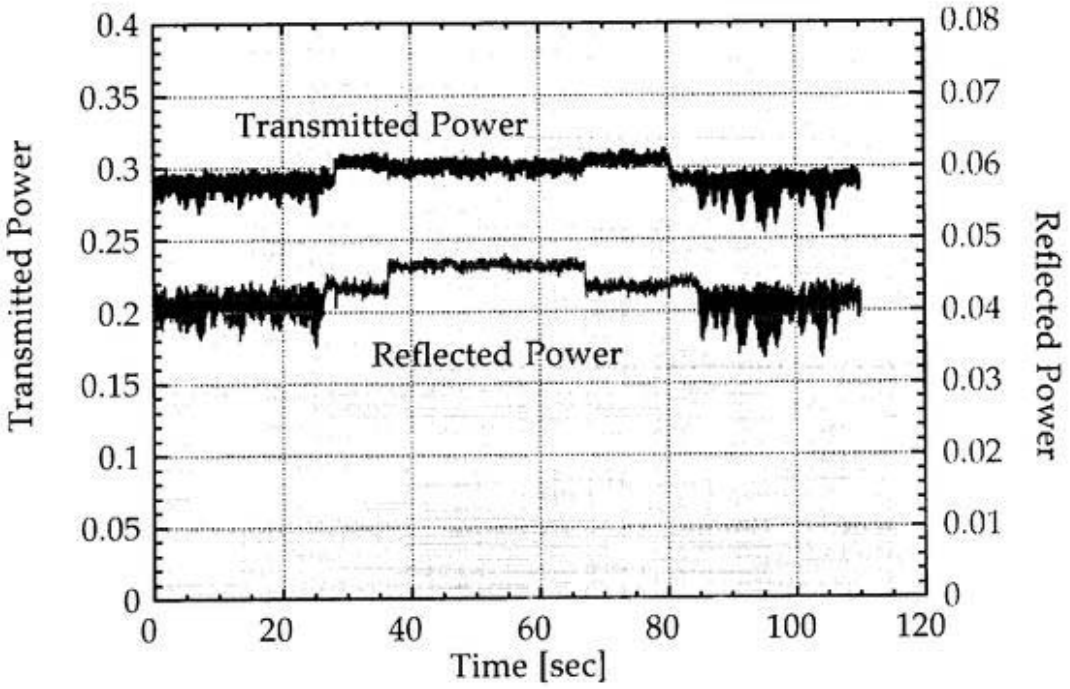

Figure 3.32: Stabilization of FP cavity by alignment control.

fluctuation both in reflected and transmitted power of light. The last stage shows stabilized cavity with engagement of all four degrees of freedom of alignment. The 8Hz fluctuation was satisfactory suppressed and also both transmitted and reflected light level were increased.

3.4.2 Interferometer Control

Configurations

The goal of this experiment is to stabilize the high recycling gain and maintain the lock for a long time over 1 hour at least. There are total 12 degrees of freedom to be controlled including beam splitter. Though all these degree should be controlled at final stage of PRFPMI operation, there can be effective way to stabilize the system with less amount of control. As reported by MIT group on phase noise interferometer [8], the recycling gain of simple Michelson interferometer was sufficiently stabilized by control the only differential degree of freedom of arm mirror misalignment. This effects were already calculated and reported and this experiment confirmed it. From this point of view, the differential mode control of arm cavity was tried for the first step. The experimental configuration is shown

in Fig.3.33. The length control topologies was same for alignment control free recycling

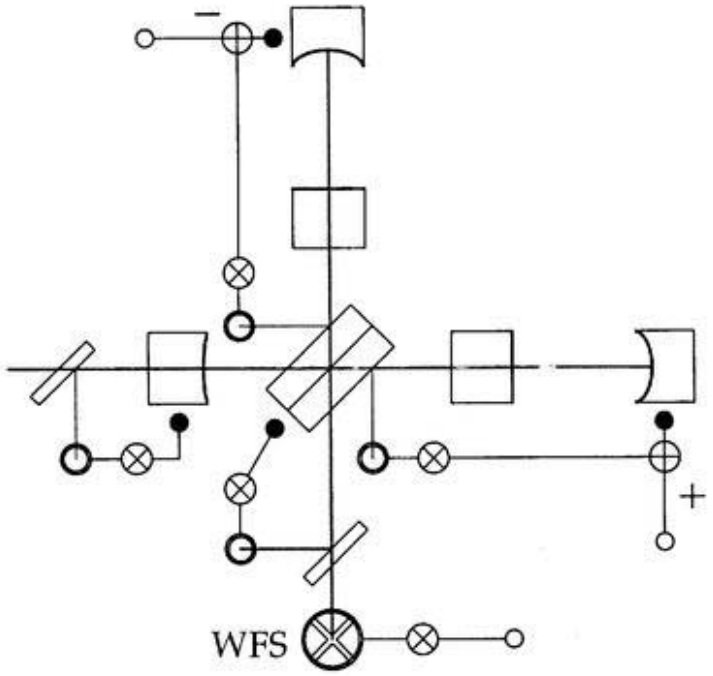

Figure 3.33: Optical configuration of PRFPMI with WFSs.

experiment, phase I. Additional WFS was fabricated on the detection bench to pick up the alignment signals by using a part of antisymmetric light divided by half beam splitter. In the antisymmetric light, almost all the alignment signals are mixing as calculated in previous section. Especially, the alignment signals for input and end mirrors can not be separated at all. However, if the end mirror motion of tilt is predominant for optical axis tilt of the arm cavity and accordingly for the contrast defects, the PRFPMI system can be stabilized using antisymmetric light by feeding back to the both end mirrors differentially.

Alignment Controlled PRFPMI

The stabilized recycling gain is shown in Fig 3.34. The alignment control free locking

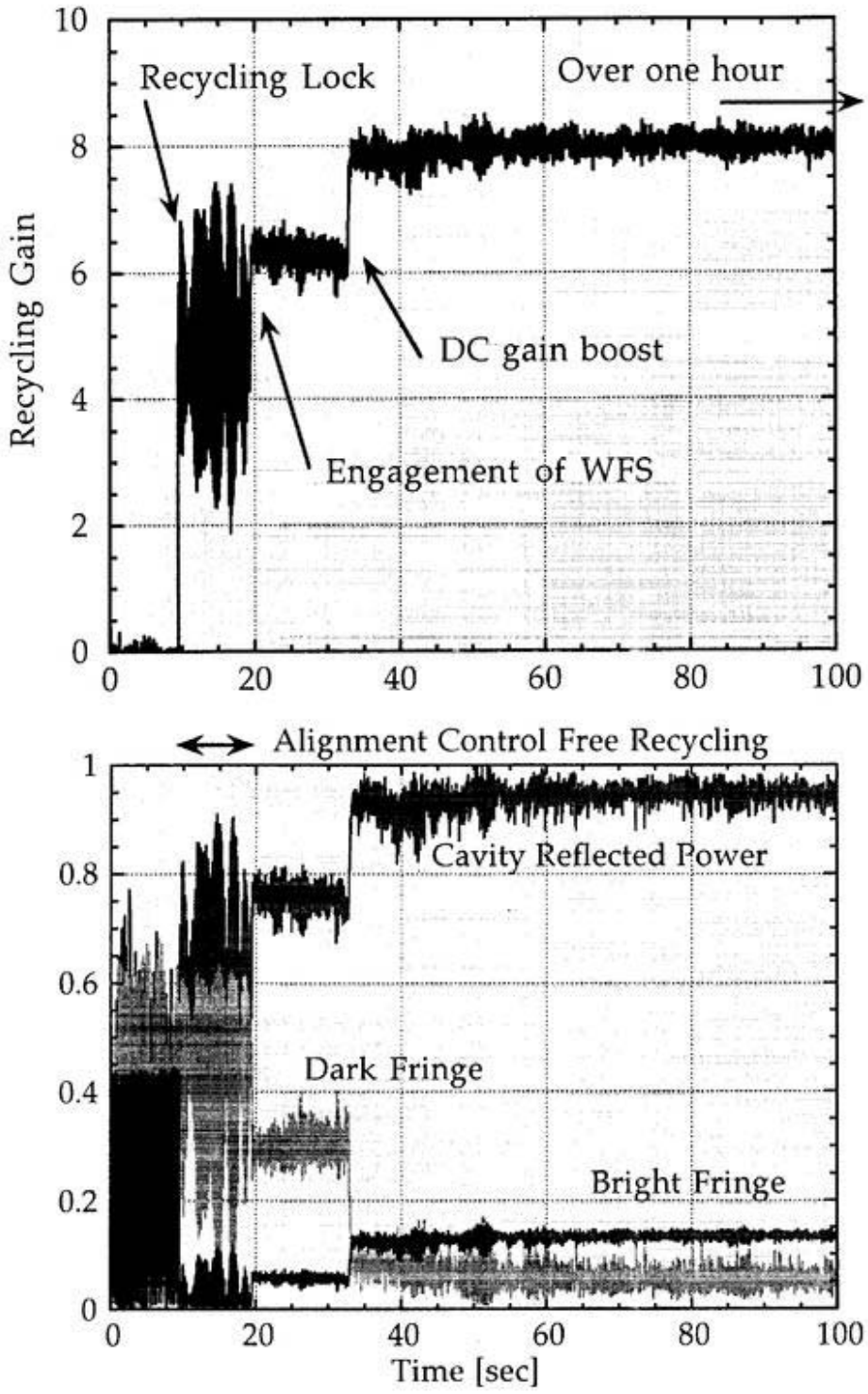

Figure 3.34: Stabilized recycling gain by engagement of alignment control.

interval contains huge 8Hz fluctuation in the gain, but it was stabilized by engagement of alignment control. Further more, DC gain booster increased the recycling gain by 25% , from 6 to 8. This implies that DC offset of alignment existed at initial alignment tuning before locking the complete interferometer. In other words, as far as WFSs shows "correct" alignment signals, initial alignment by hand do not have adequate accuracy for recycling.

Chapter 4

Conclusion

To summarize, the power recycling technique was tested on the 20m baseline prototype interferometer with suspended mirrors. In order to realize high recycling gain, interferometer loss induced by mirror loss and misalignment of optics was successfully controlled. The total loss of the high reflecting mirror was measured to be below 30ppm/optics for about 10mm size beam. These super high-quality mirrors were obtained after repetition of test coating and loss measurement of them. In these measurements, two equivalent mirrors were used to form a 20m Fabry-Perot cavity. This made it possible to measure total loss factor directly and accurately with actual size of beam and serves a new method to measure the loss of mirrors for large interferometer.

Automatic alignment control system using wave-front sensors were implemented to stabilize the optical fluctuations in the interferometer. The pith motion of test masses which were excited by resonance of suspension system resulted in a contrast fluctuation of about one percent. By engagement of alignment control, contrast at the beam splitter due to misalignment of the mirrors were considerably stabilized and improved. This was the first demonstration of wave-front sensing technique on full configured interferometer with suspended masses and this showed the effectiveness of the alignment control.

As a result, 20m prototype interferometer locked with sufficiently high power recycling gain of over 12. This is the highest gain ever reported in the world by Fabry-Perot Michelson interferometer with suspended mirrors. The whole interferometer was acquired lock by both sequential and automatic locking method within a minute typically. From these result, it is shown that the power recycled interferometer with high gain can acquire lock automatically even if control signals are not well separated. Furthermore the remaining gain fluctuation

due to mirror misalignment was sufficiently suppressed by engagement of wave-front sensing technique and the stable operation was realized .

Success of this work on high gain recycling and implementation of automatic alignment control system using wave-front sensing on 20m interferometer marks significant progress towards achieving full-configured interferometer. This work concludes that loss factor of the interferometer can be reduced by controlling both quality of optics and alignment of optics so as to demonstrate high recycling gain and recycling is feasible technology for large scale interferometer with respect to the high recycling gain.

References

[1] B. J. Meers, Phys. Rev. D **38**, 2317(1988).

[2] A. Abramovici, W.E. Althouse, R.W.P. Drever, Y. Gursel, S. Kawamura, F.J. Raab, D. Shoemaker, L. Sievers, R.E. Spero, K.S. Thone, R.E. Vogt, R. Weiss, S.E. Whitcomb, and M.E. Zucker, Science **256**, 325 (1992).

[3] C. Bradaschia, R. Del Fabbro, A. Di Virgilio, A. Giazotto, H. Kautzkey, V. Montelatici, D. Passuello, A. Brillet, O. Cregut, P. Hello, C. N. Man, P. T. Manh, A. Marraud, D. Shoemaker, J. -Y. Vinet, F. Barone, L. Di Fiore, L. Milano, G. Russo, S. Solimeno, J. M. Aguirregabiria, H. Bel, J.-P. Du- ruisseau, G. Le Denmat, P. Tourrenc, M. Capozzi, M. Longo, M. Lops, I. Pinto, G. Rotoli, T. Damour, S. Bonazzola, J. A. Marck, Y. Gourghoulon, L. E. Holloway, F. Fuligni, V. Iafolla, and G. Natale, Nucl. Instr. Meth. Phys. Res. **A289** (1990) p.518.

[4] K. Danzmann, H. Luck, A. Rudiger, R. Schilling, M. Schrempe, W. Wink- ler, J. Houah, G. P. Newton, N. A. Robertson, A. M. Campbell, J. E. Logan , D. I. Robertson, K. A. Strain, J. R. J. Bennett, V. Kose, M. Kiuhne, B. F. Schutz, D. Nicholson, J. Shuttleworth, H. Welling, P. Aufmuth, R. Rinkleff, A. Tiunner- mann, and B. Willke, Internal report MPQ 190 (1994)

[5] K. Tsubono et.al. in First Edoardo Amaldi Conference on Gravitaional Wave Experiments, Frascati , 1994 (World Scientific, Singapole, 1995) , pp.112-114

[6] T. Nakamura, N. Mio, and M. Ohashi

[7] D. Shoemaker, R. Schilling, L. Schnupp, W. Winkler, K. Maischberger, and A. Rudiger, Phys. Rev. D38 (1988) p.423.

[8] P. Fritschel, G. Gonzalez, B. Lantz, P.Saha, and M. Zucker, Phys. Rev. Lett. **80**, 3181 (1998)

[9] R. W. P. Drever, "Interferometric detectors for gravitational radiation" in *Gravitation Radiation*, North-Holland, pp.321-338 (1983)

[10] P.Fritschel , Ph.D Thesis, Massachusetts Institute of Technology, (1992), unpublished.

[11] Akitoshi Ueda, Noburu Uehara, Katsumi Uchisawa, Ken-ichi Ueda, Hisao Sekiguchi, Takayoshi Mitake, Kenji Nakamura, Naoya Kitajima and, Izumi Kataoka, "Ultra-high quality cavity with 1.5ppm loss at 1064 nm" Opt. Rev. **5**, 369-372 (1996).

[12] R. W. P. Drever, J. L. Hall, F. V. Kowalski, J. Hough, G. M. Ford, A. J. Munleyand, and H. Ward, "Laser phase and frequency stabilization using an optical resonator" Appl. Phys. **B31**, 97 (1983).

[13] M.W. Regehr, Ph.D Thesis, California Institute of Technology, Pasadena (1995), unpublished.

[14] M. Ando, K. Kawabe, and K. Tsubono, Phys. Lett. A, **237**, 13-20, (1997)

[15] D.Z. Anderson, Appl. Opt. 23. 2944 (1984).

[16] E.Morrison,B. J.Meers,D.I.Robertson,and H.Ward, Appl.Opt. 33, 5037(1994). E. Morrison, B.J. Meers, D.I. Robertson. and H. Ward, Appl. Opt. 33, 5041 (1994).

[17] Nergis M., Ph.D Thesis, California Institute of Technology, Pasadena (1997), unpublished.

[18] M. Ohashi, Doctral Thesis, University of Tokyo, (1997), unpublished.

[19] S. Telada, Doctral Thesis, Graduate University for Advanced Studies, (1997), unpublished.

[20] A. Araya, Doctral Thesis, University of Tokyo, (1994), unpublished.

[21] S. Miyoki, Doctral Thesis, University of Tokyo, (1995), unpublished.

[22] Akito Araya, Norikatsu Mio, Kimio Tsubono, Koya Suehiro, Souichi Telada, Masatake Ohashi, and Masa-Katsu Fujimoto, "Optical mode cleaner with suspended mirrors" Appl. Opt. **36**, 1446-1453 (1997).

[23] Masatake Ohashi, Koya Suehiro, Souichi Telada, Shuichi Sato, Masa-Katsu Fujimoto, Ryutaro Takahashi, Shinji Miyoki, Toshitaka Yamazaki, Mitsuhiro Fukushima, Akito Araya, and Osamu Miyakawa, "Current status of 20m prototype" in *Gravitational wave detection*, Universal Academy Press, pp.147-154.

[24] Souichi Telada, Koya Suehiro, Shuichi Sato, Masatake Ohashi, Masa-Katsu Fujimoto, and Akito Araya, "Development of a mode cleaner for laser interferometer gravitaional wave detector" in *Gravitational wave detection*, Universal Academy Press, pp.349-351.

[25] Noburu Uehara, and Ken-ichi Ueda, "Accurate measurement of ultra low loss in a high finesse Fabry-Perot interferometer using the frequency response function" Appl. Phys. B. **61**, 9-15 (1995).

[26] A. Rüdiger, R. Schilling, L. Schunupp, W. Winkler H. Billing, and K. Maischberger, "A mode selector to suppress fluctuations in laser beam geometry" Opt. Acta. **28**, 641-658 (1981).

[27] N. Z. Anderson, J. C. Frisch and C. S. Masser, "Mirror reflectometer based on optical cavity decay time" Appl. Opt. **23**, 1238-1245 (1984).

[28] Shinji Miyoki, Shuichi Sato, Masatake Ohashi and Masa-Katsu Fujimoto, "Techniques to estimate the reflectance of a high-reflectance dielectric multilayer coating mirror using incident beam angular dependencies of its transmittance" Opt. Rev. **5**, 17-19 (1998).